Rapid Identification of Virtual CNC Drives

by

Wilson Wai-Shing Wong

A thesis
presented to the University of Waterloo
in fulfillment of the
thesis requirement for the degree of
Master of Applied Science
in
Mechanical Engineering

Waterloo, Ontario, Canada, 2007

AUTHOR'S DECLARATION FOR ELECTRONIC SUBMISSION OF A THESIS

I hereby declare that I am the sole author of this thesis. This is a true copy of the thesis, including any required final revisions, as accepted by my examiners.

I understand that my thesis may be made electronically available to the public.

Wilson Wai-Shing Wong

Abstract

Virtual manufacturing has gained considerable importance in the last decade. To obtain reliable predictions in a virtual environment, the factors that influence the outcome of a manufacturing operation need to be carefully modeled and integrated in a simulation platform. The dynamic behavior of the Computer Numerical Control (CNC) system, which has a profound influence on the final part geometry and tolerance integrity, is among these factors. Classical CNC drive identification techniques are usually time consuming and need to be performed by an engineer qualified in dynamics and control theory. These techniques require the servo loop or the trajectory interpolator to be disconnected in order to inject the necessary identification signals, causing downtime to the machine. Hence, these techniques are usually not practical for constructing virtual models of existing CNC machine tools in a manufacturing environment.

This thesis presents an alternative strategy for constructing virtual drive models with minimal intervention and downtime to the machinery. The proposed technique, named “rapid identification”, consists of executing a short G-code experiment and collecting input/output data using the motion capture feature available on most CNC controllers. The data is then processed to reverse engineer the equivalent tracking and disturbance transfer functions and friction characteristics of the machine. It is shown that virtual drive models constructed this way can be used to predict the real machine’s contouring performance for large class of drive systems, controlled with different control techniques.

In the proposed scheme, the excitation is delivered by smoothly interpolated motion commands. Hence, convergence of parameters to their true values is not guaranteed. When the real system contains pole-zero cancellations, namely due to feedforward control action, this also results in a loss of identifiability. In order to guarantee the stability of the identified drive models, the pole locations are constrained with frequency and damping ratio limits. Hence, the rapid identification task is cast as a constrained minimization problem.

Two solution strategies have been developed. In the first approach, Lagrange Multipliers (LM) technique is applied, which yields successful estimation results. However,

implementation of LM is computationally intensive and requires the use of a dedicated symbolic solver. This limits the portability for industrial implementation. In the second approach, a Genetic Algorithm (GA) search technique is developed, which is a more practical but slightly approximate alternative. The GA allows parameter bounds to be incorporated in a natural manner and converges to 2-3% vicinity of the LM solution in one-tenth of the computation time. The GA solution can be easily ported to different computation platforms.

Both LM and GA identification techniques were validated in simulations and experiments conducted on virtual and real machine tool drives. It is shown that although the parameters estimated using the rapid identification scheme do not always match their true values, the key tracking and disturbance rejection characteristics of the drives are successfully captured in the frequency range of the CNC motion commands. Therefore, the drive models constructed with rapid identification can be used to predict the contouring accuracy of real machine tools in a virtual process planning environment.

Acknowledgements

I would like to express my sincerest gratitude towards my advisor Dr. Kaan Erkorkmaz for his invaluable support and encouragement throughout my graduate study. I consider it a great privilege to work with him. Without his guidance, patience and wisdom this work would not have been possible. I am indeed indebted to him for all that he has done for me.

I would also like to think my reading committee members, Drs. Michael Mayer and William Melek who took the time to read my thesis and gave me advantageous feedback.

Furthermore, I would like to thank my colleagues in the Precision Control Laboratory, my friends, as well the faculty and staff, especially Robert Wagner, Andy Barber, and Steve Hitchman, at the University of Waterloo – Department of Mechanical and Mechatronics Engineering, who have made my experience at UW very enjoyable.

Finally, I would like to thank my beloved family for their unwavering support and patience regarding my graduate study I dedicate this work to them.

Table of Contents

List of Figures

List of Tables

Chapter 1

Introduction

1.1 Introduction

Virtual manufacturing has gained considerable importance in the last decade, with the increasing availability of computational power which enables accurate simulation of complex phenomena that govern manufacturing operations [1], [2]. The ability to predict, evaluate, and optimize the performance of production machines and processes, without having to build costly prototypes or run production trials, is highly appealing to both machine tool builders and end users. The ultimate objective of virtual manufacturing is to achieve the shortest possible cycle time and lowest cost, while maintaining the desired product quality from the very first part onwards. The time, money, and engineering effort that could be saved through sidestepping the prototyping and testing stages also promises shorter turnaround times for putting new products on the market, in response to changing demands.

To obtain reliable predictions in a virtual environment, the factors that influence the outcome of a manufacturing operation need to be carefully modeled and integrated into a simulation platform. These factors typically originate from the process, the machine dynamics, and the interaction between the two. Among factors pertaining to the machine tool, the dynamic behavior of the Computer Numerical Control (CNC) system has a profound influence on the final part geometry, as well as the tolerance integrity and surface quality. When axis servo errors become excessive, the part geometry gets distorted and tolerances may be violated. If the tool motion is not smooth, this would cause noticeable feed marks on the machined part. In either case, the part may become unacceptable.

In order to predict the impact of the CNC system on the final part quality, a Virtual CNC (VCNC) simulator was developed in [3]. The VCNC enables the contouring performance of

a real machine tool to be predicted and optimized in a virtual process planning environment. However, its prediction accuracy relies strongly on the validity of feed drive models that are identified from the actual machine. Standard identification tests are usually time consuming and need to be performed by an engineer who is qualified in dynamics and control theory. Sometimes, these experiments require the servo loop or the trajectory interpolator to be disconnected, so special identification signals like sine or square waves, random noise, or sine wave speeds can be injected into the servo system. When these factors are considered, building even basic virtual models of CNC systems may require significant downtime to the production machines, which is usually not practical in a manufacturing environment.

In this thesis, an alternative identification strategy is developed for constructing virtual models of machine tool drives. The proposed technique, named “rapid identification”, consists of executing a short G-code experiment and collecting input and output data using the motion capture feature available on most CNC systems. The rapid identification test can be conducted quickly, as if running a diagnostic routine, without any hardware or software modification to the machine. The collected data is then processed with the intention of reverse engineering the equivalent tracking and disturbance transfer functions of the closed loop drive system, as well as the guideway friction. It is shown that a virtual drive model constructed this way enables accurate prediction of the real machine’s contouring accuracy for a variety of feed drive systems controlled with different control techniques.

The excitation input, in rapid identification, is delivered through motion commands interpolated by trajectory generator. These signals are typically smooth up to the acceleration level (i.e. C^2 continuity) and lack the persistence of excitation to allow accurate estimation of a large number of parameters. On the other hand, if the real servo system contains pole-zero cancellations, which usually occur when feedforward action is employed in the controller, this also results in incorrect estimation of the closed loop dynamics. Deviations between the true and identified drive models are acceptable as long as the virtual model captures the dynamics of the real drive system with sufficient closeness in the frequency range of the CNC motion commands as observed in Section 3.4. In extreme cases, the non-

convergence of parameters can also result in the identification of critically stable or even unstable virtual models, which have limited practical value. In order to avoid this problem, bounds are imposed on the closed loop pole locations, which results in the identification problem to assume the form of a constrained optimization problem.

Two solution strategies have been developed in this thesis. In the first approach, Lagrange Multipliers (LM) technique is applied, which yields successful estimation results. However, implementation of LM is found to be computationally intensive, and also requires the use of a dedicated symbolic solver, like Matlab's Symbolic Toolbox, to construct and solve a system of nonlinear equations for each constraint activation case (i.e. Kuhn-Tucker switching conditions [4]). These factors significantly limit the portability of the LM technique for industrial implementation. As a more practical but slightly approximate approach, a Genetic Algorithm search technique has also been developed. The GA's ability to constrain the search space allows the parameter bounds to be incorporated in a natural manner. Computational speed of the GA has been streamlined by decoupling all a priori calculations from the terms that need to be recomputed for each iterative cycle. It is shown that the GA solution converges to 2-3% vicinity of the LM solution in one-tenth of the computational time with a repeatable rate of 100%. The developed rapid identification scheme has been verified in simulations and experiments conducted on virtual and real machine tool drives. It is shown that the identified drive models can be successfully used for predicting the contouring accuracy of real machine tools in a virtual process planning environment.

Chapter 2

Literature Review

2.1 Introduction

This chapter presents a review of literature and industrial state-of-the-art in the areas of virtual manufacturing, feed drive identification, and evolutionary programming. Section 2.2 introduces the concept of virtual manufacturing and the Virtual CNC framework. Various techniques dedicated to the modeling and identification of feed drives are surveyed in Section 0. Evolutionary programming, which is the basis of the Genetic Algorithm solution, is introduced in Section 2.4. Conclusions for the chapter are presented in Section 2.5.

2.2 Virtual CNC

Many companies involved in manufacturing have started developing new technologies and products that exploit modern computers' ability to simulate manufacturing operations in a virtual environment. CAD/CAM packages such as MasterCam® and ESPRIT® provide toolpath visualization and analysis modules to help avoid potential collisions, which might

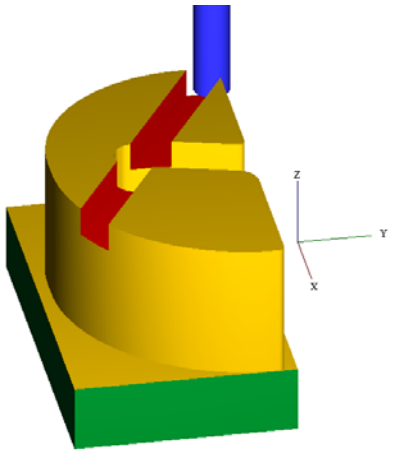

Figure 2.1. Simulation of a machining path in CAD/CAM software.

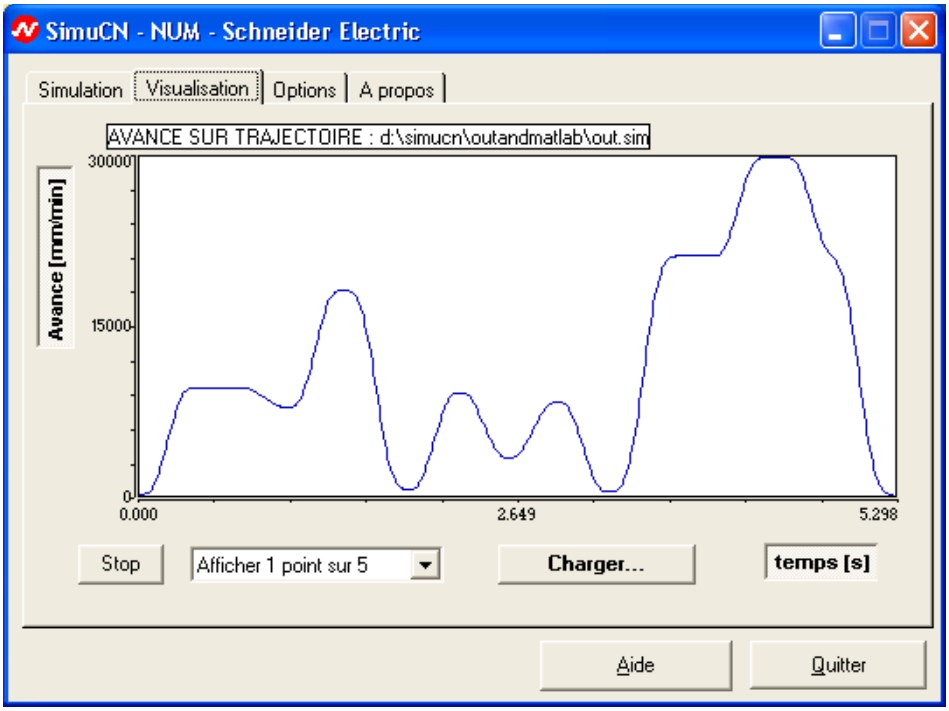

Figure 2.2. SimuCN® interface.

occur during the machining process. A snapshot of such an interface is shown in Figure 2.1. One disadvantage of these analysis tools is that they typically lack the dynamic information about the machine or the manufacturing process, and provide only a geometric visualization of what happens in the "ideal case". Recently drive manufacturers like Omron™, Jtekt™, and Schneider Electric™ have provided simulation software which allows the user to simulate the dynamic behavior of a drive system, by providing NC code as the input. Such software usually yields accurate predictions, since the drive parameters are known by the manufacturer. An example application, SimuCN® developed by NUM™ CNC, is shown in Figure 2.2. Other companies such as Siemens [5], Mori Seiki [6], and Ford Automotive [7] have also been contributing the development of virtual manufacturing technologies, by researching simulation systems that can predict and emulate the behavior of machining centers and Computer Numerical Control (CNC) systems.

The overall objective of virtual manufacturing is to be able to combine the effect of machine tool dynamics, manufacturing process, and the interaction between the two in a common simulation platform. The Virtual CNC (VCNC) shown in Figure 2.3 was developed

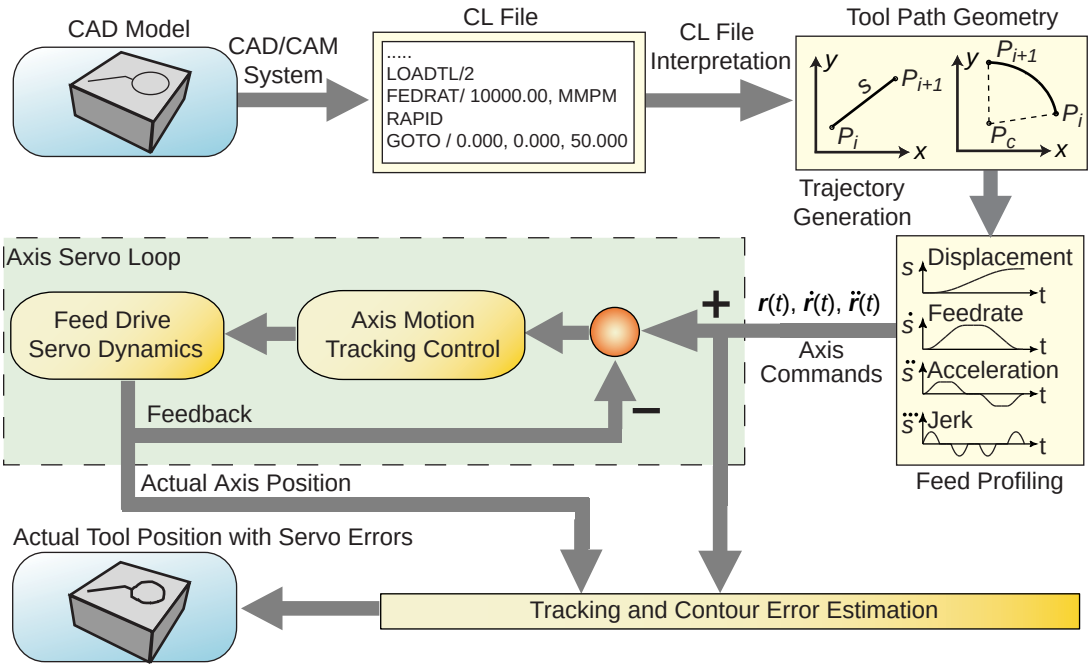

Figure 2.3. Overview of the Virtual CNC system.

at the University of British Columbia for this purpose; as a module to facilitate the simulation of a real CNC system in a virtual environment. The Virtual CNC allows the performance of machine tools to be optimized during design, development and end user stages [8], [9]. The user can prototype a real CNC by selecting standard modules out of libraries of feed drive models, control laws, trajectory generation algorithms, and feedback devices.

After the virtual CNC is configured, the contouring performance can be predicted and optimized for different part programs. The VCNC can be used as a design and testing platform by machine tool builders and controller developers [8], or as a process planning tool by end users [10]. The prediction accuracy of the VCNC was verified in experiments performed on real machinery, which matched the simulation results within less than 10% error. Such prediction accuracy was only achievable after scrupulous modeling and identification of the real machine's feed drive dynamics, indicating the importance of having a reliable model to obtain accurate predictions.

The structure of the VCNC is composed of three main functions: 1) The toolpath interpolation; 2) Simulation of the drives' response; 3) Performance evaluation. In the toolpath interpolation, the trajectory commands are generated using a Cutter Location (CL)

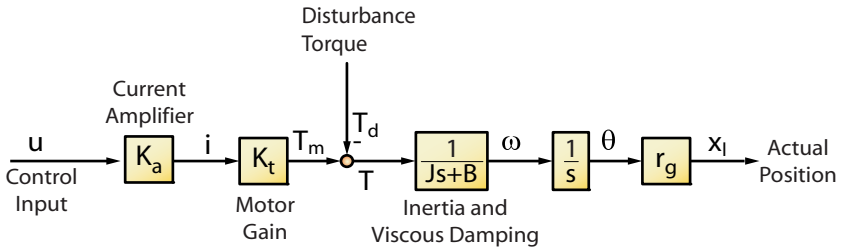

Figure 2.4. Simplified drive dynamic model.

file which is obtained from a CAD/CAM package like Unigraphics® or CATIA®. The user can select what type of feed profile (trapezoidal or S-curved velocity) will be used. Simulation of the drive's response considers the interaction between the open loop drive dynamics and the servo controller. The user can configure a detailed drive model using modules for ball screw (geared) or linear (direct driven) feed drives, available in a library. The controller library contains a wide range of control laws ranging from simple P, PID, P-PI cascade controllers to more complex techniques proposed in literature such as Pole-Placement [11], Generalized Predictive [12], Adaptive Sliding Mode [13] and feedforward [14], [15] control. Sensor noise, quantization, actuator saturation, backlash, and computational delays can also be defined for each virtual CNC model. During performance evaluation, important variables such as the contour error history, drive torque and current signals are presented to the user in context of the commanded toolpath, which allows critical regions to be easily identified. This enables corrective actions to be taken either by modifying the part program or improving the CNC design. The Virtual CNC is currently a module of CutPro machining process simulation software which is commercialized through Manufacturing Automation Laboratories Inc., a UBC spin-off company.

2.3 Modeling and Identification of Feed Drives

The Virtual CNC is a promising tool towards achieving the overall objective of simulating a complete digital factory in the virtual environment. However, the prediction accuracy of the VCNC is strongly dependent on the correctness of the drive models that are identified from real machinery. There has been extensive research in literature dedicated to building models of feed drive systems, as reviewed in the following.

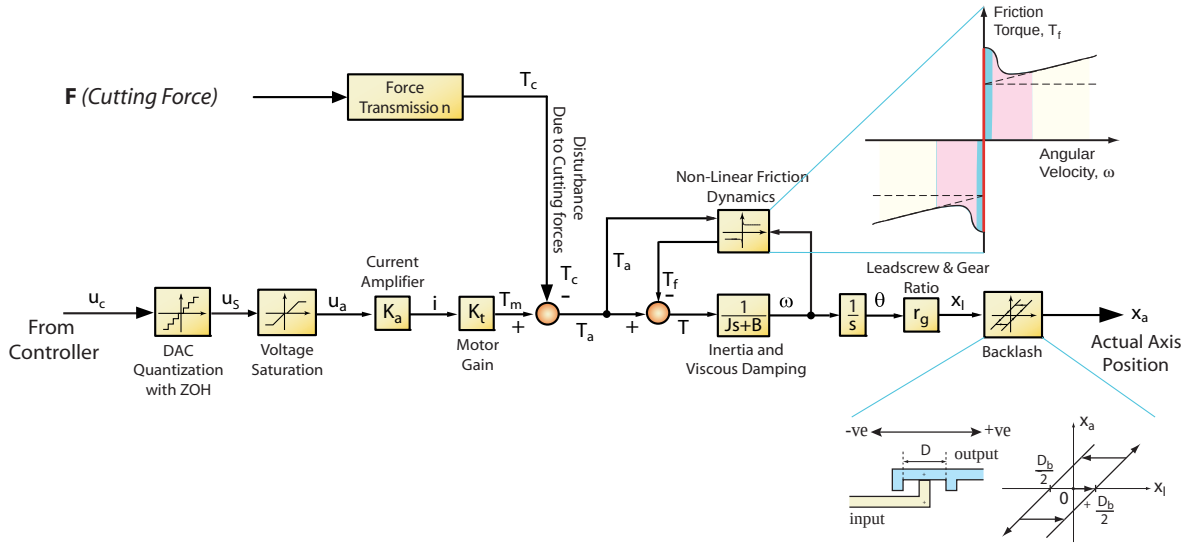

Figure 2.5. General feed drive model in Virtual CNC.

One of the basic models which is widely used was proposed by Koren [16]. This model considers only the linear rigid body dynamics, as shown in Figure 2.4. The current command u injected into the current amplifier (K_a) results in the armature current i, which is then converted into actuation torque T_m through the motor (K_t). Part of the actuation torque is consumed by disturbances (T_d) originating from nonlinear guideway friction and possibly the cutting process. The remaining torque actuates the drive system, which is represented by an equivalent inertia J and viscous friction B reflected on the actuator. The motor angular velocity ω is integrated to obtain angular position θ, which is then converted into linear axis movement x through the gear ratio r_g. Models have also been proposed that capture and integrate the nonlinear effect of friction in the feed drive. Armstrong et al. [17] has presented a very broad survey of the available techniques used to model and compensate friction in servo systems. They have proposed a seven parameter model which adequately captures the effect of pre-sliding displacement, static friction, and the full Streibeck curve describing how the friction force changes with the relative sliding velocity between two surfaces in contact. Later, Lee and Tomizuka [18] and Erkorkmaz and Altintas [19] have applied simpler versions of this model to identify the friction dynamics in CNC drives. These models focus primarily on the static, Coulomb, and viscous friction regimes.

The main disadvantage of rigid body type models is that they fail to capture the effect of structural vibrations which becomes prevalent when high bandwidths are demanded in the control law. To address these issues, Varanasi and Nayfeh [20] and Erkorkmaz and Kamalzadeh [21] have worked on building Finite Element models and conducting frequency response experiments to identify the torsional and axial vibrations of ball screw drives. The backlash and motion loss in the nut interface have been identified by Kao et al. [22] and Cuttino et al. [23], with models of varying complexity. The volumetric and thermal errors, which influence the final tool positioning accuracy, were modeled by researchers at NIST in [24]. Several of the listed models have successfully been incorporated into the general feed drive template in the Virtual CNC shown in Figure 2.5.

Depending on circumstances, some of the dynamic factors listed above play a more dominant role than the others in determining the final accuracy of a feed drive system. In overall, experimental identification of models that capture the relevant dynamics is usually time consuming and needs to be performed by an engineer who is competent in control theory and sometimes metrology. The identification experiments may require the servo loop or the interpolator to be disconnected, in order to inject particular excitation signals to the drive system. When these factors are considered, building even basic virtual models of CNC drives can result in considerable downtime to the actual production machines, which is not always practical in a manufacturing environment.

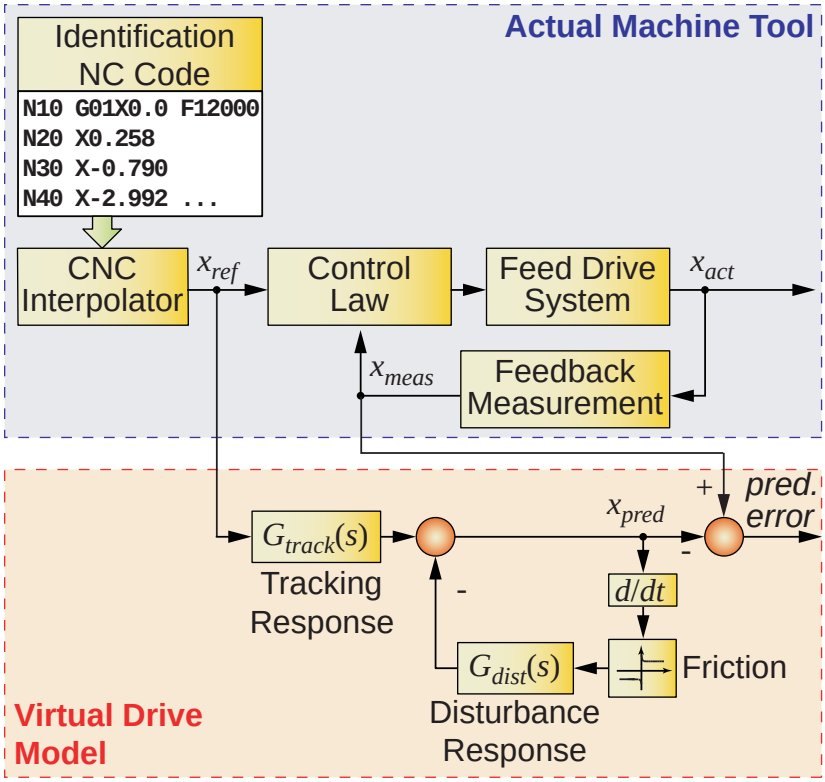

Figure 2.6. Overview of rapid identification technique.

To address these issues, a rapid identification strategy has been developed in this thesis, which has been reported in [25], [26], and [27]. The rapid identification technique, shown in Figure 2.6, consists of executing a short G-code experiment and collecting input and output data using the "motion capture" feature available on most CNC systems. The data is processed with the intention of reverse engineering the equivalent tracking and disturbance transfer functions of the closed loop drive system, and the guideway friction. It is shown that accurate prediction of the real machine's contouring capability for a variety of feed drive systems can be achieved through such virtual drive model.

One drawback of the rapid identification scheme is that the motion commands generated by the interpolator are smooth, typically up to the acceleration level (i.e. C^2 continuity), and therefore lack the persistence of excitation to allow accurate estimation of all model parameters using data captured for a short period of time. Furthermore, when feedforward control is used to widen the effective tracking bandwidth, majority of the stable axis

dynamics are cancelled out by placing poles and zeros inside a trajectory pre-filter [14], [15]. This cancellation renders the identification of closed loop dynamics very difficult. In either case, there is high likelihood that the identified parameters will not converge to their true values. Such a deviation is normally acceptable, as long as the identified model captures the dynamics of the real drive system with sufficient closeness in the frequency range of the CNC motion commands. In extreme cases this non-convergence can also result in the identification of critically stable or even unstable virtual drive models, which have very limited practical value.

In order to guarantee stability of the identified model, bounds need to be imposed on the closed loop pole locations. This results in the identification task to assume the form of a constrained minimization problem, which has been solved using the Lagrange Multipliers (LM) technique in [25], [26] and a Genetic Algorithm in [27]. LM theoretically yields the best possible parameter estimates for the collected data, and this strategy was found to be successful in identifying virtual drive parameters. However, it is a computationally lengthy approach and requires the use of a specialized symbolic solver like Matlab's Symbolic Math Toolbox [28], which significantly limits its portability for industrial implementation. On the other hand, the Genetic Algorithm (GA) is a slightly less exact approach but converges much faster than the LM solution, and can be easily be ported to different platforms as it does not require the use of a symbolic solver. The two approaches are explained in detail in Chapter 3 and Chapter 4.

2.4 Evolutionary Computation

Artificial Intelligence has been finding widespread use in solving complex engineering problems which are difficult to solve using traditional algebraic or gradient based optimization methods. There are three major areas of interest to engineers in the field of artificial Intelligence; these are fuzzy logic, neural networks, and evolutionary programming [29]. Fuzzy logic is used when the system does not have a direct relationship between the inputs and outputs. Fuzzy logic is usually used for transferring existing expert knowledge into automated decision making processes. Neural networks are used for mimicking

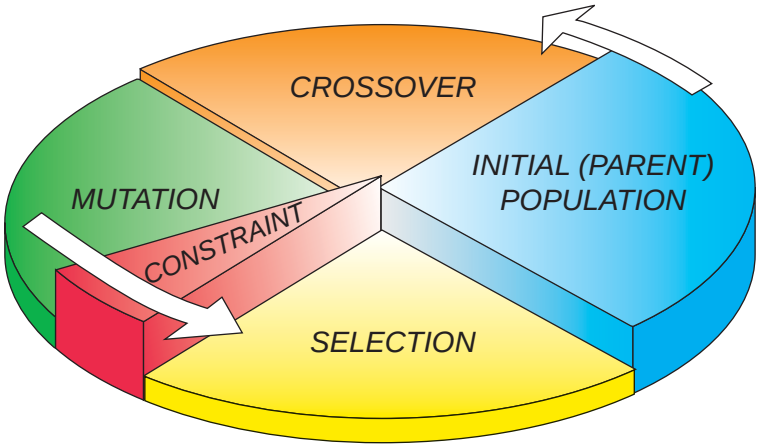

Figure 2.7. A Schematic of the Genetic Algorithm.

processes where the relationship between inputs and outputs are not exactly known, but can be "learned" through observation, expert knowledge or pattern recognition. Genetic Algorithms (GA's) relate to an evolutionary programming technique which applies the Principle of Natural Selection to find the best solution out of a large pool of candidates which undergo several cycles of evolution. This concept was pioneered by Holland in his book in 1975 [30]; however it is Fogel who made this technique practical in the 1980's, as an alternative to classical approaches, by mimicking the evolutionary process in organ cells [31]. The ability to constrain the search space with desired bounds lends Genetic Algorithms to be suitable for solving complex optimization problems in controller design and identification which are constrained, nonlinear, multivariable, and typically non-convex [32].

A schematic of the GA is shown in Figure 2.7, which cycles through five main processes. The first part of the cycle starts with a Parent Population of solution candidates. This population is used to produce a new generation in the Crossover phase, which inherits characteristics from the parent pairs. Randomness is introduced by perturbing the new solutions in the Mutation phase. After ensuring compliance with the given constraints [32], the solution candidates are evaluated for how well they minimize an overall objective. The best solutions are then carried forward to spawn the next generation using the Selection process. This cycle is repeated until the solution pool converges to the optimal result.

The main advantage of the Genetic Algorithm is the ease at which it can be adopted to solve different kinds of problems. The designer only requires to supply the objective function

and the constraints. Afterwards, the GA iteratively converges toward the optimal result. This allows problems which are difficult to solve by algebra or conventional numerical techniques to be efficiently handled. Although GA's have been around since the 1980's, it is with the recent increase in the availability of computational power that they have become more widespread. By restructuring the problem to streamline the computations and casting the search in terms of the right parameters, Genetic Algorithms can provide solutions at a rate which are comparable to deterministic calculations [33]. Problems such as airport traffic control [34], shortest traveling distance between multiple points [35], operation planning of NC processes [36], and AC motor modeling [37] have been successfully solved using GA's. Other applications in which GA's have been applied are identifying the dynamics of generators [38], [39], bearing stiffness and damping values in rotor assemblies [40], friction models in precision linear stages [41], and robotic applications [42][43][44].

. In this thesis, the GA is used to identify the equivalent command following and disturbance rejection properties and guideway friction in CNC machine tool drives, as explained in Chapter 4.

2.5 Summary

This chapter has presented a survey of academic literature and industrial practice relevant to virtual simulation of CNC systems, identification of feed drives, and the use of evolutionary programming to solve complex engineering problems. It is shown that virtual production simulations, as promising as they are, rely on the accuracy of the machine and process models that are available. Hence, there is a strong need to identify dynamic models of existing machine tools in a practical and reliable manner, while causing minimal disruption to their operation. To address these issues, the concept of rapid identification has been introduced, which will be further explained in the next two chapters.

Chapter 3

Rapid Identification Problem and Lagrange Multipliers Solution

3.1 Introduction

In this chapter, a mathematical framework is presented for solving the rapid identification problem. In Section 3.2, a generalized model is developed which captures the key dynamics of a large class of CNC drive systems. Based on this model, the constrained identification problem is constructed and the solution is formulated in Section 3.3, using the Lagrange Multipliers (LM) technique. Simulation and experimental results demonstrating the effectiveness of the LM solution are presented in Section 3.4. The conclusions are presented in Section 3.5.

3.2 Generalized Model for Closed Loop Axis Dynamics

In this section a dynamic model is developed which is applicable to a large class of CNC drives. This model can be used to describe the overall closed loop behavior of ball screw or linear drives, controlled with various feedback techniques such as P, PI, PD, PID, and P-PI cascade control, with or without feedforward dynamic or friction compensation. The model also considers the existence of nonlinear Coulomb friction, hence enabling the prediction of quadrant glitches and tracking errors that arise from sudden changes in the friction field during motion reversals. The main assumptions made in developing the model are: 1) Rigid body motion is dominant (i.e. flexible modes are not excited); 2) Actuator saturations are avoided; and 3) The effect of nonlinearities like torque ripples, backlash, and lead errors, are minor in comparison to the servo errors that originate from the interaction between the controller dynamics and the drive's rigid body motion. These conditions are typically realized on most feed drive systems.

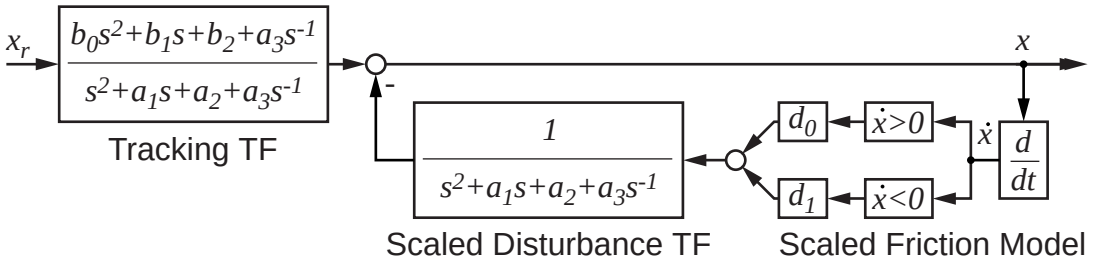

Figure 3.1. General representation of closed loop dynamics.

Two of the most common control structures used in CNC drives are shown in Figure 3.2. In Figure 3.2(a), the velocity loop is closed using proportional–integral (PI) control, and the position loop is closed using proportional (P) control. In Figure 3.2(b), the position loop is directly closed using a proportional-integral-derivative (PID) controller, which typically results in motor torque commands. In both cases, feedforward compensation of axis dynamics can be applied to widen the servo tracking bandwidth, in order to improve the positioning accuracy. In the figure, J [kgm^2] is the equivalent inertia and B [kgm^2/sec] is the viscous damping coefficient. u [V] is the torque command applied to the current amplifier, K [Nm/V] is the product of the amplifier gain (K_{amp} [A/V]), motor torque constant (K_t [Nm/A]), ball screw transmission gain (r_g [mm/rad]), and the gear ratio (n), if there is one, between the motor and ball screw ($K = K_{amp}K_t r_g n$). x_r [mm] is the commanded and x [mm] is the actual axis position. In both cases, the equivalent closed loop dynamics can be represented in the form:

$$x(s) = \underbrace{\frac{b_0 s^2 + b_1 s + b_2 + a_3 \frac{1}{s}}{s^2 + a_1 s + a_2 + a_3 \frac{1}{s}}}_{Gtrack(s)} \cdot x_r(s) - \underbrace{\frac{K/J}{s^2 + a_1 s + a_2 + a_3 \frac{1}{s}}}_{Gdist(s)} \cdot d(s) \qquad (3.1)$$

Above $G_{track}(s)$ and $G_{dist}(s)$ are the equivalent tracking and disturbance transfer functions. The most dominant source of nonlinear friction in feed drives is Coulomb and static friction. A full model to describe the Stribeck curve requires extensive testing and identification procedures to be carried out [17]. In this work, Coulomb friction is considered

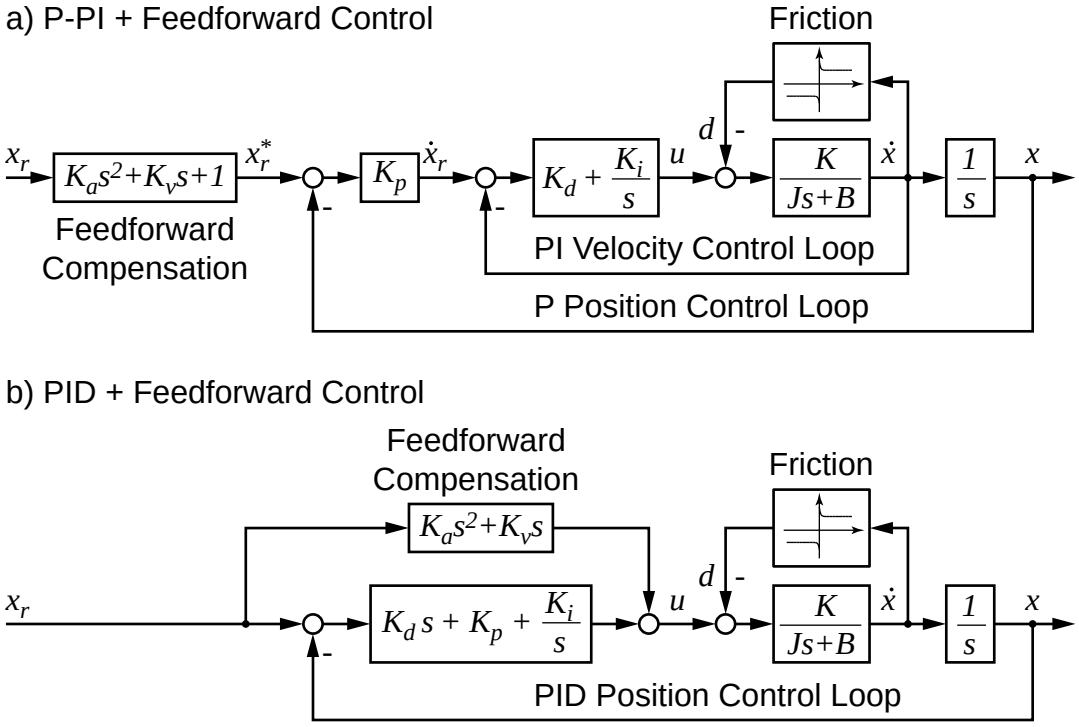

Figure 3.2. Common control structures used in CNC drives.

as the main contributor to contouring and tracking errors during motion reversals. The friction model is expressed in the form:

$$d = d^+ \cdot \mathrm{PV}(\dot{x}) + d^- \cdot \mathrm{NV}(\dot{x}) \tag{3.2}$$

where $\mathrm{PV}(\dot{x})$ is a binary function which assumes a value of "1" when the axis velocity is positive and "0" otherwise. $\mathrm{NV}(\dot{x})$ takes a value of "1" when the axis velocity is negative and "0" otherwise. d^+ and d^- are the control signal equivalent values of Coulomb friction for positive and negative directions of motion. Substituting the friction model in Eq. (3.2) into the closed loop linear dynamics in Eq. (3.1) yields the general axis model shown in Figure 3.1:

$$\begin{aligned}[s^2 + a_1 s + a_2 + a_3 \frac{1}{s}] \cdot x(s) \\ = [b_0 s^2 + b_1 s + b_2 + a_3 \frac{1}{s}] \cdot x_r(s) - [\mathrm{PV}(\dot{x}) \cdot d_0 + \mathrm{NV}(\dot{x}) \cdot d_1]\end{aligned} \tag{3.3}$$

For the P-PI structure, the model parameters are obtained as:

$$\left.\begin{array}{lll} a_1 = \dfrac{B + KK_d}{J} & , \; a_2 = \dfrac{K(K_d K_p + K_i)}{J} & , \quad a_3 = \dfrac{KK_p K_i}{J} \\ b_0 = \dfrac{KK_p K_d K_a}{J} & , \; b_1 = \dfrac{KK_p (K_d K_v + K_a K_i)}{J} & \\ b_2 = \dfrac{KK_p (K_d + K_v K_i)}{J} & , \; d_0 = \dfrac{K}{J} d^+ & , \quad d_1 = \dfrac{K}{J} d^- \end{array}\right\} \tag{3.4}$$

In the PID structure, the parameters become:

$$\left.\begin{array}{llll} a_1 = \dfrac{B + KK_d}{J} & , \; a_2 = \dfrac{KK_p}{J} & , \; a_3 = \dfrac{KK_i}{J} & , \; b_0 = \dfrac{KK_a}{J} \\ b_1 = \dfrac{K(K_d + K_v)}{J} & , \; b_2 = a_2 = \dfrac{KK_p}{J} & , \; d_0 = \dfrac{K}{J} d^+ & , \; d_1 = \dfrac{K}{J} d^- \end{array}\right\} \tag{3.5}$$

It should be noted that the derived model in Eq. (3.3) allows the closed loop dynamics for a large class of feed drive systems to be represented with only 8 parameters (3 poles, 3 zeros, and 2 friction amplitudes). This model can also be used to capture the dominant dynamics of drive systems controlled with more complex controllers such as state feedback and pole-placement control. The time-dependent terms correspond to physically meaningful variables such as commanded and actual axis position (x_r, x), velocity ($\dot{x}_r$, $\dot{x}$), acceleration ($\ddot{x}_r$, $\ddot{x}$), and integrated tracking error ($\int_0^t [x_r(\tau) - x(\tau)] d\tau$). These profiles can be captured on the fly in most CNC systems. If necessary, velocity and acceleration and integrated tracking error profiles can be constructed through numerical differentiation or integration of discrete-time position signals (i.e. $\hat{\dot{x}}_k = (x_{k+1} - x_{k-1})/(2T_s)$, $\hat{\ddot{x}}_k = (\hat{\dot{x}}_{k+1} - \hat{\dot{x}}_{k-1})/(2T_s)$, $e_{i,k} = T_s \sum_{m=1}^{k} (x_{r,m} - x_m)$ where T_s: sampling period). The derived model can also capture the response of simpler control structures, which may or may not contain feedforward, integral, or derivative action. If feedforward friction compensation is used in the control law, this results in lower values to be estimated for the remaining Coulomb friction. Finally, the

closed loop model is linear with respect to its parameters, allowing Least Squares type of identification techniques to be applied [45].

3.3 Constrained Parameter Identification using Lagrange Multipliers

As shown in Figure 2.6 in Chapter 2, the rapid identification experiment is conducted by executing a series of NC instructions comprised of short random linear movements, to deliver as much excitation as possible to the drive system. The maximum feed and acceleration values are set below the physical limits of the drives, in order to avoid actuator saturation. The overall displacement range is selected such that the maximum feed can only be reached when traveling from one end of the motion range to the other. The commanded displacement between consecutive NC blocks is generally too short to reach the desired maximum feedrate, which enables the performance of the drive to be observed for a wide range of feeds within the machine's working envelope. The execution of multiple back and forth movements at different velocities allow for the effect of Coulomb friction, which brings amplitude dependence into the drive model, to be clearly observed. In order to deliver the excitation in as high frequency range as possible, smooth acceleration profiling (i.e. "S-curve" functionality) should be disabled in the interpolator, if possible. This results in trapezoidal and triangular velocity transitions, which provide higher frequency content, as opposed to parabolic velocity transitions.

The axis position commands and encoder measurements ($x_{r,k}$ and x_k) are collected while running the identification NC code. The data collection is carried out at the control loop period T_s for a total of N samples. The objective is to find the parameters (a_1, a_2, a_3, b_0, b_1, b_2, d_0, d_1) for the dynamic model in Eq. (3.3) such that the discrepancy between measured (x_k) and predicted ($\hat{x}_k$) axis movements is minimized in a least squares sense:

$$\text{Objective: Minimize} \quad f = \frac{1}{2}\sum_{k=1}^{N}[x_k - \hat{x}_k]^2 \tag{3.6}$$

The motion commands generated by the interpolator are relatively smooth and generally lack the persistence of excitation for all estimated parameters to converge to their true values, even though only rigid body motion is considered. This is not a major problem, as long as the identified drive model captures the key dynamics of the real system within the frequency range of the CNC motion commands. However, incorrect estimation of the drive dynamics may also result in unstable or poorly damped pole locations, which have limited practical value for conducting virtual manufacturing simulations. In order to avoid this problem and guarantee stability of the identified drive models, bounds need to be imposed on the frequency and damping ratio values of the closed loop poles. The characteristic polynomial in Eq. (3.3) and its pole locations are:

$$\begin{aligned} & s^3 + a_1 s^2 + a_2 s + a_3 = (s+p)(s^2 + 2\zeta\omega_n s + \omega_n^2) = \prod_{k=1}^{3}(s - p_k) \\ & p_1 = -p\,,\ \ p_{2,3} = -\zeta\omega_n \pm j\omega_n\sqrt{1-\zeta^2} \end{aligned} \tag{3.7}$$

As the damping ratio becomes large ($\zeta >> 1$), the third closed loop pole starts approaching zero (i.e. $p_3 \to 0^-$), which is undesirable. In order to guarantee the necessary stability margins, the closed loop pole frequencies need to be constrained with lower bounds and the damping ratio needs to be constrained with lower and upper bounds, resulting in the below statement of identification constraints:

$$\text{Constraints}: \left.\begin{matrix} h_1 : p \geq p_{\min} \ \ , \ \ h_2 : \omega_n \geq \omega_{n,\min} \\ h_3 : \zeta \geq \zeta_{\min} \ \ , \ \ h_4 : \zeta \leq \zeta_{\max} \end{matrix}\right\} \tag{3.8}$$

where $p_{\min} > 0$, $\omega_{n.\min} > 0$, and $\zeta_{\max} > \zeta_{\min} > 0$. Assuming that $\zeta_{\max} > 1$, the allowable pole locations are shown in Figure 3.3. In the following, the identification problem is solved as a constrained minimization problem using Lagrange Multipliers technique with Kuhn-Tucker switching conditions [4], in order to handle the inequality constraints.

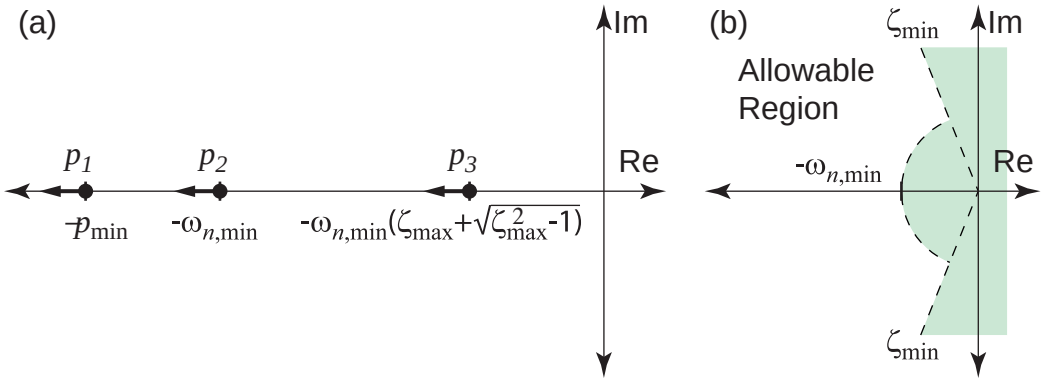

Figure 3.3. Allowable locations for (a) real, (b) complex poles.

Assuming that the commanded position ($x_{r,k}$), velocity ($\dot{x}_{r,k}$), acceleration ($\ddot{x}_{r,k}$), measured velocity ($\dot{x}_k$) and acceleration ($\ddot{x}_k$), and integrated tracking error ($e_i = T_s \sum_{m=1}^{k} (x_{r,m} - x_m)$) are available at the k^{th} sample, the axis position can be predicted by taking the inverse Laplace transform of Eq. (3.3):

$$\hat{x}_k = \alpha_i e_{i,k} - \alpha_1 \dot{x}_k - \alpha_2 \ddot{x}_k + \beta_0 x_{r,k} + \beta_1 \dot{x}_{r,k} + \beta_2 \ddot{x}_{r,k} - \mathrm{PV}(\dot{x}_k) \cdot \delta^+ - \mathrm{NV}(\dot{x}_k) \cdot \delta^- \qquad (3.9)$$

The model parameters, normalized with respect to a_2 (i.e. coefficient for axis position) are obtained as:

$$\left.\begin{array}{lll} \alpha_2 = 1/a_2 & , \ \alpha_1 = a_1/a_2 & , \ \alpha_i = a_3/a_2 \\ \beta_2 = b_0/a_2 & , \ \beta_1 = b_1/a_2 & , \ \beta_0 = b_2/a_2 \\ \delta^+ = d_0/a_2 & , \ \delta^- = d_1/a_2 & \end{array}\right\} \qquad (3.10)$$

The identification problem is solved to determine the vector of normalized model parameters ($\boldsymbol{\theta}$). Clustering the axis position measurements into an output vector: $\mathbf{Y}$ and defining the regressor matrix $\boldsymbol{\Phi}$,

$$\mathbf{Y} = [x_1 \quad x_2 \quad \dots \quad x_N]^T$$

$$\mathbf{\Phi} = \begin{bmatrix} e_{i,1} & -\dot{x}_1 & -\ddot{x}_1 & x_{r,1} & \dot{x}_{r,1} & \ddot{x}_{r,1} & -\mathrm{PV}(\dot{x}_1) & -\mathrm{NV}(\dot{x}_1) \\ e_{i,2} & -\dot{x}_2 & -\ddot{x}_2 & x_{r,2} & \dot{x}_{r,2} & \ddot{x}_{r,2} & -\mathrm{PV}(\dot{x}_2) & -\mathrm{NV}(\dot{x}_2) \\ \vdots & \vdots & \vdots & \vdots & \vdots & \vdots & \vdots & \vdots \\ e_{i,N} & -\dot{x}_N & -\ddot{x}_N & x_{r,N} & \dot{x}_{r,N} & \ddot{x}_{r,N} & -\mathrm{PV}(\dot{x}_N) & -\mathrm{NV}(\dot{x}_N) \end{bmatrix} \tag{3.11}$$

$$\boldsymbol{\theta} = [\alpha_i \quad \alpha_1 \quad \alpha_2 \quad \beta_0 \quad \beta_1 \quad \beta_2 \quad \delta^+ \quad \delta^-]^T$$

the objective function in Eq. (3.6) is re-expressed as:

$$\text{Objective: Minimize} \quad f = \frac{1}{2}(\mathbf{Y} - \mathbf{\Phi\theta})^T (\mathbf{Y} - \mathbf{\Phi\theta}) \tag{3.12}$$

The inequality constraints in Eq. (3.8) are transformed into equality constraints using the slacking variables $\sigma_1, \sigma_2, \sigma_3, \sigma_4 \in \Re$:

$$\left.\begin{array}{lll} h_1 : p - p_{\min} \geq 0 & \Rightarrow & h_1 = p - p_{\min} - \sigma_1^2 = 0 \\ h_2 : \omega_n - \omega_{n,\min} \geq 0 & \Rightarrow & h_2 = \omega_n - \omega_{n,\min} - \sigma_2^2 = 0 \\ h_3 : \zeta - \zeta_{\min} \geq 0 & \Rightarrow & h_3 = \zeta - \zeta_{\min} - \sigma_3^2 = 0 \\ h_4 : -\zeta + \zeta_{\max} \geq 0 & \Rightarrow & h_4 = -\zeta + \zeta_{\max} - \sigma_4^2 = 0 \end{array}\right\} \quad \text{Constraints:} \tag{3.13}$$

Considering Eq. (3.7) and (3.10), the first three optimization variables ($\alpha_i, \alpha_1, \alpha_2$) are related to the constraint variables (p , ω_n, ζ) as:

$$\alpha_i = \frac{a_3}{a_2} = \frac{p\omega_n^2}{\omega_n^2 + 2p\zeta\omega_n}, \quad \alpha_1 = \frac{a_1}{a_2} = \frac{p + 2\zeta\omega_n}{\omega_n^2 + 2p\zeta\omega_n}, \quad \alpha_2 = \frac{1}{a_2} = \frac{1}{\omega_n^2 + 2p\zeta\omega_n} \tag{3.14}$$

The differential relationship between these variables can be constructed as by taking the total differential of the expressions in Eq. (3.14):

$$\begin{bmatrix} d\alpha_i \\ d\alpha_1 \\ d\alpha_2 \end{bmatrix} = \begin{bmatrix} \partial\alpha_i/\partial p & \partial\alpha_i/\partial\omega_n & \partial\alpha_i/\partial\zeta \\ \partial\alpha_1/\partial p & \partial\alpha_1/\partial\omega_n & \partial\alpha_1/\partial\zeta \\ \partial\alpha_2/\partial p & \partial\alpha_2/\partial\omega_n & \partial\alpha_2/\partial\zeta \end{bmatrix} \cdot \begin{bmatrix} dp \\ d\omega_n \\ d\zeta \end{bmatrix} = \mathbf{G} \cdot \begin{bmatrix} dp \\ d\omega_n \\ d\zeta \end{bmatrix}$$

$$\text{where: } \mathbf{G} = \frac{\begin{bmatrix} \omega_n^2 & 2p^2\zeta & -2p^2\omega_n \\ 1-4\zeta^2 & -2(\zeta\omega_n^2 + p\omega_n + p^2\zeta)/\omega_n^2 & -2(p^2-\omega_n^2)/\omega_n \\ -2\zeta/\omega_n & -2(\omega_n + p\zeta)/\omega_n^2 & -2p/\omega_n \end{bmatrix}}{(\omega_n + 2p\zeta)^2} \tag{3.15}$$

The inverse gradient can then be obtained by inverting the matrix $\mathbf{G}$:

$$\begin{bmatrix} dp \\ d\omega_n \\ d\zeta \end{bmatrix} = \begin{bmatrix} \partial p/\partial\alpha_i & \partial p/\partial\alpha_1 & \partial p/\partial\alpha_2 \\ \partial\omega_n/\partial\alpha_i & \partial\omega_n/\partial\alpha_1 & \partial\omega_n/\partial\alpha_2 \\ \partial\zeta/\partial\alpha_i & \partial\zeta/\partial\alpha_1 & \partial\zeta/\partial\alpha_2 \end{bmatrix} \cdot \begin{bmatrix} d\alpha_i \\ d\alpha_1 \\ d\alpha_2 \end{bmatrix} = \mathbf{G}^{-1} \cdot \begin{bmatrix} d\alpha_i \\ d\alpha_1 \\ d\alpha_2 \end{bmatrix}, \quad \text{where:}$$

$$\mathbf{G}^{-1} = \frac{\begin{bmatrix} \omega_n & p^2\omega_n & -p^3\omega_n \\ (p-2\zeta\omega_n)/2 & -p\omega_n^2/2 & \omega_n^3(2p\zeta-\omega_n)/2 \\ -\dfrac{p\zeta - 2\zeta^2\omega_n + \omega_n}{2\omega_n} & -\dfrac{(p\zeta-\omega_n)\omega_n}{2} & \dfrac{(2p\zeta^2 - p - \zeta\omega_n)\omega_n^2}{2} \end{bmatrix}}{(p^2 - 2p\zeta\omega_n + \omega_n^2)/(\omega_n + 2p\zeta)} \tag{3.16}$$

The constrained optimization problem is solved by constructing the augmented objective function $f'(\boldsymbol{\theta}, \lambda_1, \lambda_2, \lambda_3, \lambda_4, \sigma_1, \sigma_2, \sigma_3, \sigma_4)$ and setting its partial derivatives with respect to the optimization variables ($\boldsymbol{\theta}$), Lagrange multipliers ($\lambda_1, \lambda_2, \lambda_3, \lambda_4$) and slacking variables ($\sigma_1, \sigma_2, \sigma_3, \sigma_4$) to zero:

$$f' = \underbrace{\frac{1}{2}(\mathbf{Y} - \boldsymbol{\Phi}\boldsymbol{\theta})^T(\mathbf{Y} - \boldsymbol{\Phi}\boldsymbol{\theta})}_{f} + \underbrace{\lambda_1(p - p_{\min} - \sigma_1^2)}_{\lambda_1 h_1} + \underbrace{\lambda_2(\omega_n - \omega_{n,\min} - \sigma_2^2)}_{\lambda_2 h_2}$$
$$+ \underbrace{\lambda_3(\zeta - \zeta_{\min} - \sigma_3^2)}_{\lambda_3 h_3} + \underbrace{\lambda_4(-\zeta + \zeta_{\max} - \sigma_4^2)}_{\lambda_4 h_4} \tag{3.17}$$

$$\text{Solution: } \begin{cases} \partial f'/\partial\boldsymbol{\theta} = \mathbf{0}, \partial f'/\partial\lambda_1 = 0, \partial f'/\partial\lambda_2 = 0, \partial f'/\partial\lambda_3 = 0, \partial f'/\partial\lambda_4 = 0 \\ \partial f'/\partial\sigma_1 = 0, \partial f'/\partial\sigma_2 = 0, \partial f'/\partial\sigma_3 = 0, \partial f'/\partial\sigma_4 = 0 \end{cases}$$

The partial derivative with respect to the optimization variables yields a system of 8 equations with resemblance to the standard least-squares estimation problem [45]:

$$\partial f'/\partial \boldsymbol{\theta} = \mathbf{0} \Rightarrow \boldsymbol{\Phi}^T \boldsymbol{\Phi}\boldsymbol{\theta} + \lambda_1 \frac{\partial p}{\partial \boldsymbol{\theta}} + \lambda_2 \frac{\partial \omega_n}{\partial \boldsymbol{\theta}} + \lambda_3 \frac{\partial \zeta}{\partial \boldsymbol{\theta}} - \lambda_4 \frac{\partial \zeta}{\partial \boldsymbol{\theta}} = \boldsymbol{\Phi}^T \mathbf{Y} \tag{3.18}$$

Defining the matrices $\mathbf{P}$ and $\mathbf{R}$ as:

$$\mathbf{P} = \begin{bmatrix} p_{11} & \cdots & p_{18} \\ \vdots & \ddots & \vdots \\ p_{81} & \cdots & p_{88} \end{bmatrix} = \boldsymbol{\Phi}^T \boldsymbol{\Phi} \quad , \quad \mathbf{R} = \begin{bmatrix} r_1 \\ \vdots \\ r_8 \end{bmatrix} = \boldsymbol{\Phi}^T \mathbf{Y} \tag{3.19}$$

The system in Equation (3.18) can be expanded as:

$$\begin{aligned}
&\left(\begin{array}{l} p_{11}\alpha_i + p_{12}\alpha_1 + p_{13}\alpha_2 + p_{14}\beta_0 + p_{15}\beta_1 + p_{16}\beta_2 + p_{17}\delta^+ + p_{18}\delta^- \\ + \lambda_1(\partial p/\partial \alpha_i) + \lambda_2(\partial \omega_n/\partial \alpha_i) + (\lambda_3 - \lambda_4)(\partial \zeta/\partial \alpha_i) \end{array}\right) &= r_1 \\
&\left(\begin{array}{l} p_{21}\alpha_i + p_{22}\alpha_1 + p_{23}\alpha_2 + p_{24}\beta_0 + p_{25}\beta_1 + p_{26}\beta_2 + p_{27}\delta^+ + p_{28}\delta^- \\ + \lambda_1(\partial p/\partial \alpha_1) + \lambda_2(\partial \omega_n/\partial \alpha_1) + (\lambda_3 - \lambda_4)(\partial \zeta/\partial \alpha_1) \end{array}\right) &= r_2 \\
&\left(\begin{array}{l} p_{31}\alpha_i + p_{32}\alpha_1 + p_{33}\alpha_2 + p_{34}\beta_0 + p_{35}\beta_1 + p_{36}\beta_2 + p_{37}\delta^+ + p_{38}\delta^- \\ + \lambda_1(\partial p/\partial \alpha_2) + \lambda_2(\partial \omega_n/\partial \alpha_2) + (\lambda_3 - \lambda_4)(\partial \zeta/\partial \alpha_2) \end{array}\right) &= r_3 \\
&p_{41}\alpha_i + p_{42}\alpha_1 + p_{43}\alpha_2 + p_{44}\beta_0 + p_{45}\beta_1 + p_{46}\beta_2 + p_{47}\delta^+ + p_{48}\delta^- &= r_4 \\
&p_{51}\alpha_i + p_{52}\alpha_1 + p_{53}\alpha_2 + p_{54}\beta_0 + p_{55}\beta_1 + p_{56}\beta_2 + p_{57}\delta^+ + p_{58}\delta^- &= r_5 \\
&p_{61}\alpha_i + p_{62}\alpha_1 + p_{63}\alpha_2 + p_{64}\beta_0 + p_{65}\beta_1 + p_{66}\beta_2 + p_{67}\delta^+ + p_{68}\delta^- &= r_6 \\
&p_{71}\alpha_i + p_{72}\alpha_1 + p_{73}\alpha_2 + p_{74}\beta_0 + p_{75}\beta_1 + p_{76}\beta_2 + p_{77}\delta^+ + p_{78}\delta^- &= r_7 \\
&p_{81}\alpha_i + p_{82}\alpha_1 + p_{83}\alpha_2 + p_{84}\beta_0 + p_{85}\beta_1 + p_{86}\beta_2 + p_{87}\delta^+ + p_{88}\delta^- &= r_8
\end{aligned} \tag{3.20}$$

The partial derivatives with respect to the Lagrange multipliers yield the constraint equations:

$$\begin{aligned}
\partial f'/\partial \lambda_1 = 0 \quad &\Rightarrow \quad p - p_{\min} - \sigma_1^2 = 0 \\
\partial f'/\partial \lambda_2 = 0 \quad &\Rightarrow \quad \omega_n - \omega_{n,\min} - \sigma_2^2 = 0 \\
\partial f'/\partial \lambda_3 = 0 \quad &\Rightarrow \quad \zeta - \zeta_{\min} - \sigma_3^2 = 0 \\
\partial f'/\partial \lambda_4 = 0 \quad &\Rightarrow \quad -\zeta + \zeta_{\max} - \sigma_4^2 = 0
\end{aligned} \tag{3.21}$$

The partial derivatives with respect to the slacking variables yield the Kuhn-Tucker switching conditions [4]:

$$\begin{aligned} \partial f'/\partial\sigma_1 = 0 \quad &\Rightarrow \quad -2\lambda_1\sigma_1 = 0 \\ \partial f'/\partial\sigma_2 = 0 \quad &\Rightarrow \quad -2\lambda_2\sigma_2 = 0 \\ \partial f'/\partial\sigma_3 = 0 \quad &\Rightarrow \quad -2\lambda_3\sigma_3 = 0 \\ \partial f'/\partial\sigma_4 = 0 \quad &\Rightarrow \quad -2\lambda_4\sigma_4 = 0 \end{aligned} \tag{3.22}$$

These equations imply that the i^{th} constraint is either active ($\sigma_i = 0$, equality state), or inactive ($\lambda_i = 0$, inequality state) [4]. Considering that there are four constraints, this leads to $2^4 = 16$ possible constraint activation scenarios, which have been shown in Table 3.1. Among these, Cases 10, 12, 14, and 16 are infeasible, since they correspond to $\zeta = \zeta_{\max}$ and $\zeta = \zeta_{\min}$ holding at the same time, which is not possible if $\zeta_{\max} > \zeta_{\min}$. Case 1 corresponds to the unconstrained solution of Eq. (3.12), which is the result of the standard Least Squares technique [45]. If the solution for this case violates the bounds in Eq. (3.8), then the remaining 11 cases need to be evaluated one by one. For each feasible case, the system in Eqs. (3.20)-(3.21) is reconstructed and solved by substituting in the known values of Lagrange multipliers and slacking variables from Table 3.1, the partial derivatives ($\partial p/\partial\alpha_i$, $\partial p/\partial\alpha_1$, $\partial p/\partial\alpha_2$, $\partial\omega_n/\partial\alpha_i$, $\partial\omega_n/\partial\alpha_1$, $\partial\omega_n/\partial\alpha_2$, $\partial\zeta/\partial\alpha_i$, $\partial\zeta/\partial\alpha_1$, $\partial\zeta/\partial\alpha_2$) from Eq. (3.16), and replacing the α_i, α_1, α_2 terms with their expressions in terms of p, ω_n, and ζ from Eq. (3.14). Each nonlinear equation system is solved using Matlab's Symbolic Math Toolbox [28], resulting in a solution (or in some cases, multiple solutions) for p, ω_n, ζ, β_0, β_1, β_2, δ^+, δ^-, the unknown Lagrange multipliers and the slacking variables. The normalized denominator parameters α_i, α_1, α_2, are computed using Eq. (3.14). Each solution is checked for constraint feasibility (Eq. (3.13)) and feasible solutions are evaluated for how well they minimize the objective function (Eq. (3.12)). The feasible solution that yields the lowest value for the objective is selected as the optimal parameter set (a_1, a_2, a_3, b_0, b_1, b_2, d_0, d_1) for the dynamic model in Eq.(3.3).

Table 3.1. Possible cases of constraint activation (cases 10, 12, 14, and 16 are infeasible).

Case	λ_1	σ_1	λ_2	σ_2	λ_3	σ_3	λ_4	σ_4
1	*0*		*0*		*0*		*0*	
2	*0*		*0*			*0*	*0*	
3	*0*			*0*	*0*		*0*	
4	*0*			*0*		*0*	*0*	
5		*0*	*0*		*0*		*0*	
6		*0*	*0*			*0*	*0*	
7		*0*		*0*	*0*		*0*	
8		*0*		*0*		*0*	*0*	
9	*0*		*0*		*0*			*0*
10	*0*		*0*			*0*		*0*
11	*0*			*0*	*0*			*0*
12	*0*			*0*		*0*		*0*
13		*0*	*0*		*0*			*0*
14		*0*	*0*			*0*		*0*
15		*0*		*0*	*0*			*0*
16		*0*		*0*		*0*		*0*

3.4 Simulation and Experimental Results

The effectiveness of the proposed identification strategy has been verified in simulations and experimental case studies conducted on virtual and actual feed drives. Since virtual axis dynamics are already known, the simulations allow a comparison between the true and identified drive parameters. The experiments were conducted to validate practical effectiveness of the rapid identification strategy.

The NC code used in the tests is shown in Table 3.2, which consists of 200 random linear movements commanded within a range of ±10 [mm] with a maximum feedrate of 200 [mm/sec]. Due to the short travel distance between consecutive position commands, this velocity is not reached. Instead, the drive's response is observed for a wide range of

velocities, as intended. The maximum acceleration and deceleration values for the interpolator were set to 2000 [mm/sec^2], which correspond to the limits of the drive system. The S-curve functionality in the interpolator was disabled, which produced trapezoidal velocity profiles with sharper motion transients. This was done to improve the parameter convergence. The data was collected at a sampling period of T_s=1 [msec] for a duration of 22 [sec]. A sample data set captured for a window of 1 [sec] is shown in Figure 3.4. The signals comprise of commanded, measured, and modeled (identified) position profiles.

In applying the Lagrange Multipliers solution, the pole location bounds were selected as $p_{\min} = \omega_{n,\min}$=6.28 [rad/sec] (1 [Hz]), $\zeta_{\min}$=0.2 [ ], and $\zeta_{\max}$=2.0 [ ]. The LM solution was implemented in Matlab on a Pentium IV computer. The use of the Symbolic Math Toolbox brought significant overhead to the computation of the solution, which sometimes took up to 15-20 minutes when all constraint activation scenarios needed to be checked. Nevertheless, the models identified with the LM technique were quite successful in replicating the real drive systems' dynamic response, as demonstrated in the following subsections.

3.4.1 Simulation Results

In the simulations, a virtual model of a Fadal VMC 2216 machining center was used, which was constructed through careful identification of the rigid body dynamics, nonlinear guideway friction, amplifier current limits, nut backlash, DAC quantization, and encoder measurement noise This model had been thoroughly verified in tracking and contouring experiments conducted on the real machine using different control schemes in earlier work [8]. The simulations were conducted considering different control structures to be implemented on the machine, such as P-PI cascade, PID, and adaptive sliding mode control.

Table 3.2. Identification NC code.

N0000 G00 X0.000 F12000	...
N0010 G01 X 0.258	N1630 G01 X-8.131
N0020 G01 X-0.790	N1640 G01 X-5.721
N0030 G01 X-2.992	N1650 G01 X 1.918
N0040 G01 X-8.099	N1660 G01 X-8.511
N0050 G01 X-1.327	N1670 G01 X 8.689
N0060 G01 X 4.185	N1680 G01 X-0.193
N0070 G01 X-7.681	N1690 G01 X-0.128
N0080 G01 X-8.438	N1700 G01 X-4.498
N0090 G01 X-2.615	N1710 G01 X 1.432
N0100 G01 X-9.327	N1720 G01 X 7.033
N0110 G01 X-6.157	N1730 G01 X 3.820
N0120 G01 X-0.573	N1740 G01 X 6.886
N0130 G01 X-7.102	N1750 G01 X-5.564
N0140 G01 X 4.357	N1760 G01 X 7.172
N0150 G01 X 3.234	N1770 G01 X-2.652
N0160 G01 X-1.363	N1780 G01 X 0.551
N0170 G01 X-1.079	N1790 G01 X 4.521
N0180 G01 X 0.167	N1800 G01 X-9.637
N0190 G01 X 0.562	N1810 G01 X-1.713
N0200 G01 X 1.458	N1820 G01 X 8.878
N0210 G01 X-2.784	N1830 G01 X9.849
N0220 G01 X-3.270	N1840 G01 X-5.730
N0230 G01 X-6.535	N1850 G01 X-4.483
N0240 G01 X-8.278	N1860 G01 X 0.362
N0250 G01 X-2.133	N1870 G01 X 5.308
N0260 G01 X 6.087	N1880 G01 X-7.907
N0270 G01 X-9.778	N1890 G01 X-5.381
N0280 G01 X-5.338	N1900 G01 X-3.796
N0290 G01 X 8.677	N1910 G01 X 2.959
N0300 G01 X-5.464	N1920 G01 X-3.515
N0310 G01 X 5.719	N1930 G01 X-1.919
N0320 G01 X-1.785	N1940 G01 X 4.187
N0330 G01 X-7.612	N1950 G01 X 9.234
N0340 G01 X 2.687	N1960 G01 X 3.739
N0350 G01 X 7.248	N1970 G01 X 6.345
N0360 G01 X-6.835	N1980 G01 X-6.731
N0370 G01 X 2.024	N1990 G01 X 9.038
N0380 G01 X-7.648	N2000 G01 X-2.641
...	N2010 G01 X 0.000

P-PI Cascade Controlled System

The rapid identification strategy was first evaluated on a P-PI cascade controlled drive system. The identification converged to the unconstrained solution without any of the stability constraints (Eq.(3.21)) becoming active. The true and estimated closed loop parameters are summarized in Table 3.3. A comparison between the true and estimated tracking and disturbance frequency response functions (FRF's) is presented in Figure 3.5. As can be noted in the table, there is discrepancy between the true and estimated pole locations. Although the slowest pole (p_3) at 4.68 [Hz] is captured with reasonable closeness at 4.88 [Hz] in x and y axes, the complex conjugate poles (p_1 and p_2) which actually have a frequency of 36.26 [Hz] are estimated as a pair of real poles at 368.80 and 47.84 [Hz] for x, and 436.91 and 45.52 [Hz] for y axes. The zero (z_3) at 21.88 and 21.90 [Hz] in the x and y axes is closely estimated at 23 and 22.81 [Hz] respectively. In addition, there is around 16.9× and 18.4× mismatch between the estimated and true friction parameters (d_0 and d_1) in x and y axes.

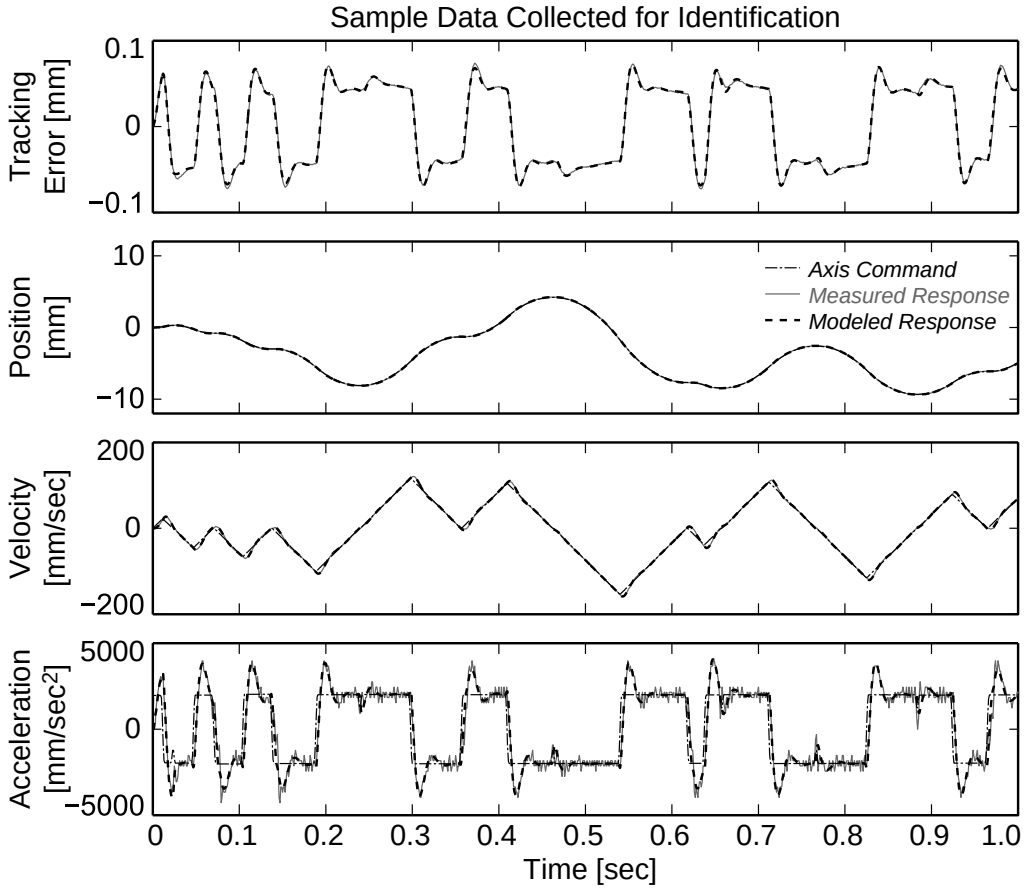

Figure 3.4. Identification trajectory captured in VCNC.

Considering the FRF's shown in Figure 3.5 (a) and (b) it is seen that the identified transfer functions are able to represent the tracking characteristics of the x and y axes accurately up to a frequency range of 30 [Hz], which is reasonably wide for tracking most CNC motion commands.

Table 3.3.Actual and estimated closed loop parameters for P-PI controlled drive system.

		X Axis				Y Axis			
		Actual		Estimated		Actual		Estimated	
Parameters	a_1	372.76		2648.46		372.76		3061.86	
	a_2	62009.83		776813.58		61999.31		878064.60	
	a_3	1527104.87		21349028.29		1527104.86		24070716.71	
	b_0	0		1.08		0		1.19	
	b_1	0		-415.03		0		-472.93	
	b_2	11106.33		65194.67		11095.82		75718.61	
	d_0	441		7210		409		7523	
	d_1	-302		-5277		-388		-7160	
Poles and Zeros		Frequency [Hz]	Damping [ ]	Frequency [Hz]	Damping [ ]	Frequency [Hz]	Damping [ ]	Frequency [Hz]	Damping [ ]
Poles	p_1	36.26	0.75	368.80	1.00	36.26	0.75	436.91	1.00
	p_2	36.26	0.75	47.84	1.00	36.26	0.75	45.52	1.00
	p_3	4.68	1.00	4.88	1.00	4.68	1.00	4.88	1.00
Zeros	z_1	–	–	58.91	-0.72	–	–	59.74	-0.72
	z_2	–	–	58.91	-0.72	–	–	59.74	-0.72
	z_3	21.88	1.00	23.00	1.00	21.90	1.00	22.81	1.00

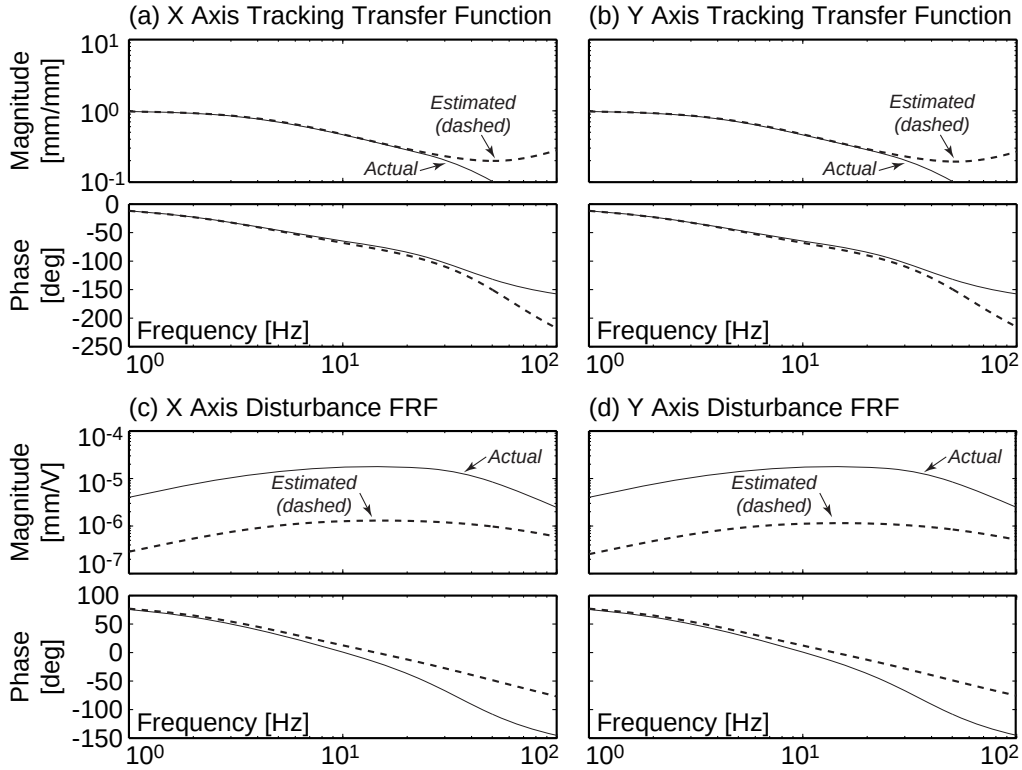

Figure 3.5. Estimated and actual tracking and disturbance frequency response functions (FRF's) for P-PI controlled servo system (simulation).

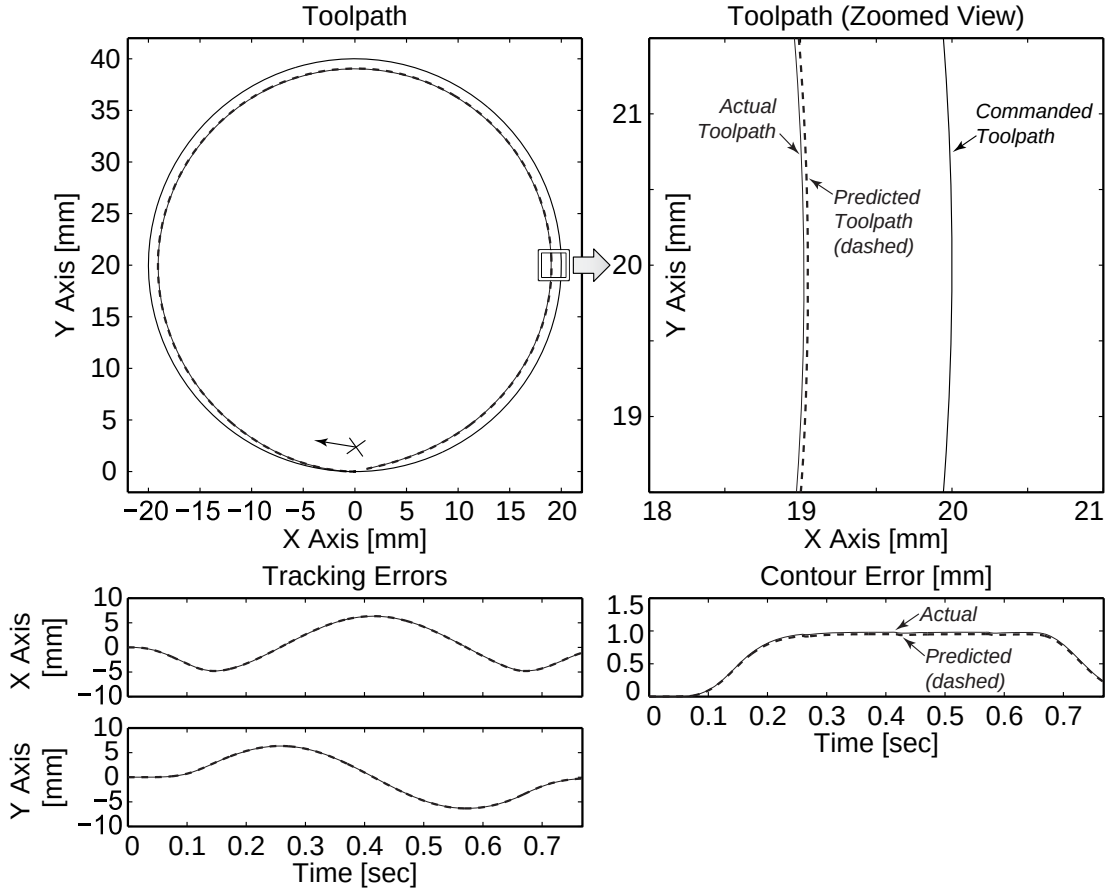

Figure 3.6. Predicted and actual contouring of P-PI controlled servo system (simulation).

In addition, considering the real and estimated disturbance transfer functions (Figure 3.5 (c) and (d)), it can be seen that there is close agreement in the phase shift up to 10 [Hz] and a D.C. amplitude difference of 13.9× for x and 15.7× for y axes, which compensates for the discrepancy between true and estimated friction parameters to a large extent. In overall, it can be said that the estimated transfer functions are successful in capturing the key dynamic characteristics required to predict the tracking and contouring performance of the actual drives with reasonable closeness. The actual and identified axis dynamics have been compared in tracking circular and diamond shaped toolpaths at 200 [mm/sec] feed with 2000 [mm/sec2] trapezoidal acceleration transients. The comparison results are shown in Figure 3.6 and Figure 3.7, which are seen to be in close agreement.

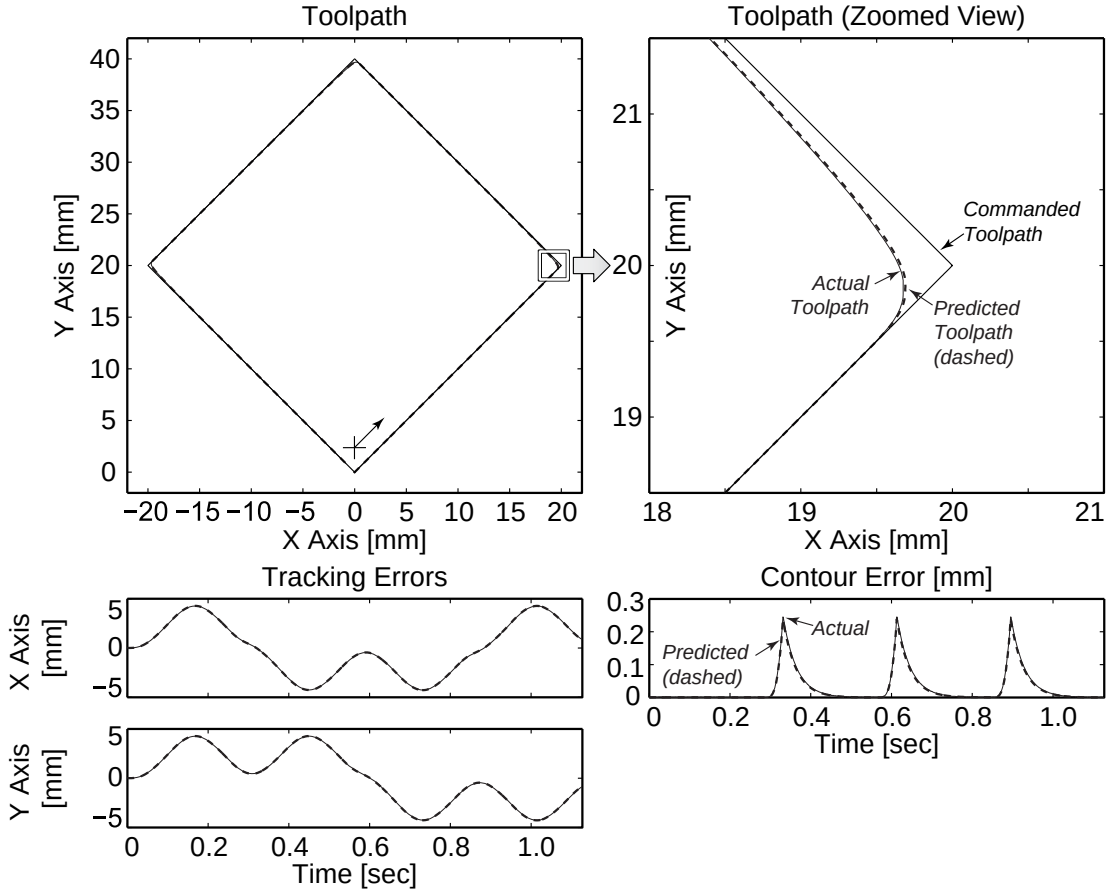

Figure 3.7. Predicted and actual contouring of P-PI controlled servo system (simulation).

PID Controlled System

The second simulation study was conducted for a PID controlled drive system, which does not have an inner velocity control loop. The actual and estimated drive parameters are summarized in Table 3.4.

As seen from the table, there is close match in this case between the actual and identified pole and zero locations. This is verified by the consistency in the actual and estimated frequency response functions (Figure 3.8), both for tracking and disturbance. The tracking transfer functions are in close agreement up to 30 [Hz]. The disturbance transfer functions appear to be in agreement up to 80 [Hz]. When averaged, there is 15 [%] discrepancy between the actual and estimated friction parameters (d_0 and d_1).

Table 3.4. Actual and estimated closed loop parameters for PID controlled drive system.

		X Axis				Y Axis			
		Actual		Estimated		Actual		Estimated	
Parameters	a_1	192.65		214.13		178.75		123.02	
	a_2	44356.23		60040.19		41031.98		40099.88	
	a_3	316830.21		685295.65		293085.57		146558.19	
	b_0	0		-0.35		0		-0.08	
	b_1	190.10		203.86		175.85		123.16	
	b_2	44356.23		60043.78		41031.98		40089.20	
	d_0	441		620		409		478	
	d_1	-302		-280		-388		-428	
Poles and Zeros		Frequency [Hz]	Damping [ ]	Frequency [Hz]	Damping [ ]	Frequency [Hz]	Damping [ ]	Frequency [Hz]	Damping [ ]
Poles	p_1	33.00	0.45	38.21	0.42	31.74	0.43	31.69	0.30
	p_2	33.00	0.45	38.21	0.42	31.74	0.43	31.69	0.30
	p_3	1.17	1.00	1.89	1.00	1.17	1.00	0.59	1.00
Zeros	z_1	–	–	129.50	-1.00	–	–	270.83	-1.00
	z_2	35.96	1.00	32.88	1.00	35.96	1.00	42.98	1.00
	z_3	1.17	1.00	1.89	1.00	1.17	1.00	0.59	1.00

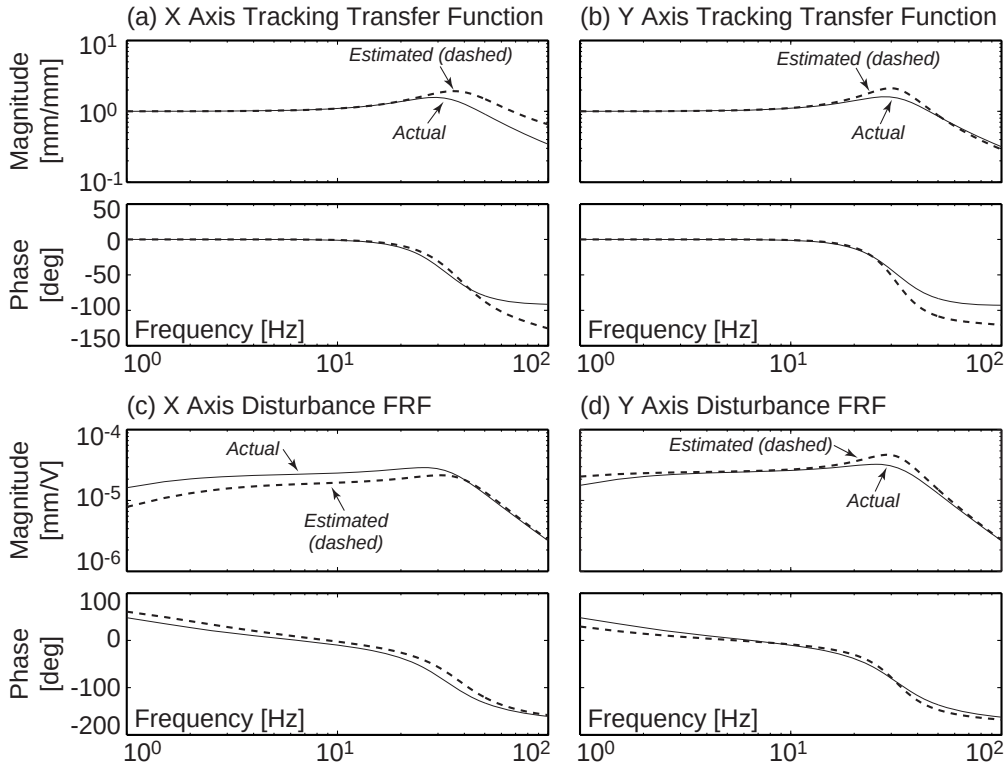

Figure 3.8. Estimated and actual tracking and disturbance frequency response functions (FRF's) for PID controlled servo system (simulation).

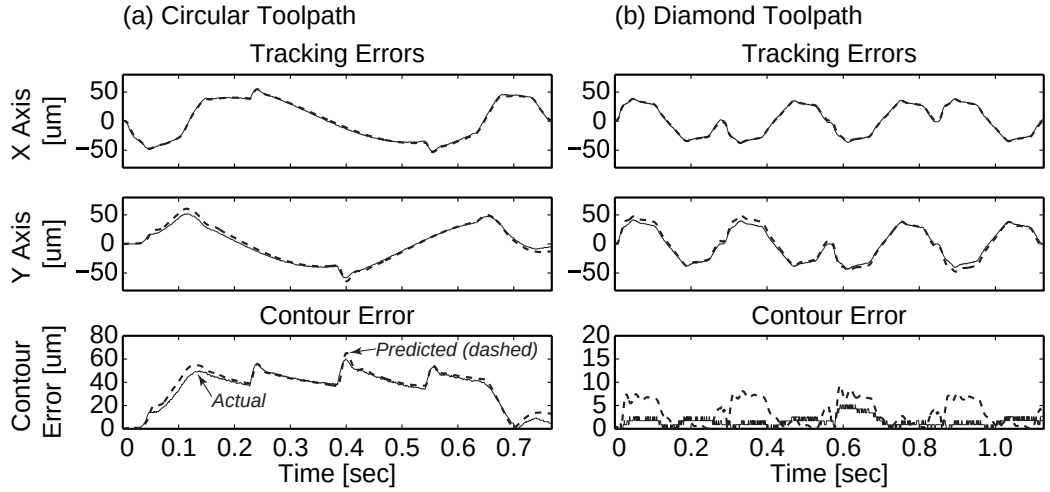

Figure 3.9. Predicted and actual contouring of PID controlled system (simulation).

The circular and diamond contouring results for the actual and estimated transfer functions are shown in Figure 3.9, which are also in close agreement.

Adaptive Sliding Mode Controlled System

The third control structure which was evaluated is adaptive sliding mode control. When adaptation is conducted only for the unknown disturbance, the control law assumes a PID-like structure with feedforward velocity and acceleration terms [13]. The true and estimated drive parameters are summarized in Table 3.5. Due to the existence of feedforward control action, there is full pole-zero cancellation in both axes, resulting in a tracking transfer function equal to unity with zero phase shift in the ideal case. This makes the accurate identification of drive parameters very difficult. It is seen that the identified poles and zeros do not match their true values. However, the near-cancellation effect can be observed between poles at 7.04 and 93.76 [Hz] and zeros at 7.05 and 101.62 [Hz] in the x axis, and poles at 7.86 and 108.50 [Hz] and zeros at 7.87 and 116.02 [Hz] in the y axis, yielding reasonably flat tracking transfer functions up to 50 [Hz] range, as seen in Figure 3.10(a) and (b). There is 5.8× and 5.1× inconsistency between actual and estimated friction model parameters, in x and y axes, which is compensated by the 4.0× and 3.9× D.C. gain difference in the real and estimated disturbance transfer functions (Figure 3.10 (c) and (d)), which are in close phase agreement up to 10 [Hz].

Table 3.5. Actual and estimated closed loop parameters for SMC controlled drive system.

		X Axis				Y Axis			
		Actual		Estimated		Actual		Estimated	
Parameters	a_1	390.10		566.95		493.09		449.09	
	a_2	57029.44		370137.94		87925.67		484496.30	
	a_3	3801962.50		15346572.85		5861711.35		22962987.98	
	b_0	1.00		0.85		1.00		0.87	
	b_1	390.10		574.83		493.09		455.36	
	b_2	57029.44		370142.25		87925.67		484500.13	
	d_0	441		2367		409		2023	
	d_1	-302		-1858		-388		-2016	
Poles and Zeros		Frequency [Hz]	Damping [ ]	Frequency [Hz]	Damping [ ]	Frequency [Hz]	Damping [ ]	Frequency [Hz]	Damping [ ]
Poles	p_1	31.83	1.00	93.76	0.44	31.83	1.00	108.50	0.29
	p_2	21.94	0.69	93.76	0.44	27.25	0.86	108.50	0.29
	p_3	21.94	0.69	7.04	1.00	27.25	0.86	7.86	1.00
Zeros	z_1	31.83	1.00	101.62	0.50	31.83	1.00	116.02	0.32
	z_2	21.94	0.69	101.62	0.50	27.25	0.86	116.02	0.32
	z_3	21.94	0.69	7.05	1.00	27.25	0.86	7.87	1.00

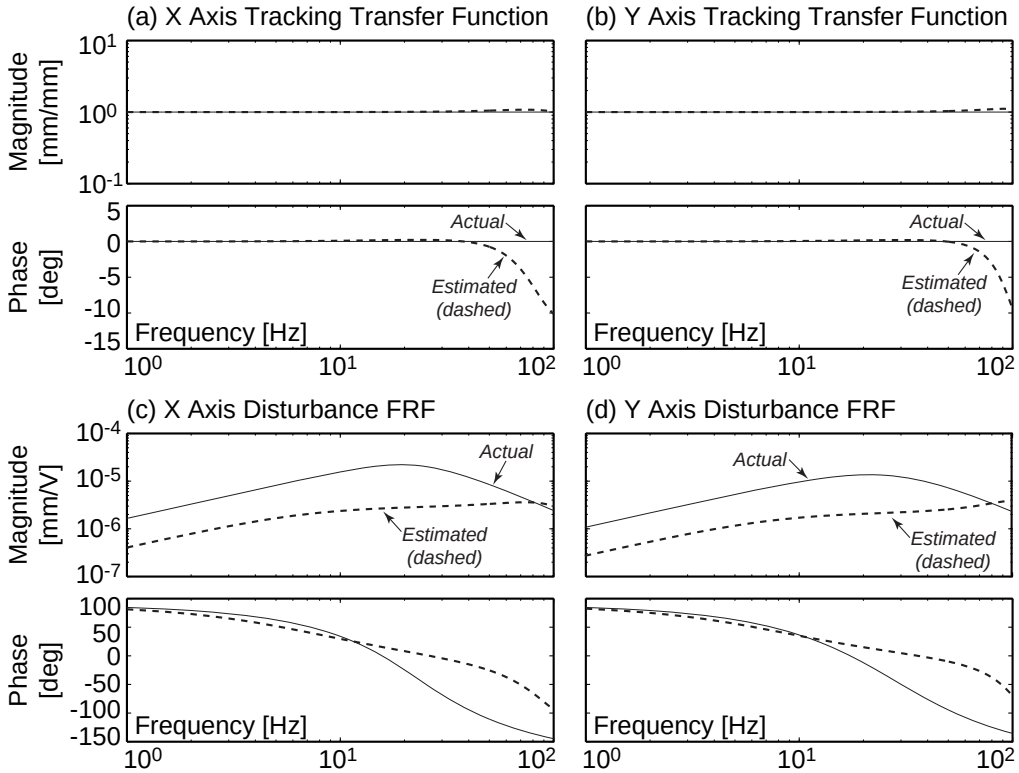

Figure 3.10. Estimated and actual tracking and disturbance frequency response functions (FRF's) for sliding mode controlled servo system (simulation).

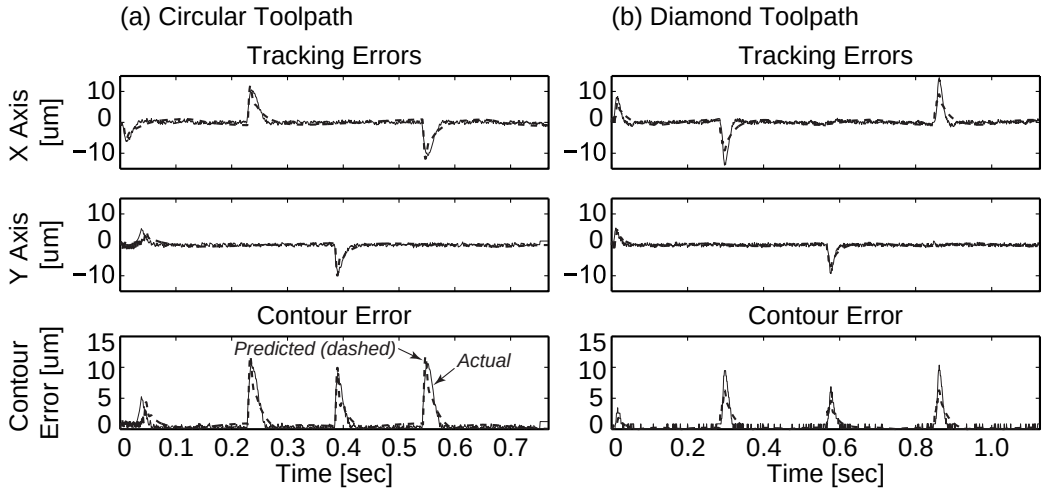

Figure 3.11. Predicted and actual contouring performance of sliding mode controlled servo system (simulation).

The contouring results obtained with the actual and estimated drive models for the two toolpaths are shown in Figure 3.11, which are again in agreement.

The simulation results validate the proof of concept for the proposed rapid identification strategy. They show that theoretically it is possible to construct virtual models of existing feed drives, using data captured during a short G-code experiment. Although the identified models may not exactly have the same parameters as the actual drive system, they are still successful in predicting the tracking and contouring accuracies of CNC machine tools for different part programs.

3.4.2 Experimental Results

Following successful concept validation in simulation results, the rapid identification technique was tested experimentally on a ball screw drive, to demonstrate its practical effectiveness. The ball screw drive setup, controlled with a dSPACE motion controller, is shown in Figure 3.12. Position measurements were obtained from the encoder mounted on the motor, which provides a resolution equivalent to 1.25 [um] of table motion. Due to the availability of only a single drive, the x and y axis trajectories were tested separately and the results were synchronized by overlapping the command trajectories, which enabled the estimation of equivalent contour error profiles.

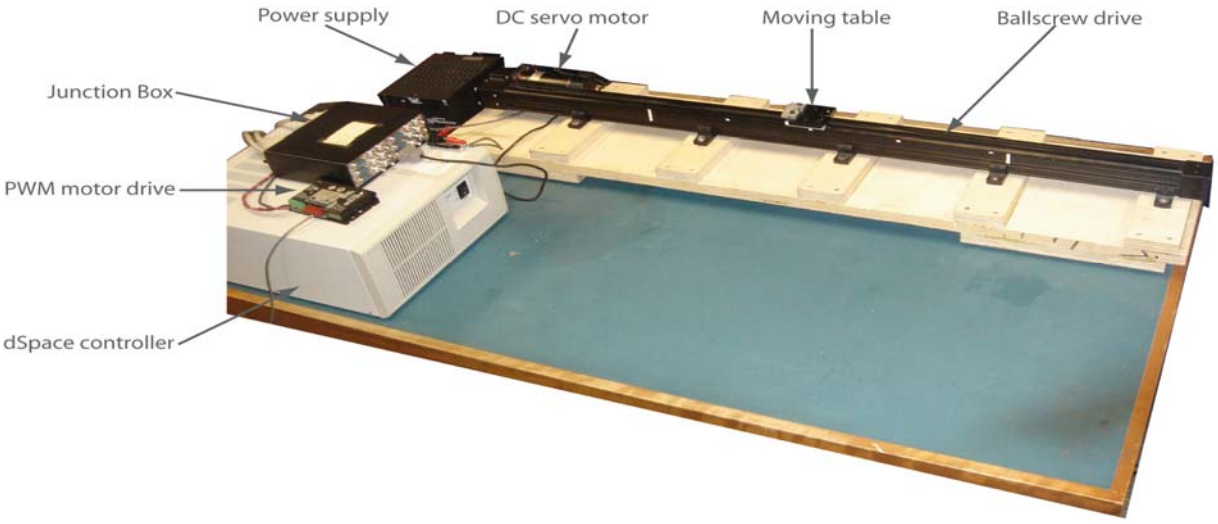

Figure 3.12. Setup of one axis ballscrew system.

Two control cases have been considered: In the first case, the control loop is closed using a Pole Placement Controller (PPC) [11] with a Kalman Filter (KF) [46] for disturbance observation and cancellation. In the second case, a Zero Phase Error Tracking Controller (ZPETC) [14] is added to the scheme, to widen the tracking bandwidth with feedforward control action. The implemented control scheme is shown in Figure 3.13. The ZPETC improves the tracking accuracy by widening the overall command following bandwidth. In order to achieve this, it cancels out all of the poles and stable (or well damped) zeros of the closed loop system achieved with the pole-placement controller. Considering Figure 3.13, the discrete-time transfer function between the filtered position commands $x_r^*(z)$ and the final axis position $x(z)$ can be expressed as,

$$\frac{x(z)}{x_r^*(z)} = G(z) = \frac{B(z)}{A(z)} = \frac{B^+(z)B^-(z)}{A(z)} \tag{3.23}$$

In the numerator, $B^+(z)$ contains all of the stable and well-damped, and $B^-(z)$ contains the unstable or poorly damped zeros. The expression for the ZPETC is given as [14],

$$G_{ZPETC}(z) = \frac{x_r^*(z)}{x_r(z)} = \frac{A(z)B^-(z^{-1})}{B^+(z)[B^-(1)]^2} \tag{3.24}$$

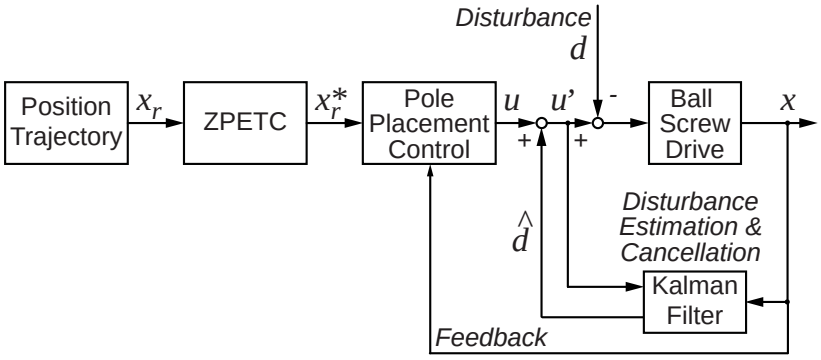

Figure 3.13. ZPETC + PPC + KF control scheme implemented on ball screw drive.

It can be shown that this results in an overall tracking transfer function of

$$\frac{x(z)}{x_r(z)} = G_{ZPETC}(z) \cdot G(z) = \frac{B^-(z) \cdot B^-(z^{-1})}{[B^-(1)]^2} \tag{3.25}$$

which has zero phase shift at all frequencies, and a gain very close to one for a wide frequency range. After conducting the rapid identification, the axis models were verified by running the circular toolpath in Figure 3.6 at 100 [mm/sec] feed with 600 [mm/sec^2] trapezoidal acceleration transients. The actual and predicted tracking and contour error profiles are shown in Figure 3.14, which are in close agreement for both the low bandwidth (PPC + KF) and high bandwidth (PPC + KF + ZPETC) controllers, thus demonstrating the practicality and effectiveness of the proposed identification scheme.

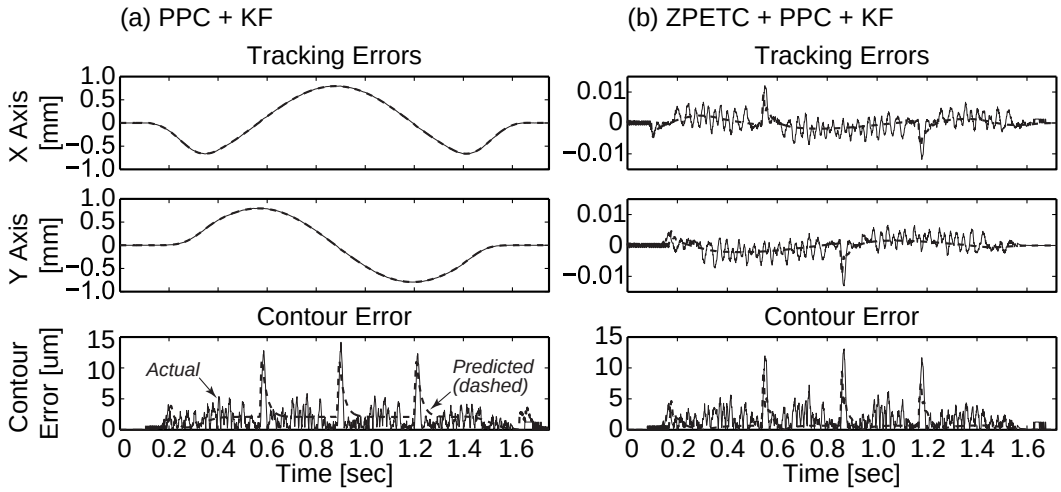

Figure 3.14. Predicted and experimentally verified contouring performance for servo system controlled with (a) pole placement, (b) zero phase error tracking control.

3.5 Conclusions

This chapter has provided a basic mathematical framework for the rapid identification strategy. It has presented a solution which utilizes Lagrange Multipliers for solving the constrained identification problem. This guarantees the stability of identified drive models, regardless of the lack of excitation in the command signals, or presence of pole-zero cancellations in the drive dynamics. The practicality and effectiveness of the proposed identification scheme has been demonstrated in simulation and experimental results, in which the tracking and contouring accuracy of a real drive system could be successfully predicted in a virtual process planning environment. One major downfall of the Lagrange Multipliers technique was found to be its mathematical complexity, which required the use of a dedicated symbolic math solver in order to handle different constraint activation cases. This resulted in a computationally lengthy solution, which sometimes took up to half an hour on a Pentium IV Personal Computer. The dependence on a symbolic solver also limits the portability of the LM solution for industrial implementation. In the next chapter, these issues have been addressed by developing an alternative strategy to solve the constrained identification problem more efficiently, using a Genetic Algorithm.

Chapter 4

Constrained Parameter Estimation using a Genetic Algorithm

4.1 Introduction

In this chapter, a Genetic Algorithm (GA) approach is developed for solving the constrained identification problem defined in earlier Chapter 3. The structure of the GA is explained in detail in Section 4.2. This is followed by simulation and experimental results that validate the practicality and effectiveness of the GA identification scheme. The conclusions are presented in Section 4.4.

4.2 Genetic Algorithm Solution

The structure of the proposed Genetic Algorithm (GA) is shown in Figure 2.7. It is similar to the one proposed by Fogel et al. [33]. The first part of the cycle starts with a Parent Population of solution candidates. This population is used to produce a new generation in the Crossover phase, which inherits its characteristics from the parent pairs. Randomness is introduced by perturbing the new solutions in the Mutation phase. After ensuring compliance with the stability constraints [32], the solution candidates are evaluated for how well they minimize the objective in Eq. (3.12). The best solutions are carried forward to spawn the next generation using the Selection process. This cycle is repeated until the solution pool converges to an optimal set of parameters which best replicate the observed feed drive response. In setting up the GA identification, the solution search is conducted directly in terms of the closed loop pole frequency (ω_n , p) and damping (ζ) values, as shown in Figure 4.1. Adopting this strategy simplifies the incorporation of stability constraints expressed in Eq. (3.8). The upper bounds for pole frequencies ($\omega_{n,\max}$, $p_{\max}$) are set to half of the

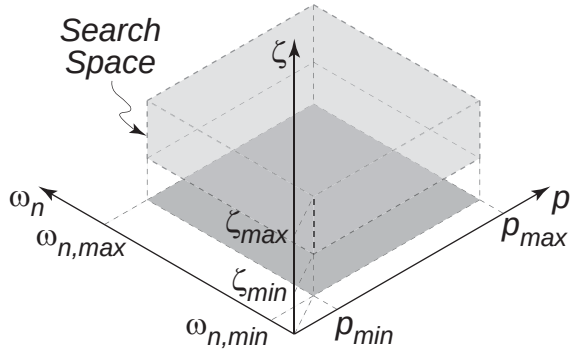

Figure 4.1. Solution search space for GA identification.

sampling frequency (i.e. Nyquist frequency) used in the data collection process. The following notation is adopted in describing the GA identification framework:

$$\mathbf{v}_i^t = \mathbf{v}_i^t(\omega_{n,i}^t, \zeta_i^t, p_i^t) \quad \text{where} \quad \begin{cases} t: \text{Generation Number} \\ i: \text{Candidate Number} \end{cases} \tag{4.1}$$

It should be noted that the GA identification technique can easily be generalized to handle more complex problems with a larger number of parameter constraints. In this case, each constrained parameter would be introduced as an additional bounded variable, resulting in the search space to assume the form of a hyperprism. In the following, phases of the GA identification scheme are explained in detail.

4.2.1 Initial (Parent) Population

The initial population is generated with a uniform distribution within the highlighted search space in Figure 4.1. After the first cycle is complete, the new parent generation is determined through a selection process applied on the mutated solution candidates from the earlier generation.

4.2.2 Crossover Operation

The crossover operation spawns the next generation of candidates by combining pairs from the current generation. It has a smoothening effect on the solution pool, which facilitates convergence. Every solution candidate ($\mathbf{v}_i^t$) is randomly matched with another

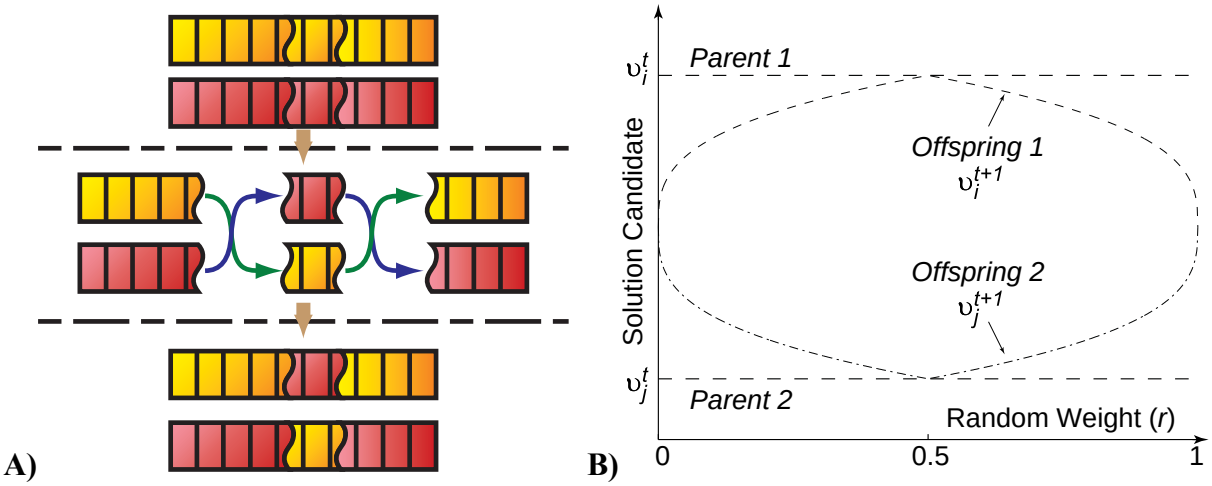

Figure 4.2. Simulated binary crossover (SBX) operation.

candidate ($\mathbf{v}_j^t$). These pairs are then used to produce two new candidates in the next generation: $\mathbf{v}_i^{t+1}$ and $\mathbf{v}_j^{t+1}$. Since the solution candidates are made up of real numbers, the crossover operation needs to be conducted in the domain of real numbers instead of binary. To achieve this, the Simulated Binary Crossover (SBX [47]) operation was adopted with a slight modification which prevents the divergence of the new generation away from the parents. The process of SBX is shown in Figure 4.2. The implemented SBX has the following mathematical expression [47],

$$\mathbf{v}_i^{t+1} = \frac{1+\alpha}{2}\mathbf{v}_i^t + \frac{1-\alpha}{2}\mathbf{v}_j^t \;,\; \mathbf{v}_j^{t+1} = \frac{1-\alpha}{2}\mathbf{v}_i^t + \frac{1+\alpha}{2}\mathbf{v}_j^t$$
$$\text{where}: \alpha = \begin{cases} (2r)^{1/n+1} & , \; r < 0.5 \\ [2(1-r)]^{1/n+1} & , \; r \geq 0.5 \end{cases} \tag{4.2}$$

The specific case use in this thesis is n = 2,

$$\mathbf{v}_i^{t+1} = \frac{1+\alpha}{2}\mathbf{v}_i^t + \frac{1-\alpha}{2}\mathbf{v}_j^t \;,\; \mathbf{v}_j^{t+1} = \frac{1-\alpha}{2}\mathbf{v}_i^t + \frac{1+\alpha}{2}\mathbf{v}_j^t$$
$$\text{where}: \alpha = \begin{cases} (2r)^{1/3} & , \; r < 0.5 \\ [2(1-r)]^{1/3} & , \; r \geq 0.5 \end{cases} \tag{4.3}$$

Above, r is a random weighting factor with a uniform distribution between zero and one, which determines the closeness of the offspring to one of the parents. Possible outcomes of the SBX operation are illustrated in Figure 4.2.

4.2.3 Mutation

Mutation is used to randomly perturb the candidates in the new generation. This helps prevent the Genetic Algorithm from converging to local minima. Each candidate is perturbed in the form:

$$[\mathbf{v}_i^{t+1}]' = \mathbf{v}_i^{t+1} + R_i \eta_i N_i(0,1) \tag{4.4}$$

Above, $N_i(0,1)$ is a random number generated with a normal distribution which has zero mean and unit variance. This variable is computed separately for each candidate. R_i is a scaling factor defined as,

$$R_i = \begin{cases} (\mathbf{v}_i^{t+1} - \mathbf{v}_{\min})/3 & , \quad N_i(0,1) \le 0 \\ (\mathbf{v}_{\max} - \mathbf{v}_i^{t+1})/3 & , \quad N_i(0,1) > 0 \end{cases} \tag{4.5}$$

Considering that 99.73% of the values generated by $N_i(0,1)$ will be in the range of -3 to +3 (i.e. three standard deviations), the scaling factor R_i maps these outcomes such that the perturbed solutions span the search space in Figure 4.1 bounded by the corners points $\mathbf{v}_{\min}(\omega_{\min}, \zeta_{\min}, p_{\min})$ and $\mathbf{v}_{\max}(\omega_{\max}, \zeta_{\max}, p_{\max})$. The η_i term represents a momentum step size, which is employed in evolutionary programming to facilitate larger perturbation in initial cycles. As iterations continue, η_i converges to a stationary random sequence around "1". Its mathematical expression is given as [31],

$$\begin{aligned} &\eta_i = \exp(\tau' N_t(0,1) + \tau N_i(0,1)) \\ &\text{where}: \quad \tau = 1/\sqrt{2\sqrt{t}} \quad , \quad \tau' = 1/\sqrt{2t} \end{aligned} \tag{4.6}$$

Above, $N_t(0,1)$ is generated from a normally distributed random sequence, independently from $N_i(0,1)$. $N_t(0,1)$ is updated only once for each generation. Essentially, $N_i(0,1)$ represents individual mutations which can affect each candidate separately while $N_t(0,1)$ represents an overall mutation affecting the whole generation. τ and τ' ensure that the step size is different for each iteration.

4.2.4 Constraint Checking

Each candidate is checked for compliance with the constraints. If any value of ω_n, ζ, or p is outside the valid search range, it is replaced by the closest bound:

$$\left.\begin{array}{llll} \text{if } [\omega_{n,i}^t]' < \omega_{n.\min} \Rightarrow [\omega_{n,i}^t]' = \omega_{n.\min}, & \text{if } [\omega_{n,i}^t]' > \omega_{n.\max} \Rightarrow [\omega_{n,i}^t]' = \omega_{n.\max} \\ \text{if } [\zeta_i^t]' < \zeta_{\min} \Rightarrow [\zeta_i^t]' = \zeta_{\min}, & \text{if } [\zeta_i^t]' > \zeta_{\max} \Rightarrow [\zeta_i^t]' = \zeta_{\max} \\ \text{if } [p_i^t]' < p_{\min} \Rightarrow [p_i^t]' = p_{\min}, & \text{if } [p_i^t]' > p_{\max} \Rightarrow [p_i^t]' = p_{\max} \end{array}\right\} \quad (4.7)$$

4.2.5 Selection

Selection of successful candidates is carried out using a hybrid approach which combines Top Percent and Random Tournament techniques, as shown in Figure 4.3. Top Percent ensures that solutions which yield the lowest value for the objective in Eq. (3.12) are included in the crossover process. Random Tournament, on the other hand, arbitrarily matches pairs out of the mutated pool and selects the superior candidate out of each pair. This approach may lead to the same candidate being chosen more than once, as seen with $\boldsymbol{\upsilon}'_4$ for example in Figure 4.3.

During implementation of the GA, numerical evaluation of the cost function was found to bring the largest computational load. Naming N as the number of collected data samples, computing the objective function using the form in Eq. (3.12) would require $9N+23$ multiplications, $9N+16$ additions, and 1 division. Typically N is larger than 1000 and in our experimental results $N = 8192$. In order to avoid this computational bottleneck,

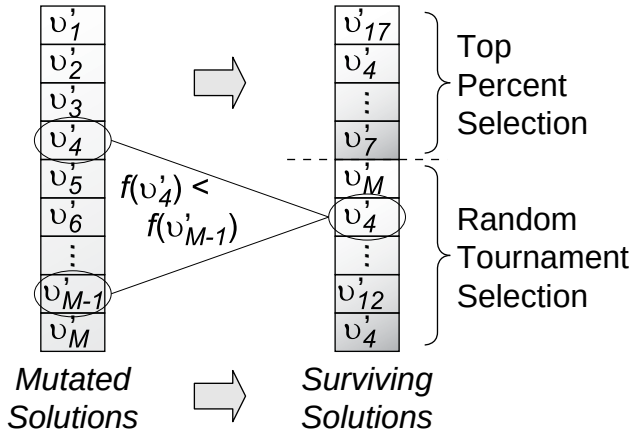

Figure 4.3. Selection of best solution candidates.

calculation of the objective function was realized in a more efficient manner as explained in the following paragraphs.

The parameter vector $\boldsymbol{\theta}$ in Eq. (3.11) can be separated into two parts as:

$$\boldsymbol{\theta} = [\underbrace{\alpha_i \quad \alpha_1 \quad \alpha_2}_{\boldsymbol{\theta}_1^T} \quad \underbrace{\beta_0 \quad \beta_1 \quad \beta_2 \quad \delta^+ \quad \delta^-}_{\boldsymbol{\theta}_2^T}]^T = [\boldsymbol{\theta}_1^T \quad \boldsymbol{\theta}_2^T]^T \tag{4.8}$$

Given the pole frequency and damping values for a particular solution candidate $\boldsymbol{\upsilon}_i^t(\omega_{n,i}^t, \zeta_i^t, p_i^t)$, the normalized denominator parameters $\boldsymbol{\theta}_1 = [\alpha_i \quad \alpha_1 \quad \alpha_2]^T$ can be determined using Eq. (3.14). The remaining parameters $\boldsymbol{\theta}_2 = [\beta_0 \quad \beta_1 \quad \beta_2 \quad \delta^+ \quad \delta^-]^T$ can then be uniquely calculated by constructing a Least Squares sub-problem [45], assuming that the inverse for $\boldsymbol{\Phi}_2{}^T\boldsymbol{\Phi}_2$ exists. Hence,

$$\boldsymbol{\Phi}_2\boldsymbol{\theta}_2 = \mathbf{Y} - \boldsymbol{\Phi}_1\boldsymbol{\theta}_1 \Rightarrow \boldsymbol{\theta}_2 = (\boldsymbol{\Phi}_2{}^T\boldsymbol{\Phi}_2)^{-1}\boldsymbol{\Phi}_2{}^T\left(\mathbf{Y} - \boldsymbol{\Phi}_1\boldsymbol{\theta}_1\right) \tag{4.9}$$

Using this idea, and modifying the notation to represent each solution candidate as $\boldsymbol{\mu}_i^t(\boldsymbol{\upsilon}_i^t)$ where,

$$\boldsymbol{\mu}_i^t(\boldsymbol{\upsilon}_i^t) = [1 \quad \alpha_i \quad \alpha_1 \quad \alpha_2]^T \tag{4.10}$$

the normalized drive parameters can be solved in the form:

$$\left.\begin{aligned} &\boldsymbol{\theta}_i^t = \begin{bmatrix} 0 & \mathbf{I}_3 \\ \mathbf{R}* & -\mathbf{P}* \end{bmatrix} \boldsymbol{\mu}_i^t \text{, where } \mathbf{R}* = \begin{bmatrix} p_{44} & \cdots & p_{48} \\ \vdots & \ddots & \vdots \\ p_{84} & \cdots & p_{88} \end{bmatrix}^{-1} \begin{bmatrix} r_4 \\ \vdots \\ r_8 \end{bmatrix} \\ &\text{and} \quad \mathbf{P}* = \begin{bmatrix} p_{44} & \cdots & p_{48} \\ \vdots & \ddots & \vdots \\ p_{84} & \cdots & p_{88} \end{bmatrix}^{-1} \begin{bmatrix} p_{41} & p_{42} & p_{43} \\ \vdots & \vdots & \vdots \\ p_{81} & p_{82} & p_{83} \end{bmatrix} \end{aligned}\right\} \tag{4.11}$$

It should be noted that the matrix terms p_{ij} and r_k are directly the individual entries of $\mathbf{P}$ and $\mathbf{R}$ matrices defined in Eq. (3.19). The value of the objective function (i.e. fitness) for each candidate can then be evaluated by expanding Eq. (3.12) using Eqs. (4.10) and (4.11), which results in:

$$\left.\begin{aligned} &f(\boldsymbol{\upsilon}_i^t) = \frac{1}{2}([\boldsymbol{\mu}_i^t]^T \mathbf{A}\boldsymbol{\mu}_i^t + \mathbf{B}\boldsymbol{\mu}_i^t + \boldsymbol{\Gamma}) \\ &\text{where} \quad \mathbf{A}_{4\times4} = \begin{bmatrix} 0 & \mathbf{R}*^T \\ \mathbf{I}_3 & -\mathbf{P}*^T \end{bmatrix} \mathbf{P} \begin{bmatrix} 0 & \mathbf{I}_3 \\ \mathbf{R}* & -\mathbf{P}* \end{bmatrix}, \ \mathbf{B}_{4\times1} = -2\mathbf{R}^T \begin{bmatrix} 0 & \mathbf{I}_3 \\ \mathbf{R}* & -\mathbf{P}* \end{bmatrix}, \\ &\boldsymbol{\Gamma}_{1\times1} = \mathbf{Y}^T\mathbf{Y} \end{aligned}\right\} \tag{4.12}$$

Above, matrices $\mathbf{A}$, $\mathbf{B}$, and $\boldsymbol{\Gamma}$ depend solely on the experimental data and are computed only once prior to running the Genetic Algorithm. Given $\boldsymbol{\upsilon}_i^t(\omega_{n,i}^t, \zeta_i^t, p_i^t)$ for a solution candidate, evaluation of the objective function using Eq. (4.12) requires only 32 multiplications, 22 additions and 1 division, hence reducing the computational load by 2-3 orders of magnitude. It should be noted that a similar reduction can also be obtained in more complex problems with a larger number of constrained variables. This step, which improves the numerical efficiency, was crucial in realizing a practically viable Genetic Algorithm for solving the constrained identification problem. This numerical simplification is also one of the contributions in this thesis.

4.3 Simulation and Experimental Results

The Genetic Algorithm identification technique was validated in simulations and experiments conducted on virtual and real feed drive systems. Simulations were conducted on a virtual machine tool model to verify the parameter convergence and servo error prediction capability. Experiments were conducted on a ball screw drive and a 5-axis machining center, to demonstrate the practicality and effectiveness of the GA. Where applicable, the GA has been compared to the LM technique described in Chapter 3.

The GA was configured to have a population size of 4000 candidates in each generation. The parameter search ranges were set as $\omega_{n,\min} = p_{\min} = 0.2$ [Hz], $\omega_{n,\max} = p_{\max} = 500$ or 800 [Hz] (depending on the sampling frequency), $\zeta_{\min} = 0.2$, and $\zeta_{\max} = 2.0$. The crossover rate is 0.5 and the mutation rate is 0.05. The selection operation was carried out by choosing the best 5 solutions (i.e. 0.125%) using the Top Percent approach, and the remaining using the Random Tournament approach, as explained in Section 4.2.5. The GA was implemented in Matlab on a Pentium IV computer. The implementation did not require the use of any specialized toolboxes and was written in a manner that could be directly ported into C++ or any other programming language. The Lagrange Multipliers solution was also implemented in Matlab on the same PC platform, but required the use of the Symbolic Math Toolbox, as mentioned in Chapter 2, to handle cases where the unconstrained solution of Eq. (3.12) violated the parameter bounds in Eq. (3.8).

The LM solution represents the best theoretical estimate that could be obtained with the collected data and given parameter constraints. When all constraint activation cases need to be checked, the solution takes around 15-20 minutes to compute. On the other hand, the Genetic Algorithm was observed to converge within 2-3% closeness of the LM solution in about 2-3 minutes, making the GA a more practical alternative to the LM approach, even if it is slightly less exact. Sample results are presented in the following.

4.3.1 Validation on a Virtual Machine Tool

In the first example, the Genetic Algorithm is compared to the Lagrange Multipliers (LM) solution in simulation results obtained using the virtual machine tool model (Fadal VMC 2216) reported in Section 3.4.1. The drive's axes were controlled using PID controllers tuned to provide a bandwidth of 57 [Hz]. The rapid identification data generated by running the G-code in Table 3.2 was used.

The identification results obtained with the two schemes are shown in Figure 4.4 and Table 4.1. Figure 4.4 shows the convergence of GA parameter estimates to the LM solution. Table 4.1 presents the actual and estimated values of the search variables, model parameters, and tracking transfer function zeros. Considering Figure 4.4, it can be seen that in about 300 iterations, the Genetic Algorithm converges closely to the LM solution. The actual solutions are captured at 500 iterations with a repeatability rate of 100%. All the test cases result are documented in Appendix A.

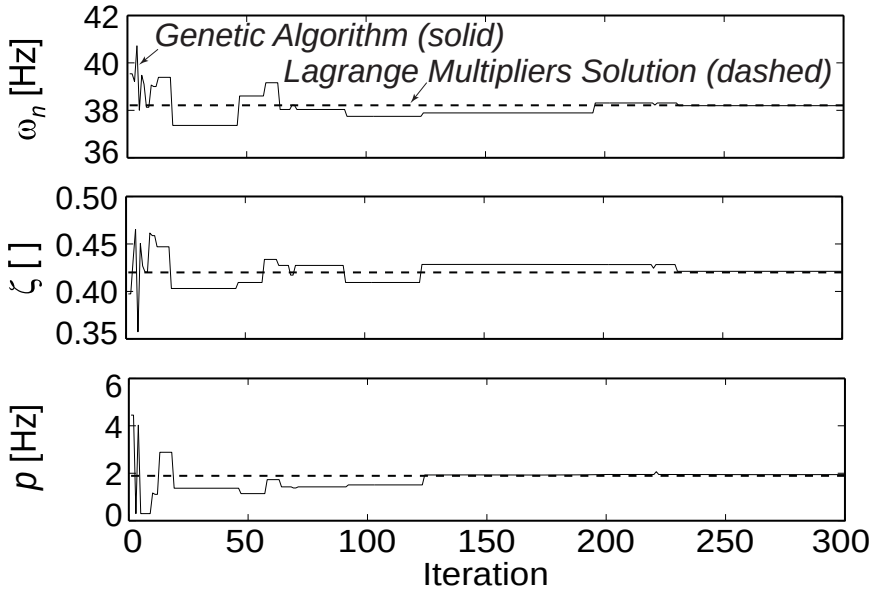

Figure 4.4. Estimated parameters for PID controlled virtual drive.

Table 4.1. Actual and estimated parameters for PID controlled virtual drive.

Search variables	Actual	Lagrange Multipliers Estimate	Genetic Algorithm Estimate
ω_n [Hz]	*33*	***38.21***	***38.20***
ζ [ ]	*0.45*	***0.42***	***0.42***
p [Hz]	*1.17*	*1.89*	*1.94*
Model Parameters	Actual	Lagrange Multipliers Estimate	Genetic Algorithm Estimate
a_1	192.65	214.13	214.41
a_2	44356.23	60040.19	60072.73
a_3	316830.21	685295.65	703594.29
b_0	0	-0.35	-0.34
b_1	190.1	203.86	203.74
b_2	44356.23	60043.78	60076.41
d_0	441	620	627
d_1	-302	-280	-277
Zero Locations	Actual	Lagrange Multipliers Estimate	Genetic Algorithm Estimate
z_1 [Hz]	-35.96	127.32	129.58
z_2 [Hz]	*-1.17*	-32.72	-32.87
z_3 [Hz]	-	*-1.89*	*-1.95*

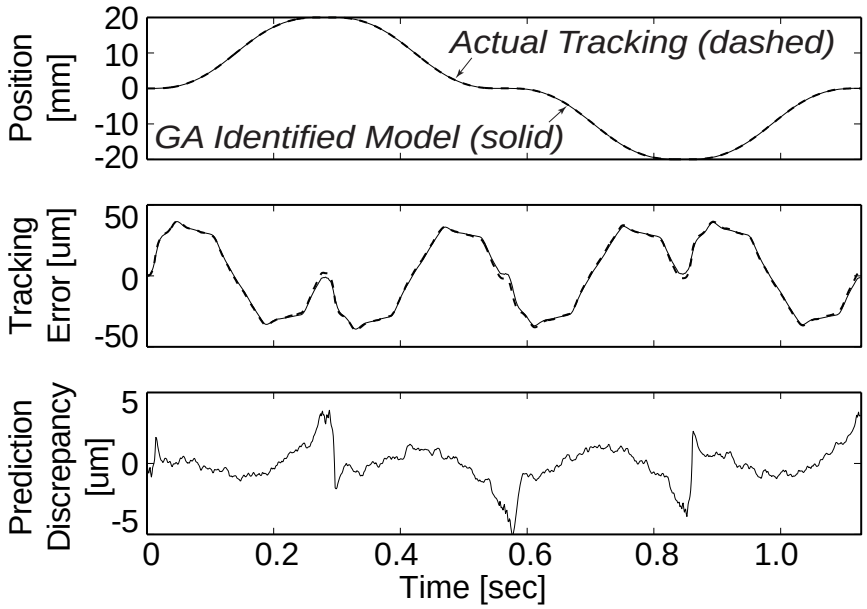

Figure 4.5. Predicted and actual tracking performance of virtual feed drive (simulation).

As shown in Table 4.1, the natural frequency and damping ratio are estimated in a consistent manner between both solutions ($\omega_{n,LM}$ =38.21, $\omega_{n,GA}$ =38.20 [Hz] and $\zeta_{LM} = \zeta_{GA}$=0.42), and the estimates are reasonably close to their true values ($\omega_{n,Actual}$ =33 [Hz], ζ_{Actual} =0.45). The estimates for the real pole are also consistent among each other (p_{LM} =1.89, p_{GA} =1.94 [Hz]), but slightly different from the actual pole location (p_{Actual} =1.17 [Hz]). Considering that the real pole is cancelled by a zero in all cases ($z_{2,Actual} = -1.17$, $z_{3,LM} = -1.89$, $z_{3,GA} = -1.95$ [Hz]), this pole does not have any effect on the command following properties but it influences the response of axis position to disturbances, as can be inferred from the block diagram in Figure 3.1. The GA identified model was validated in a tracking simulation using a trajectory of ±20 [mm] of forward and backward motion commanded at a feedrate of 70.71 [mm/sec] with acceleration transients of 424.26 [mm/sec^2]. The simulation result is shown in Figure 4.5, in which the tracking error, using the reference trajectory, predicted with the GA identified model is generally within 10-15% closeness of the actual tracking error.

4.3.2 Validation on a Ball Screw Drive

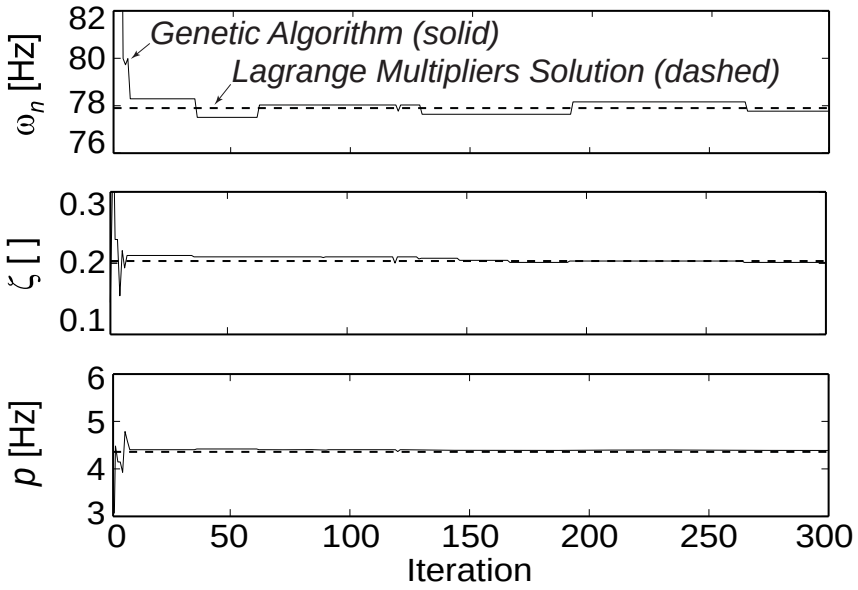

Figure 4.6. Estimated parameters for ZPETC + PPC + KF controlled ball screw drive (experimental).

In the second example, the GA is tested on the ball screw drive controlled with the ZPETC + PPC + KF scheme, explained in Section 3.4.2. As mentioned earlier, in this control configuration accurate identification of the closed loop dynamics is very difficult, due to the pole-zero cancellations that take place between the feedback loop and the ZPETC. The parameter convergence obtained using experimental identification data is shown in Figure 4.6. As can be seen, the GA estimates converge closely to the LM solution in less than 50 iterations. The actual discrete-time controller design parameters and model estimates obtained with GA and LM techniques are shown in Table 4.2. The control system was designed at a sampling period of T_s = 1 [msec] and the closed loop poles were placed at $p_{1,2}$ =0.86846+j0.11762 in the z-domain, corresponding to a natural frequency of $\omega_{n,Actual}$ =30 [Hz] and a damping ratio of ζ_{Actual} =0.7. These poles are cancelled out by the zeros of the ZPETC at $z_{3,4}$ =0.86846+j0.11762, and replaced by two deadbeat delay terms $p_{3,4}$ =0. The closed loop zero at z_1 =-0.99937, which is very close to -1, is not directly cancelled out but its phase lag is removed by incorporating another zero at z_2 = –1.0006

Table 4.2. Actual and estimated parameters for ZPETC + PPC + KF controlled ball screw drive.

Actual Parameters (discrete-time system)	**Search Variables**	Lagrange Multipliers Estimate	Genetic Algorithm Estimate
Sampling Period	ω_n [Hz]	***77.83***	***77.30***
T_s = 0.001 [sec]	ζ [ ]	***0.203***	***0.202***
PPC + KF (closed loop)	p [Hz]	*4.36*	*4.39*
Poles	**Model Parameters**	Lagrange Multipliers Estimate	Genetic Algorithm Estimate
$p_{1,2}$=0.86846+j0.11762 (ω_n=30 [Hz], ζ=0.7)			
Zeros z_1=-0.99937	a_1	225.94	223.76
ZPETC (feedforward filter)	a_2	244579.87	241310.90
Poles	a_3	6551189.40	6510957.51
$p_{3,4,5}$ = 0 (*3 delays*)	b_0	0.75	0.76
Zeros	b_1	240.24	238.13
z_2 = -1.0006	b_2	244452.20	241460.26
$z_{3,4}$ = 0.86846 + j0.11762	d_0	1032.57	1024.55
Overall Transfer Function	d_1	-996.03	-987.61
Poles	**Zero Locations**	Lagrange Multipliers Estimate	Genetic Algorithm Estimate
$p'_{1,2,3}$ = 0 (*3 delays*)	z_1 [Hz]	*-4.37*	*-4.39*
Zeros	$z_{2,3}$	ω=89.76 [Hz], ζ=0.26	ω=88.65 [Hz], ζ=0.26
$z'_{1,2}$ = -1.0006, -0.99937			

through spectral factorization (i.e. 1/–0.99937= –1.0006) and adding an additional delay term p_5=0 to make the ZPETC causal.

It was shown in [48] that additional closed loop poles contributed by the Kalman filter do not affect the tracking transfer function, as they get cancelled out by collocated zeros. Hence, their effect is ignored, which simplifies the ZPETC design and analysis. During parameter identification and model validation the command trajectory was shifted forward in time by 2 samples, which is the preview horizon of the designed ZPETC [14]. One shift accounts for the pole excess and the other for the number of unstable zeros, in the closed loop system.

Considering the LM and GA estimates, it is seen that the natural frequency, damping ratio, and real poles are estimated consistently between the two techniques: $\omega_{n,LM}$ =77.83, $\omega_{n,GA}$ =77.30, p_{LM} =4.36, p_{GA} =4.39 [Hz], ζ_{LM} =0.203, ζ_{GA} =0.202. The identified natural frequency and damping ratio, however, are very different from their actual closed loop values of $\omega_{n,Actual}$ =30 [Hz] and ζ_{Actual} =0.7. Furthermore, the damping estimate is very close to its minimum acceptable limit $\zeta_{\min}$ =0.2. The identified zero locations are also close to the pole estimates $z_{1,LM}$ = −4.37, $z_{1,GA}$ = −4.39, $\omega_{z_{2,3},LM}$ =89.76, $\omega_{z_{2,3},GA}$ =88.65 [Hz], $\zeta_{z_{2,3},LM}$ =0.26, $\zeta_{z_{2,3},GA}$ =0.26, thus emulating the effect of "cancelled dynamics" observed in the real system.

In this example, the dominant closed loop poles were estimated at significantly different locations than their actual values, which resulted in the identified model to have marginal stability characteristics. The non-convergence of parameters was caused by the cancellation of closed loop dynamics with a feedforward filter, which resulted in a loss of identifiability. In other cases involving different control structures or identification signals, parameter convergence can also be hampered by the lack of excitation in smoothly interpolated motion commands. In either case there is no guarantee over the locations at which the closed loop poles will be estimated unless bounds are imposed, as done here, to ensure the stability of identified virtual drive models.

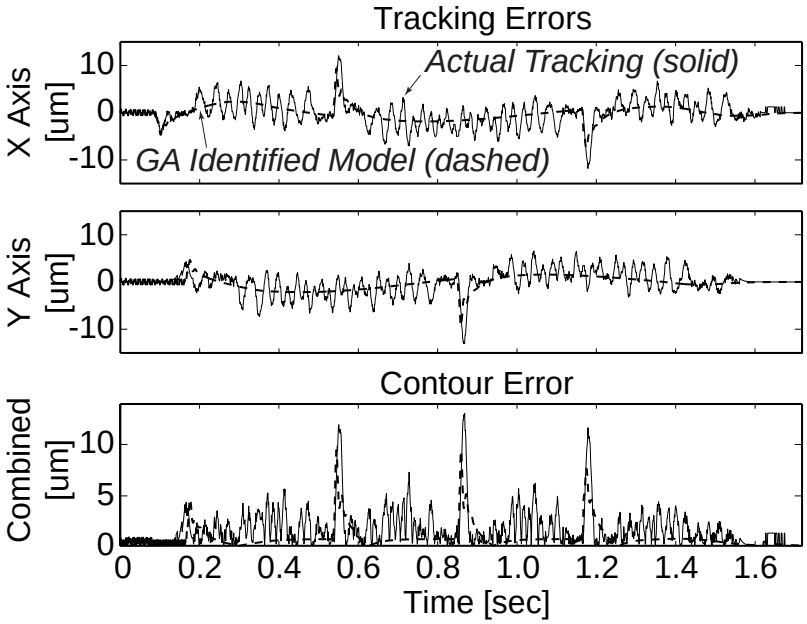

Figure 4.7. Predicted and experimentally verified contouring performance of ball screw drive.

The prediction accuracies of the estimated models were verified in tracking and contouring experiments. The drive's position measurements were obtained from the encoder mounted on the motor, which provided a resolution equivalent to 1.25 [um] of linear table motion. Due to the availability of only a single drive, the x and y axis trajectories were tested separately and the results were synchronized by overlapping the command trajectories. This enabled the equivalent contour error profiles to be estimated. It was seen that the identified models were quite successful in predicting the tracking quality of the actual drive, even during velocity reversals. Predictions obtained with the LM model were presented in 3.4.2 and will not be repeated here. The GA identified model, being very close to the LM solution, displayed a similar performance. A sample result for contouring a 40 [mm] diameter circular toolpath at 200 [mm/sec] feed is shown in Figure 4.7. As can be seen, the GA identified model is reasonably successful in predicting the experimental tracking and contouring accuracy, in spite of the reported mismatch between the true and estimated parameters. This is due to the identified model displaying similar dynamic characteristics to the real drive system in the frequency range of the motion commands, as discussed earlier.

4.3.3 Validation on a Machining Center

In the third example, the practicality and effectiveness of the GA identification scheme is demonstrated with experimental results obtained on a commercial machine tool. A Deckel Maho 80P hi-dyn 5-axis machining center was used in the experiments [49]. The x and y axis dynamics were identified, which enabled a comparison between the actual and predicted contouring performance. The same identification procedure can also be applied for the z (vertical), A (tilt), and C (rotary) axes. The machining center is controlled with a Heidenhain TNC 430M controller which has a built-in oscilloscope feature that allows the commanded and measured axis position data to be captured during the machine's operation [50]. The data capture window is 4096 samples over a period of 2.4576 [sec], corresponding to a sampling period of 0.6 [msec]. The feedback is obtained through linear encoders which provide a measurement resolution of 0.1 [um]. The experiments took only a couple of minutes to perform and no hardware or software modification was required to the machine.

The identification was conducted by running two sets of G-code files; the first one which caused the machine's drives to move at very slow speeds by commanding short travel distances up to 30 [um], and the second one which generated high speed movements by commanding relatively larger travel distances up to 10 [mm]. The maximum feedrate was set to 250 [mm/sec]. This allowed the drives' response to be observed for a wide range of feeds that span the machine's operating envelope, including very slow movements which are encountered during motion reversals. The G-codes used in identifying the x axis are shown in Table 4.3 and Table 4.4 Measurements collected from the two experiments were concatenated into a single data vector, which was processed by the Genetic Algorithm. The position and velocity profiles for the collected data from the x axis are shown in Figure 4.8. Identification of the y axis follows an identical procedure. The identified parameters are summarized in Table 4.5. As can be seen, the x and y axes have well matched natural frequency values ($\omega_{n,x} = \omega_{n,y} = 13.14$ [Hz]), which is essential for minimizing the contouring

Table 4.3. G-code used for generating low speed movements.

```
0 BEGIN PGM RAPIDIDENT MM
;Rapid Identification on TNC 430 5 axis machine
1 BLK FORM 0.1 Z X-50.000 Y-50.000 Z-50.000
2 BLK FORM 0.2 X+50.000 Y+50.000 Z+50.000
3 TOOL CALL 0 Z
4 L Z+200.000 F MAX
5 L X+0.000 Y+0.000 R0 F MAX M3
7 L X-0.000 F 15000.000
```

8 L X+0.000				
9 L X-0.002	14 L X-0.001	...	...	204 L X+0.028
10 L X-0.002	15 L X-0.008	...	200 L +0.009	205 L X+0.000
11 L X-0.004	16 L X+0.002	...	201 L +0.007	206 M30
12 L X-0.001	17 L X-0.012	...	202 L X-.001	207 END PGM
13 L X-0.006	...	...	203 L +0.012	RAPIDIDENT MM

Table 4.4. G-code used for generating high speed movements.

```
0 BEGIN PGM RAPIDIDENT MM
;Rapid Identification on TNC 430 5 axis machine
1 BLK FORM 0.1 Z X-50.000 Y-50.000 Z-50.000
2 BLK FORM 0.2 X+50.000 Y+50.000 Z+50.000
3 TOOL CALL 0 Z
4 L Z+200.000 F MAX
5 L X+0.000 Y+0.000 R0 F MAX M3
6 L Z+0.000 F MAX
7 L X-9.375 F 15000.000
```

8 L X+9.375				
9 L X-5.280	14 L X+0.482	...	...	105 L X+9.375
10 L X-5.552	15 L X+0.117	...	101 L X-.158	106 L X+0.000
11 L X+0.158	16 L X-1.579	...	102 L +5.552	107 M30
12 L X+6.539	17 L X+3.552	...	103 L +5.280	108 END PGM
13 L X-1.538	...	...	104 L X-.375	RAPIDIDENT MM

errors during linear and circular tool movements. The damping ratios are reasonably close as well ζ_x=1.14, ζ_y=1.09.

Estimation of the *3*rd real pole at high frequencies (p_x=439.27, p_y=612.75 [Hz]) indicates the dominance of *2*nd order dynamics.

The identified virtual drive models were validated in contouring experiments conducted on the same machine. Diamond and circular toolpaths were used, as shown in Figure 4.9 and Figure 4.10. The contouring experiments were conducted at a feedrate of 200 [mm/sec]. The command trajectory captured from the machine's interpolator was passed through the virtual drive models to predict the tracking and contouring errors for the toolpaths. The virtual predictions have been overlaid on top of the experimental measurements in the figures. As

can be seen, the drive models are quite successful in predicting the actual tracking and contouring errors during linear movements, circular arcs, as well as sharp corners, thus validating the effectiveness of the proposed GA identification technique.

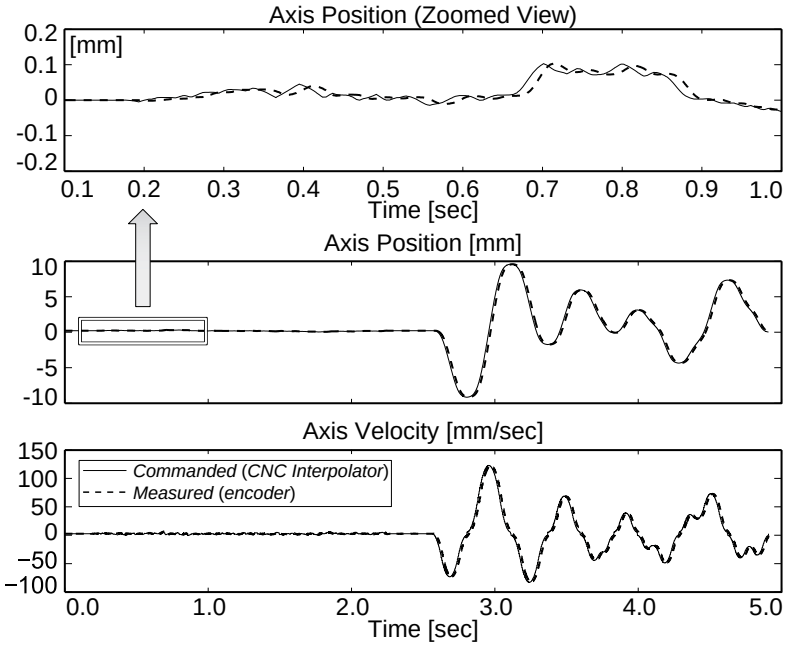

Figure 4.8. Experimentally collected identification data from Heidenhain TNC 430 controller.

Table 4.5. Estimated virtual drive parameters for Deckel Maho 80P hi-dyn machining center.

Search Variables	**X Axis**	**Y Axis**
ω_n [Hz]	***13.14***	***13.14***
ζ [ ]	***1.14***	***1.09***
p [Hz]	439.27	612.75
Model Parameters	**X Axis**	**Y Axis**
a_1	2948.25	4030.00
a_2	526359.32	699755.18
a_3	18813165.66	26243010.58
b_0	0.83	0.82
b_1	-2027	-2540.3
b_2	289780	370630
d_0	4443.5	1801
d_1	832.84	-2711.6
Zero Locations	**X Axis**	**Y Axis**
z_1 [Hz]	363.67	468.00
z_2 [Hz]	32.69	33.33
z_3 [Hz]	-7.69	-8.27

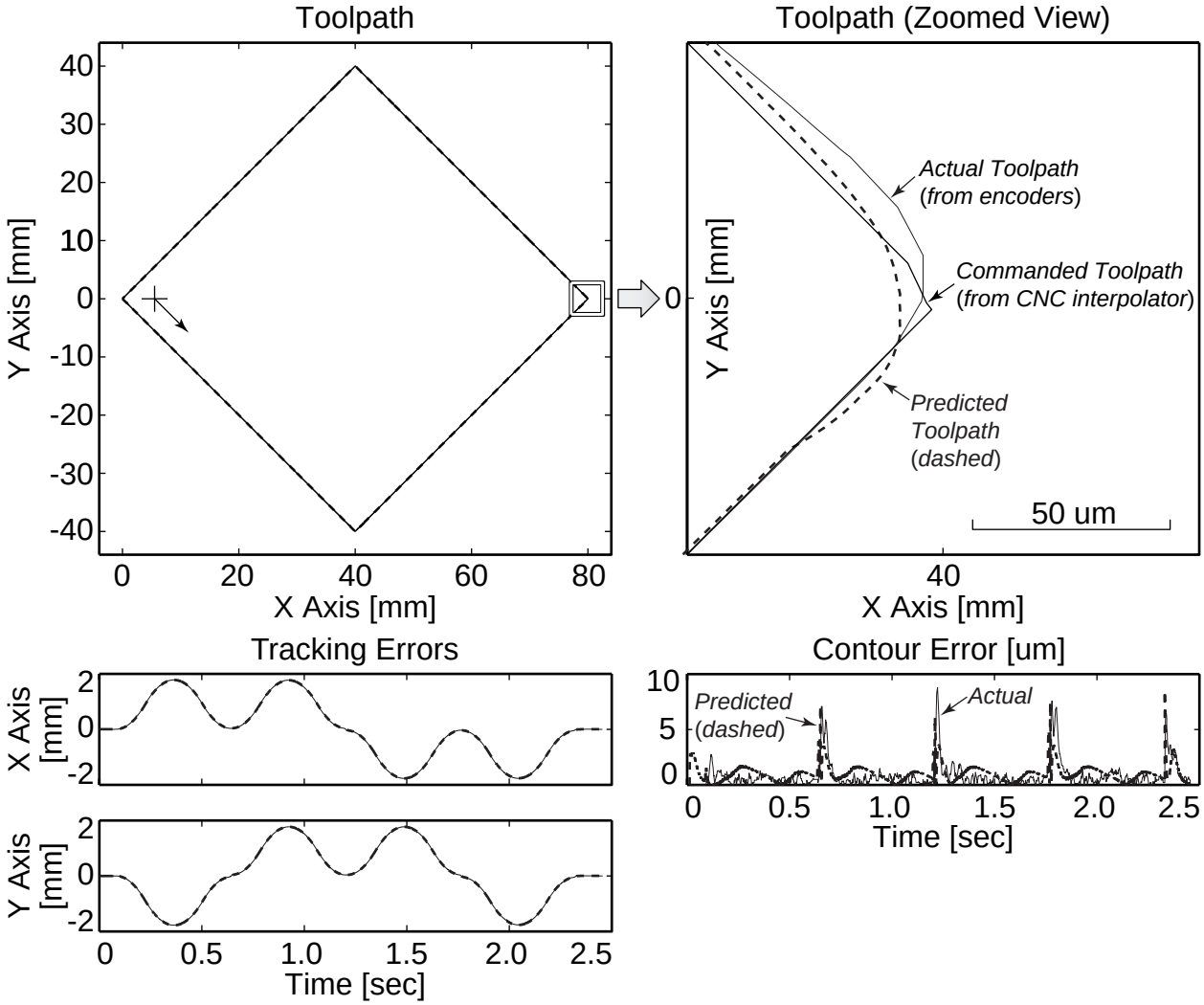

Figure 4.9. Predicted and experimentally verified contouring performance of machining center for a diamond toolpath (feedrate: 200 [mm/sec]).

4.4 Conclusions

This chapter has presented a Genetic Algorithm (GA) for solving the constrained parameter identification problem. The problem formulation has been cast to exploit the GA's inherent ability to constrain the search space, which ensures the stability of identified drive models. Evaluation of the cost function has been streamlined by separating all a priori calculations from the terms that are dependent on individual solution candidates. The proposed methodology can also be extended to handle more complex identification problems

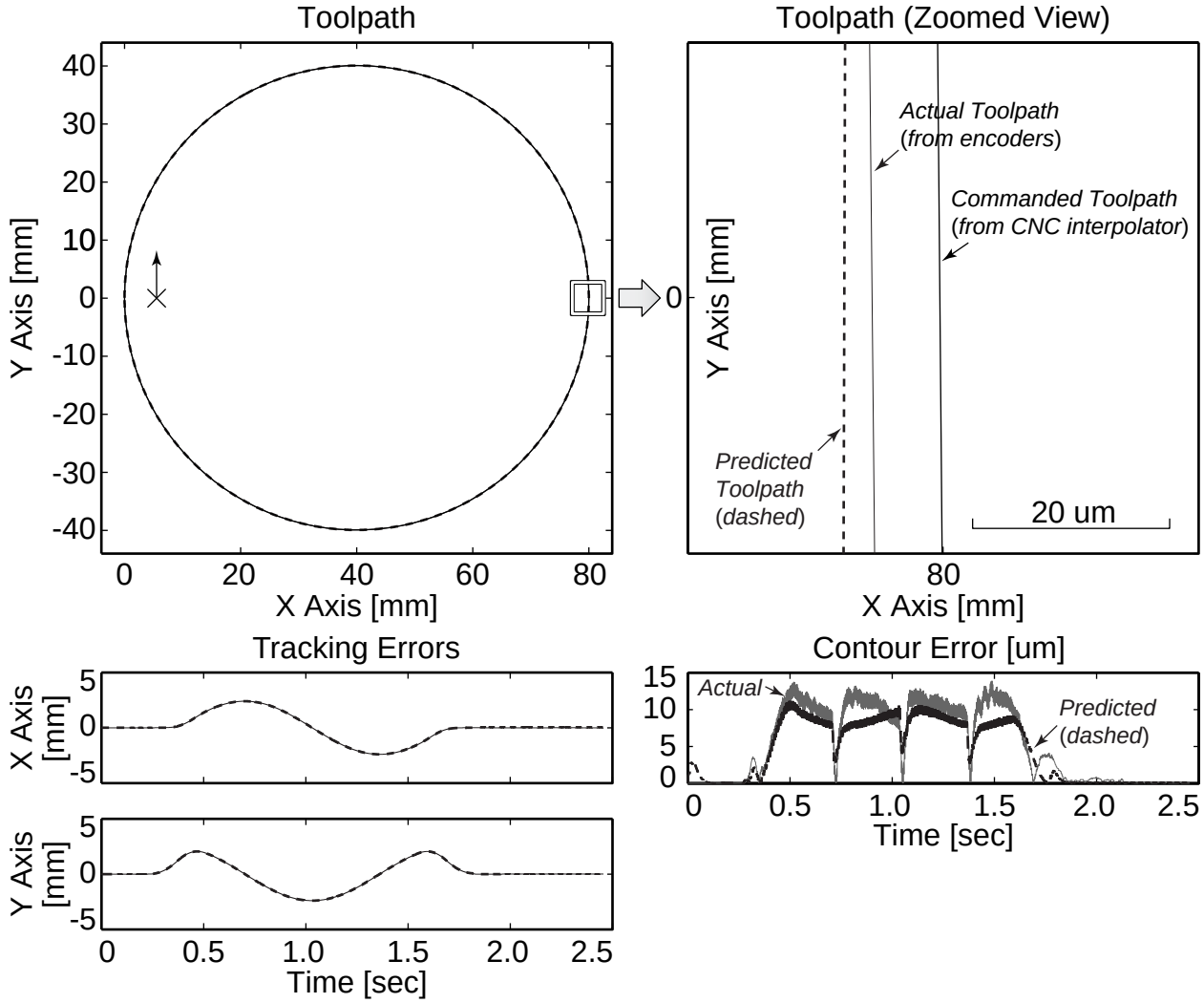

Figure 4.10. Predicted and experimentally verified contouring performance of machining center for a circular toolpath (feedrate: 200 [mm/sec]).

with a larger number of constrained variables. The practicality and effectiveness of the GA identification scheme has been verified in simulations and experiments conducted on virtual and real machine tools. It is shown that the GA can be used for estimating stable models of existing machine tool drives in a practical and efficient manner, it is easy to implement on different computing platforms, and drive models identified with the GA can be employed in predicting the contouring accuracy of real machine tools in a virtual process planning environment.

Chapter 5

Conclusions

This thesis has presented a rapid identification strategy for constructing virtual models of existing CNC drive systems with minimal intervention to the production machinery. The proposed technique consists of executing a short G-code experiment and collecting input and output data using the motion capture feature available on most CNC systems. The collected data is then processed with the intention of reverse engineering the equivalent tracking and disturbance transfer functions of the closed loop drive system, and also the effect of guideway Coulomb friction. It is shown that a virtual drive model constructed this way enables accurate prediction of the real machine's contouring accuracy for large class of feed drive systems controlled with different control techniques.

The excitation input is delivered through motion commands interpolated by the trajectory generator. Since the motion commands are smooth, they lack the persistence of excitation to allow all model parameters to be estimated accurately. Furthermore, if the real servo system contains pole-zero cancellations, which typically occur when feedforward control action is used, this also results in incorrect estimation of the closed loop dynamics. The non-convergence problem brings the risk of identifying critically stable or even unstable virtual drive models, which have limited or no practical value. To address this issue, the rapid identification task has been cast as a constrained minimization problem in which frequency and damping ratio bounds are imposed on the closed loop pole locations.

Two solution strategies have been developed. In the first approach, Lagrange Multipliers (LM) technique is used, which yields successful estimation results. However, implementation of LM is computationally intensive and requires the use of a dedicated symbolic solver for handling the constraint activation scenarios that need to be considered when the

unconstrained solution is computed to be infeasible. These factors significantly limit the portability and practicality of the LM technique for industrial implementation.

In the second approach, a Genetic Algorithm (GA) search technique has been developed, which is a more practical but slightly approximate alternative. The GA's ability to constrain the search space allows parameter bounds to be incorporated in a natural manner. The computation of the GA has been streamlined by decoupling all a priori calculations from the terms that need to be recomputed for each solution candidate. This results in 2-3 orders of magnitude reduction in the computational load, compared to using the objective function in its original form for evaluating the fitness of each candidate. It is shown that the GA converges within 2-3% vicinity of the LM solution in one-tenth of the computation time, and can be easily ported to different platforms for industrial implementation.

Both LM and GA identification techniques have been validated in simulations and experiments conducted on virtual and real machine tool drives. It is shown that although the parameters estimated with the rapid identification scheme do not always match their true values, the key tracking and disturbance rejection characteristics of the drives are successfully captured in the frequency range of the CNC motion commands. Therefore, the drive models constructed with rapid identification can be used to predict the contouring accuracy of real machine tools in a virtual process planning environment.

Due to the time limitation, the actual convergence of the system has not been studied and it should be investigated further, in order to determine the maximum number of iteration cycles for the genetic algorithm. Furthermore, the NC trajectories used in this thesis are based on trial and error, more tests should be conducted in order to obtain the most optimal trajectory. Finally, volumetric error modeling can be incorporated to achieve better prediction of the machine's final contouring accuracy.

Chapter 6

References

[1] Ehmann K.F., DeVor R.E., DeMeter E.C., Dornfeld D., Kapoor S., Ni J., Rajurkar K., Shin Y., Sutherland J., 1997, "A Framework for a Virtual Machine Tool (VMT)." *Technical Papers of NAMRI/SME*, pp. 143-148.

[2] Altintas Y., Brecher C., Weck M., Witt S., 2005, "Virtual Machine Tool," *Annals of CIRP*, Vol. 54, No. 2, pp. 651-673.

[3] Erkorkmaz K., Altintas Y., Yeung C.-H., 2006, "Virtual Computer Numerical Control System," *Annals of CIRP*, Vol. 55, pp. 399-402.

[4] Kuhn H.W., Tucker A.W., 1951, "Nonlinear Programming," *Proceedings of the Second Berkeley Symposium on Mathematical Statistics and Probability*, pp. 481-492.

[5] Schaffers E., 2006, "Advanced 5 Axis Simultaneous Machining with Sinumerik 840D," *Proc. CIRP 2nd Intl. Conf. on High Performance Cutting (HPC'06)*, Vancouver, BC, June 12-13.

[6] Mori M., Fujishima M., 2006, "Innovative Machining Process for Complex Parts using Newly Developed Integrated Mill Turn Center," *Proc. CIRP 2nd Intl. Conf. on High Performance Cutting (HPC'06)*, Vancouver, BC, June 12-13.

[7] Waller A.P., Ladbrook J., 2002, "Experiencing Virtual Factories of the Future," *Proceedings of the Winter Simulation Conference*, Vol. 1 pp.513-517.

[8] Yeung C.-H., Altintas Y., Erkorkmaz K., 2006, "Virtual CNC System - Part I: System Architecture," *International Journal of Machine Tools and Manufacture*, Vol. 46, No. 10, pp. 1107-1123.

[9] Chang T.-C., Wysk R.A., Wang H.-P., *Computer-Aided Manufacturing 2nd Edition*, Prentice-Hall, 1998.

[10] Erkorkmaz K., Yeung C.-H., Altintas Y., 2006, "Virtual CNC System - Part II: High Speed Contouring Application," *International Journal of Machine Tools and Manufacture*, Vol. 46/10, pp. 1124-1138.

[11] Astrom K.J., Wittenmark B., 1997, *Computer-Controlled Systems: Theory and Design, Third Edition*, Prentice-Hall Inc., NJ.

[12] Boucher P., Dumur D., Rahmani K.F., 1990, "Generalized Predictive Cascade Control (GPCC) for Machine Tools Drives," *Annals of CIRP*, Vol. 39, No. pp. 357-360.

[13] Altintas Y., Erkorkmaz K., Zhu W.-H., "Sliding Mode Controller Design for High-Speed Drives," *Annals of CIRP*, Vol. 49, No. 1, 2000, pp. 265–270.

[14] Tomizuka M., 1987, "Zero Phase Error Tracking Algorithm for Digital Control", *Transactions of ASME, Journal of Dynamic Systems, Measurement, and Control*, Vol. 109, pp. 65-68.

[15] Pritschow G., Philipp W., 1992, "Research on the Efficiency of Feedforward Controllers in Direct Drives", *Annals of CIRP*, Vol. 41, No. 1, pp. 411-415.

[16] Koren Y., 1983, *Computer Control of Manufacturing Systems*, McGraw-Hill, NY.

[17] Armstrong H.B., Dupont P., Canudas De Wit C., 1994, "A Survey of Models, Analysis Tools and Compensation Methods for the Control of Machines with Friction," *Automatica*, Vol. 30, No. 7, pp. 1083-1138.

[18] Lee H.S., Tomizuka M., 1996, "Robust Motion Controller Design for High-Accuracy Positioning Systems," *IEEE Transactions on Industrial Electronics*, Vol. 43, No. 1, pp. 48-55.

[19] Erkorkmaz K., Altintas Y., 2001, "High Speed CNC System Design: Part II - Modeling and Identification of Feed Drives," *International Journal of Machine Tools and Manufacture*, Vol. 41, No. 10, pp. 1487-1509.

[20] Varanasi K.K., Nayfeh S.A., 2004, "Dynamics of Lead-Screw Drives: Low-Order Modeling and Experiments," *Transactions of ASME, Journal of Dynamic Systems, Measurement, and Control*, Vol. 126, No. 2, pp. 388-396.

[21] Erkorkmaz K., Kamalzadeh A., 2006, "High Bandwidth Control of Ball Screw Drives," *Annals of CIRP*, Vol. 55, No. 1, pp. 393-398.

[22] Kao J.Y., Yeh Z.M., Tarng Y.S., Lin Y.S., 1996, "A Study of Backlash on the Motion Accuracy of CNC Lathes," *International Journal of Machine Tools and Manufacture*, Vol. 36, No. 5, pp. 539–550.

[23] Cuttino J.F., Dow T.A., Knight B.F., 1997, "Analytical and Experimental Identification of Nonlinearities in a Single-Nut Preloaded Ball Screw", *Transactions of ASME Journal of Mechanical Design*, Vol. 119, No. 1, pp. 15-19.

[24] Donmez M. A., Blomquist D. S., Hocken R. J., Liu C. R., Barash M. M., 1986, "A General Methodology for Machine Tool Accuracy Enhancement by Error Compensation," *Precision Engineering*, Vol. 8, No. 4, pp. 187-196.

[25] Erkorkmaz K., Wong W., 2006, "Rapid Identification Technique for Virtual CNC Drives," *Proc. CIRP 2nd Intl. Conf. on High Performance Cutting (HPC'06)*, Vancouver, BC, June 12-13.

[26] Erkorkmaz K., Wong W., 2007, "Rapid Identification Technique for Virtual CNC Drives", *International Journal of Machine Tools and Manufacture*, Vol. 47, pp. 1381-1392.

[27] Wong W., Erkorkmaz K., 2007, "Constrained Identification of Virtual Drive Models Using a Genetic Algorithm", *Proc. CIRP Sponsored International Conference on Smart Machining Systems*, National Institute of Standards and Technology (NIST), USA, March 13-15.

[28] 1998, *Symbolic Math Toolbox User's Guide*, The MathWorks Inc., Natick, MA.

[29] Karray F. O. and Silva C. De, 2004, *Soft Computing and Intelligent Systems Design: Theory, Tools, and Application*, Addison Wesley.

[30] Holland J. H. ,1975, *Adaptation in Natural and Artificial Systems*, University of Michigan Press, Ann Arbor.

[31] Fogel, D.B., 2006, *Evolutionary Computation: Toward a New Philosophy of Machine Intelligence 3rd Edition*, IEEE Press.

[32] Fogel, D.B., 1991, *System Identification through Simulated Evolution: A Machine Learning Approach to Modeling, Needham*, Ginn Press.

[33] Fogel D.B., Fogel L.J., Atmar J.W., 1991, "Meta-Evolutionary Programming," *Conference Record - Asilomar Conference on Circuits, Systems & Computers*, Vol. 1, pp. 540-545.

[34] Fogel D.B., Fogel L.J., 1998, "Route Optimization Through Evolutionary Programming," *Proceeding of 22nd Asilomar Conference on Signals, Systems & Computers*, Pacific Grove, California, pp. 679-680.

[35] Fogel D.B., 1990, "A Parallel Processing Approach to a Multiple Traveling Salesman Problem Using Evolutionary Programming," *Proceeding of the Fourth Annual Symposium on Parallel Processing*, Fullerton, CA, pp. 318-326.

[36] Kovacic M., Brezocnik M., Pahole I., Balic J., Kecelj B., 2005, "Evolutionary Programming of CNC Machines," *Journal of Materials Processing Technology*, Vol. 164-165, AMPT/ANMEOS Part 2, pp. 1379-1387.

[37] Bruzzese C., Corti F., Nistico E., Santini E., 2004, "Numerical Identification of Parameters for Dynamic Analysis of Single-Cage Induction Motors Starting from Data-Sheet Quantities," *Proceedings of the IASTED International Conference on Applied Simulation and Modelling*, pp 195-200

[38] Ma J.T., Lai L.L., 1995, "Determination of Operational Parameters of Electrical Machines Using Evolutionary Programming," *Electrical Machines and Drives, IEEE Conference Publication*, No. 412, pp. 116-120.

[39] Aliprantis D. C., Sudhoff S.D., Kuhn B.T., 2006, "Genetic Algorithm-Based Parameter Identification of a Hysteretic Brushless Exciter Model," *IEEE Transactions on Energy Conversion*, Vol. 21, No. 1, pp. 148-154.

[40] Kim Y.-H., Yang B.-S., Tan A.C.-C., 2007, "Bearing Parameter Identification of Rotor-Bearing System Using Clustering-Based Hybrid Evolutionary Algorithm," *Structural and Multidisciplinary Optimization*, Vol. 33, No. 6, Special Issue on Industrial Applications, pp. 493-506.

[41] Low K.S., Keck M.T., Tseng K.J., 2001, "Parameter Identification and Controller Optimization Using GA for a Precision Stage," *IEEE Proceedings of the International Conference on Power Electronics and Drive Systems*, Vol. 2, pp. 694-698.

[42] Kwok N. M., Liu D. K., Dissanayake G., 2006, "Evolutionary computing based mobile robot localization," Engineering Applications of Artificial Intelligence, Vol. 19/ 8, pp. 857-868.

[43] Mabu S., Hatakeyamay H., Thu M. T., Hirasawa K., Hu J., 2006, "Genetic network programming with reinforcement learning and its application to making mobile robot behavior," IEEJ Transactions on Electronics, Information and Systems, Vol. 126/ 8, pp. 1009-1015.

[44] Moreno L., Garrido S., Munoz M. L., 2006, "Evolutionary filter for robust mobile robot global localization," Robotics and Autonomous Systems, Vol. 54/7, pp. 590-600.

[45] Ljung L., 1998, *System Identification: Theory for the User, 2nd Edition*, Prentice-Hall of Canada Ltd.

[46] Kalman R. E., 1960, "A New Approach to Linear Filtering and Prediction Problems," *Journal of Basic Engineering*, Vol. 82, pp. 35-44.

[47] Dek, K., Beyer H.-G., 2001, "Self-Adaptive Genetic Algorithms with Simulated Binary Crossover," *Evolutionary Computation*, Vol. 9 No. 2, pp. 197-221.

[48] Erkorkmaz, K., Altintas, Y., 2001, "High Speed CNC System Design: Part III - High Speed Tracking and Contouring Control of Feed Drives," *International Journal of Machine Tools and Manufacture*, Vol. 41, No. 11, pp. 1637-1658.

[49] 2001, *Deckel Maho 80P Hi-dyn Operation Manual*, Gildemeister Aktiengesellschaft.

[50] 2001, *Heidenhain TNC 430M Operation Manual*, Heidenhain Corporation.

Appendix A

Simulation and Experiment Results

PID Result

X Axis

$$
P = \begin{bmatrix}
0.07 & -2943.87 & 4884.02 & 3.32 & 2895.29 & -5040.32 & -19.13 & 13.23 \\
-2943.87 & 129192050.83 & 5217.94 & -5974.88 & -127038376.58 & 44541892.45 & 694583.52 & -694548.72 \\
4884.02 & 5217.94 & 104569710956.76 & 127038383.55 & -44550970.54 & -87613857788.65 & 2747.25 & 8547.00 \\
3.32 & -5974.88 & 127038383.55 & 515631.00 & 0.00 & -125195411.85 & 3110.73 & 3620.41 \\
2895.29 & -127038376.58 & -44550970.54 & 0.00 & 125195400.24 & 125.45 & -686005.85 & 686343.74 \\
-5040.32 & 44541892.45 & -87613857788.65 & -125195411.85 & 125.45 & 85689028883.82 & 776371.32 & -719047.54 \\
-19.13 & 694583.52 & 2747.25 & 3110.73 & -686005.85 & 776371.32 & 11334.00 & 0.00 \\
13.23 & -694548.72 & 8547.00 & 3620.41 & 686343.74 & -719047.54 & 0.00 & 10419.00
\end{bmatrix}
$$

$$
R^T = \begin{bmatrix}
3.29 & -0.60 & 129191932.30 & 518523.76 & -5974.97 & -127038271.30 & 3153.24 & 3580.59
\end{bmatrix}
$$

$$
A = \begin{bmatrix}
521456.90 & 6.57 & -1733.08 & 257863340.00 \\
6.57 & 0.28 & -11766.35 & 17086.81 \\
-1733.08 & -11766.35 & 516027544.81 & -3616974.58 \\
257863340.00 & 17086.81 & -3616974.58 & 373857684362.75
\end{bmatrix}
$$

$$
B = \begin{bmatrix}
1042913.81 & 13.16 & -1734.29 & 516247204.61
\end{bmatrix}
$$

$$
\Gamma = \begin{bmatrix}
521465.16
\end{bmatrix}
$$

		CASE 1	CASE 2	CASE 3	CASE 4	CASE 5	CASE 6	CASE 7	CASE 8	CASE 9	CASE 10
a1	=	213.42	213.04	212.82	212.54	213.04	213.68	213.83	212.90	212.72	213.64
a2	=	59913.85	59903.18	59907.42	59821.44	59799.41	60047.11	59941.51	59903.53	59871.84	59862.96
a3	=	658081.59	678264.79	634723.36	687813.17	681554.05	669815.31	685088.91	652840.15	651192.92	676122.73
b0	=	-0.34	-0.34	-0.34	-0.34	-0.34	-0.34	-0.34	-0.34	-0.34	-0.34
b1	=	203.75	202.90	203.67	202.17	202.82	203.75	203.55	203.33	203.18	203.56
b2	=	59917.32	59906.85	59910.85	59825.21	59803.04	60050.69	59945.10	59907.06	59875.38	59866.48
d0	=	610.67	616.58	602.99	618.62	616.88	615.40	619.49	608.62	607.77	616.05
d1	=	-284.95	-280.06	-289.78	-276.95	-278.53	-283.47	-279.32	-285.71	-285.72	-280.63
p1 [Hz]	=	38.20	38.17	38.23	38.14	38.13	38.23	38.18	38.20	38.20	38.16
p1 zeta	=	0.42	0.42	0.42	0.42	0.42	0.42	0.42	0.42	0.42	0.42
p2 [Hz]	=	38.20	38.17	38.23	38.14	38.13	38.23	38.18	38.20	38.20	38.16
p2 zeta	=	0.42	0.42	0.42	0.42	0.42	0.42	0.42	0.42	0.42	0.42
p3 [Hz]	=	1.82	1.88	1.75	1.91	1.89	1.85	1.90	1.80	1.80	1.87
p3 zeta	=	1.00	1.00	1.00	1.00	1.00	1.00	1.00	1.00	1.00	1.00
z1 [Hz]	=	129.79	130.05	129.46	130.58	130.70	129.21	130.03	129.72	129.85	130.34
z1 zeta	=	-1.00	-1.00	-1.00	-1.00	-1.00	-1.00	-1.00	-1.00	-1.00	-1.00
z2 [Hz]	=	32.92	32.99	32.96	33.06	32.99	32.91	32.91	32.97	32.99	32.91
z2 zeta	=	1.00	1.00	1.00	1.00	1.00	1.00	1.00	1.00	1.00	1.00
z3 [Hz]	=	1.82	1.88	1.75	1.91	1.89	1.85	1.90	1.81	1.80	1.87
z3 zeta	=	1.00	1.00	1.00	1.00	1.00	1.00	1.00	1.00	1.00	1.00

PID Result

Y Axis

A

P =

0.10	-3447.74	9463.67	23.64	3365.96	-9714.41	-21.90	16.27
-3447.74	130069619.39	5963.36	-10823.24	-127382858.57	54354573.69	696432.12	-696396.10
9463.67	5963.36	106863835287.21	127382865.83	-54364257.41	-87631279510.00	-23504.25	20451.75
23.64	-10823.24	127382865.83	515631.00	0.00	-125195411.85	3152.01	3578.37
3365.96	-127382858.57	-54364257.41	0.00	125195400.24	125.45	-685442.48	685858.06
-9714.41	54354573.69	-87631279510.00	-125195411.85	125.45	85689028883.82	819702.12	-741320.32
-21.90	696432.12	-23504.25	3152.01	-685442.48	819702.12	11323.00	0.00
16.27	-696396.10	20451.75	3578.37	685858.06	-741320.32	0.00	10439.00

R^T =

23.60	-0.65	130069485.21	518992.09	-10823.33	-127382749.65	3235.11	3497.60

A =

522411.10	47.17	-2423.57	259272491.56
47.17	0.39	-13732.27	34346.01
-2423.57	-13732.27	519047603.91	-2847469.15
259272491.56	34346.01	-2847469.15	376204258511.42

B =

1044822.20	94.37	-2424.87	519411461.99

Γ = 522435.07

		CASE 1	CASE 2	CASE 3	CASE 4	CASE 5	CASE 6	CASE 7	CASE 8	CASE 9	CASE 10
a1	=	121.57	121.84	121.91	122.65	122.42	123.17	121.56	121.97	122.76	121.72
a2	=	39969.80	39846.50	40142.58	40086.61	40058.68	40059.37	40016.60	40012.55	40115.43	39934.88
a3	=	108746.02	141620.89	125602.84	145565.69	140617.89	141574.65	124697.04	137145.86	136197.90	140358.38
b0	=	-0.08	-0.08	-0.09	-0.09	-0.08	-0.09	-0.08	-0.08	-0.09	-0.08
b1	=	122.62	122.07	122.55	122.80	122.69	123.43	122.21	122.32	123.16	121.98
b2	=	39960.67	39836.12	40132.88	40076.03	40048.31	40048.81	40006.94	40002.37	40105.17	39924.61
d0	=	460.25	472.27	469.40	477.27	474.78	475.62	467.30	472.55	473.88	472.76
d1	=	-430.14	-424.67	-430.53	-427.76	-427.88	-428.17	-428.80	-427.46	-429.34	-425.91
p1 [Hz]	=	31.69	31.60	31.74	31.69	31.69	31.68	31.69	31.67	31.71	31.64
p1 zeta	=	0.30	0.30	0.30	0.30	0.30	0.30	0.30	0.30	0.30	0.30
p2 [Hz]	=	31.69	31.60	31.74	31.69	31.69	31.68	31.69	31.67	31.71	31.64
p2 zeta	=	0.30	0.30	0.30	0.30	0.30	0.30	0.30	0.30	0.30	0.30
p3 [Hz]	=	0.44	0.57	0.50	0.58	0.56	0.57	0.50	0.55	0.55	0.57
p3 zeta	=	1.00	1.00	1.00	1.00	1.00	1.00	1.00	1.00	1.00	1.00
z1 [Hz]	=	276.44	289.85	266.53	271.96	273.47	272.81	275.22	276.69	268.79	283.04
z1 zeta	=	-1.00	-1.00	-1.00	-1.00	-1.00	-1.00	-1.00	-1.00	-1.00	-1.00
z2 [Hz]	=	43.29	43.55	43.16	43.10	43.17	42.93	43.37	43.33	42.98	43.50
z2 zeta	=	1.00	1.00	1.00	1.00	1.00	1.00	1.00	1.00	1.00	1.00
z3 [Hz]	=	0.44	0.57	0.50	0.58	0.56	0.57	0.50	0.55	0.55	0.57
z3 zeta	=	1.00	1.00	1.00	1.00	1.00	1.00	1.00	1.00	1.00	1.00

P-PI Result

X Axis

$$
P = \begin{bmatrix}
470.09 & -4071.20 & 2870766.34 & 14192.22 & -91039.96 & -2890937.30 & 57.32 & 169.14 \\
-4071.20 & 86720098.35 & 336557.31 & -2871335.33 & -85519746.33 & 1244415212.90 & 587514.04 & -588333.94 \\
2870766.34 & 336557.31 & 39539797957.15 & 85519810.22 & -1244492060.95 & -35770419680.63 & 12515.25 & 17704.50 \\
14192.22 & -2871335.33 & 85519810.22 & 515631.00 & 0.00 & -125195411.85 & -16912.78 & 23769.26 \\
-91039.96 & -85519746.33 & -1244492060.95 & 0.00 & 125195400.24 & 125.45 & -574922.75 & 574271.46 \\
-2890937.30 & 1244415212.90 & -35770419680.63 & -125195411.85 & 125.45 & 85689028883.82 & 7494600.14 & -7494805.89 \\
57.32 & 587514.04 & 12515.25 & -16912.78 & -574922.75 & 7494600.14 & 11411.00 & 0.00 \\
169.14 & -588333.94 & 17704.50 & 23769.26 & 574271.46 & -7494805.89 & 0.00 & 10469.00
\end{bmatrix}
$$

$$
R^T = \begin{bmatrix}
14144.32 & -336.04 & 86741367.80 & 423145.38 & -2871333.32 & -85522171.59 & 2582.35 & 4249.24
\end{bmatrix}
$$

$$
A = \begin{bmatrix}
420321.47 & 27934.08 & -336968.54 & 184852741.97 \\
27934.08 & 1863.02 & -32726.88 & 12039171.10 \\
-336968.54 & -32726.88 & 331261744.49 & 529475198.27 \\
184852741.97 & 12039171.10 & 529475198.27 & 135678452754.28
\end{bmatrix}
$$

$$
B = \begin{bmatrix}
840642.93 & 56222.72 & -337640.62 & 358335477.57
\end{bmatrix}
$$

$$
\Gamma = 425759.61
$$

		CASE 1	CASE 2	CASE 3	CASE 4	CASE 5	CASE 6	CASE 7	CASE 8	CASE 9	CASE 10
a1	=	2929.18	2712.31	2701.78	2404.89	2612.99	3209.30	2706.45	2711.81	2822.79	2564.27
a2	=	850140.42	788900.46	759604.52	705031.17	736974.73	929338.15	783826.63	785805.65	815595.43	748602.00
a3	=	23331825.09	21658797.19	20778800.53	19376364.04	20159946.08	25493241.90	21509954.91	21560995.56	22368683.97	20563535.84
b0	=	1.17	1.09	0.99	0.99	0.99	1.30	1.07	1.11	1.16	1.03
b1	=	-457.60	-422.38	-404.20	-374.69	-393.00	-504.63	-418.79	-422.59	-440.31	-398.81
b2	=	72427.97	66954.45	66990.37	59162.32	64987.22	79573.68	66844.77	67111.14	69976.04	63165.58
d0	=	7904.28	7332.26	6480.63	6564.67	6855.57	8684.10	7265.97	7356.78	7650.53	6945.79
d1	=	-5793.03	-5371.80	-6167.68	-4809.69	-5031.68	-6377.88	-5319.21	-5405.13	-5626.12	-5083.99
p1 [Hz]	=	414.83	379.65	379.94	329.23	365.39	460.10	378.96	379.79	397.91	355.42
p1 zeta	=	1.00	1.00	1.00	1.00	1.00	1.00	1.00	1.00	1.00	1.00
p2 [Hz]	=	46.49	47.15	45.18	48.65	45.60	45.80	46.91	46.93	46.47	47.82
p2 zeta	=	1.00	1.00	1.00	1.00	1.00	1.00	1.00	1.00	1.00	1.00
p3 [Hz]	=	4.88	4.88	4.88	4.88	4.88	4.88	4.88	4.88	4.88	4.88
p3 zeta	=	1.00	1.00	1.00	1.00	1.00	1.00	1.00	1.00	1.00	1.00
z1 [Hz]	=	59.18	59.10	60.87	58.58	60.19	58.85	59.51	58.58	58.52	59.09
z1 zeta	=	-0.72	-0.72	-0.72	-0.71	-0.72	-0.72	-0.72	-0.71	-0.71	-0.71
z2 [Hz]	=	59.18	59.10	60.87	58.58	60.19	58.85	59.51	58.58	58.52	59.09
z2 zeta	=	-0.72	-0.72	-0.72	-0.71	-0.72	-0.72	-0.72	-0.71	-0.71	-0.71
z3 [Hz]	=	22.86	22.92	22.78	23.01	22.72	22.75	22.93	22.81	22.74	22.99
z3 zeta	=	1.00	1.00	1.00	1.00	1.00	1.00	1.00	1.00	1.00	1.00

P-PI Result

Y Axis

A

P =

470.19	-4111.67	2871445.60	14194.53	-91026.85	-2891623.62	56.45	169.77
-4111.67	86737552.74	336557.31	-2872022.28	-85521047.94	1244786004.30	587578.14	-588398.65
2871445.60	336557.31	39498613482.35	85521111.83	-1244862852.35	-35752401389.19	9157.50	19536.00
14194.53	-2872022.28	85521111.83	515631.00	0.00	-125195411.85	-16944.71	23770.86
-91026.85	-85521047.94	-1244862852.35	0.00	125195400.24	125.45	-574245.18	574187.70
-2891623.62	1244786004.30	-35752401389.19	-125195411.85	125.45	85689028883.82	7513729.53	-7494801.99
56.45	587578.14	9157.50	-16944.71	-574245.18	7513729.53	11414.00	0.00
169.77	-588398.65	19536.00	23770.86	574187.70	-7494801.99	0.00	10477.00

R^T =

14146.61	-336.53	86758837.85	423158.15	-2872020.26	-85523474.41	2552.46	4247.27

A =

420378.85	27939.09	-336827.69	184906495.50
27939.09	1863.44	-32875.61	12042568.40
-336827.69	-32875.61	331331882.55	530544222.16
184906495.50	12042568.40	530544222.16	135605585879.44

B =

840757.69	56232.31	-337500.75	358424171.20

Γ =

425812.46

		CASE 1	CASE 2	CASE 3	CASE 4	CASE 5	CASE 6	CASE 7	CASE 8	CASE 9	CASE 10
a1	=	2978.66	3148.44	2601.89	3164.07	3058.17	2714.60	2628.40	3524.97	2648.60	2763.19
a2	=	859306.79	886908.54	760283.07	892518.75	853168.10	777013.34	753886.31	1006658.79	742619.21	791177.89
a3	=	23574778.15	24255172.27	20886320.94	24415910.58	23307185.67	21300652.15	20671422.26	27578184.45	20308056.49	21688001.70
b0	=	1.17	1.22	1.05	1.20	1.15	1.04	1.02	1.36	0.97	1.07
b1	=	-461.62	-481.12	-405.44	-482.33	-460.85	-414.06	-401.50	-546.51	-394.46	-422.90
b2	=	73494.09	78400.98	64087.75	78661.87	76263.40	67004.92	64848.79	87400.24	65696.24	68255.02
d0	=	7347.17	7680.82	7052.70	7674.78	7364.81	6629.09	6449.82	8622.69	6334.34	6770.33
d1	=	-6991.16	-7315.86	-5161.75	-7307.58	-7014.61	-6307.37	-6137.24	-8207.91	-6028.51	-6442.77
p1 [Hz]	=	423.16	451.85	361.47	454.29	437.86	380.97	366.89	511.60	371.50	388.81
p1 zeta	=	1.00	1.00	1.00	1.00	1.00	1.00	1.00	1.00	1.00	1.00
p2 [Hz]	=	46.03	44.36	47.75	44.41	43.99	46.19	46.55	44.54	45.16	46.09
p2 zeta	=	1.00	1.00	1.00	1.00	1.00	1.00	1.00	1.00	1.00	1.00
p3 [Hz]	=	4.88	4.88	4.88	4.88	4.88	4.88	4.88	4.88	4.88	4.88
p3 zeta	=	1.00	1.00	1.00	1.00	1.00	1.00	1.00	1.00	1.00	1.00
z1 [Hz]	=	59.67	59.52	59.09	60.10	60.19	60.13	59.78	59.99	61.00	59.86
z1 zeta	=	-0.72	-0.72	-0.72	-0.72	-0.72	-0.72	-0.72	-0.72	-0.72	-0.72
z2 [Hz]	=	59.67	59.52	59.09	60.10	60.19	60.13	59.78	59.99	61.00	59.86
z2 zeta	=	-0.72	-0.72	-0.72	-0.72	-0.72	-0.72	-0.72	-0.72	-0.72	-0.72
z3 [Hz]	=	22.88	22.55	22.99	22.64	22.54	22.90	22.90	22.72	22.77	22.86
z3 zeta	=	1.00	1.00	1.00	1.00	1.00	1.00	1.00	1.00	1.00	1.00

SMC Result

X Axis

$$
P = \begin{bmatrix}
0.00 & -117.97 & 364.71 & 1.51 & 117.71 & -368.27 & -1.12 & 0.59 \\
-117.97 & 125308741.73 & 2981.68 & -395.10 & -125248516.57 & -541727.78 & 688575.59 & -688579.25 \\
364.71 & 2981.68 & 89501877010.05 & 125248525.00 & 538027.84 & -86592829873.57 & -22588.50 & 25335.75 \\
1.51 & -395.10 & 125248525.00 & 515631.00 & 0.00 & -125195411.85 & 2828.33 & 3933.74 \\
117.71 & -125248516.57 & 538027.84 & 0.00 & 125195400.24 & 125.45 & -688486.44 & 688519.97 \\
-368.27 & -541727.78 & -86592829873.57 & -125195411.85 & 125.45 & 85689028883.82 & 157140.20 & -145273.66 \\
-1.12 & 688575.59 & -22588.50 & 2828.33 & -688486.44 & 157140.20 & 11522.00 & 0.00 \\
0.59 & -688579.25 & 25335.75 & 3933.74 & 688519.97 & -145273.66 & 0.00 & 10327.00
\end{bmatrix}
$$

$$
R^T = \begin{bmatrix}
1.51 & 0.00 & 125308749.18 & 515748.52 & -395.10 & -125248525.02 & 2841.36 & 3920.73
\end{bmatrix}
$$

$$
A = \begin{bmatrix}
515866.16 & 3.02 & -2.21 & 250605803.85 \\
3.02 & 0.00 & -471.18 & 1423.66 \\
-2.21 & -471.18 & 501213818.66 & -7392.41 \\
250605803.85 & 1423.66 & -7392.41 & 352065377427.18
\end{bmatrix}
$$

$$
B = \begin{bmatrix}
1031732.32 & 6.05 & -2.21 & 501223302.21
\end{bmatrix}
$$

$$
\Gamma = \begin{bmatrix}
515866.31
\end{bmatrix}
$$

		CASE 1	CASE 2	CASE 3	CASE 4	CASE 5	CASE 6	CASE 7	CASE 8	CASE 9	CASE 10
a1	=	563.15	562.88	566.27	565.16	566.77	557.07	565.39	565.66	567.23	554.92
a2	=	370078.01	369425.59	370273.55	369708.69	370307.33	369741.98	369332.67	370403.09	370735.66	366241.68
a3	=	15304659.73	15221615.16	15306266.62	15218798.31	15310818.53	15243434.15	15188121.80	15342178.68	15333310.44	15144283.54
b0	=	0.85	0.85	0.85	0.85	0.85	0.85	0.85	0.85	0.85	0.85
b1	=	571.04	570.76	574.16	573.06	574.66	564.96	573.28	573.54	575.13	562.72
b2	=	370082.44	369430.21	370278.02	369713.36	370311.79	369746.54	369337.39	370407.45	370740.11	366246.10
d0	=	2363.07	2354.40	2363.99	2355.19	2364.49	2356.77	2351.59	2367.22	2367.64	2337.89
d1	=	-1856.36	-1851.08	-1857.34	-1852.14	-1857.66	-1852.55	-1849.73	-1859.03	-1860.01	-1836.48
p1 [Hz]	=	93.78	93.70	93.79	93.73	93.79	93.78	93.68	93.80	93.84	93.31
p1 zeta	=	0.44	0.44	0.44	0.44	0.44	0.44	0.44	0.44	0.44	0.44
p2 [Hz]	=	93.78	93.70	93.79	93.73	93.79	93.78	93.68	93.80	93.84	93.31
p2 zeta	=	0.44	0.44	0.44	0.44	0.44	0.44	0.44	0.44	0.44	0.44
p3 [Hz]	=	7.02	6.99	7.02	6.98	7.02	6.99	6.98	7.03	7.02	7.01
p3 zeta	=	1.00	1.00	1.00	1.00	1.00	1.00	1.00	1.00	1.00	1.00
z1 [Hz]	=	101.65	101.55	101.66	101.58	101.66	101.65	101.52	101.68	101.73	101.04
z1 zeta	=	0.49	0.49	0.49	0.49	0.50	0.49	0.49	0.49	0.50	0.49
z2 [Hz]	=	101.65	101.55	101.66	101.58	101.66	101.65	101.52	101.68	101.73	101.04
z2 zeta	=	0.49	0.49	0.49	0.49	0.50	0.49	0.49	0.49	0.50	0.49
z3 [Hz]	=	7.03	7.00	7.03	7.00	7.03	7.00	6.99	7.04	7.03	7.03
z3 zeta	=	1.00	1.00	1.00	1.00	1.00	1.00	1.00	1.00	1.00	1.00

SMC Result

Y Axis

A

P =

0.00	-81.79	260.09	1.07	81.67	-262.84	-0.65	0.54
-81.79	125274029.74	4286.17	-281.27	-125231986.86	-500602.46	688617.11	-688620.77
260.09	4286.17	89430596188.28	125231996.50	495692.86	-86537664103.28	-43956.00	36324.75
1.07	-281.27	125231996.50	515631.00	0.00	-125195411.85	2673.09	4056.03
81.67	-125231986.86	495692.86	0.00	125195400.24	125.45	-688466.71	688502.47
-262.84	-500602.46	-86537664103.28	-125195411.85	125.45	85689028883.82	186183.12	-168015.78
-0.65	688617.11	-43956.00	2673.09	-688466.71	186183.12	11522.00	0.00
0.54	-688620.77	36324.75	4056.03	688502.47	-168015.78	0.00	10322.00

R^T =

1.07	0.00	125274038.68	515712.54	-281.27	-125231995.31	2682.03	4047.09

A =

515794.13	2.14	-0.21	250538937.71
2.14	0.00	-326.87	1014.79
-0.21	-326.87	501079809.17	27059.46
250538937.71	1014.79	27059.46	351662868848.43

B =

1031588.26	4.27	-0.22	501087015.07

Γ =

515794.20

		CASE 1	CASE 2	CASE 3	CASE 4	CASE 5	CASE 6	CASE 7	CASE 8	CASE 9	CASE 10
a1	=	442.30	443.25	436.91	447.82	443.85	445.83	442.77	441.21	448.34	439.90
a2	=	480536.47	484304.21	478035.86	484129.76	485913.06	481396.94	480154.88	481773.67	483551.01	482670.90
a3	=	22720934.07	22894600.41	22540962.86	22924951.87	22869843.60	22793081.37	22629030.48	22704767.25	22905249.08	22815922.91
b0	=	0.87	0.87	0.88	0.87	0.87	0.87	0.87	0.87	0.87	0.87
b1	=	448.52	449.52	443.11	454.09	450.17	452.06	449.00	447.46	454.60	446.15
b2	=	480540.39	484308.13	478039.89	484133.62	485917.18	481400.81	480158.95	481777.73	483554.86	482674.82
d0	=	2003.31	2019.10	1989.85	2020.17	2021.40	2008.43	1998.38	2005.18	2018.07	2012.05
d1	=	-1997.31	-2013.08	-1984.27	-2013.92	-2016.05	-2002.23	-1992.90	-1999.67	-2011.78	-2006.04
p1 [Hz]	=	108.08	108.52	107.83	108.47	108.71	108.16	108.04	108.24	108.39	108.35
p1 zeta	=	0.29	0.29	0.29	0.29	0.29	0.29	0.29	0.29	0.29	0.29
p2 [Hz]	=	108.08	108.52	107.83	108.47	108.71	108.16	108.04	108.24	108.39	108.35
p2 zeta	=	0.29	0.29	0.29	0.29	0.29	0.29	0.29	0.29	0.29	0.29
p3 [Hz]	=	7.84	7.84	7.82	7.86	7.80	7.85	7.82	7.81	7.86	7.84
p3 zeta	=	1.00	1.00	1.00	1.00	1.00	1.00	1.00	1.00	1.00	1.00
z1 [Hz]	=	115.50	116.04	115.18	115.98	116.28	115.60	115.45	115.69	115.89	115.83
z1 zeta	=	0.32	0.32	0.32	0.32	0.32	0.32	0.32	0.32	0.32	0.32
z2 [Hz]	=	115.50	116.04	115.18	115.98	116.28	115.60	115.45	115.69	115.89	115.83
z2 zeta	=	0.32	0.32	0.32	0.32	0.32	0.32	0.32	0.32	0.32	0.32
z3 [Hz]	=	7.85	7.85	7.83	7.87	7.81	7.87	7.83	7.82	7.87	7.85
z3 zeta	=	1.00	1.00	1.00	1.00	1.00	1.00	1.00	1.00	1.00	1.00

ZPETC Result

X Axis & Y Axis

$$
P = \begin{bmatrix}
0.00 & -118.56 & -1528.07 & -19.66 & 118.01 & 1520.83 & -2.04 & 1.30 \\
-118.56 & 68626328.38 & 1953.18 & 1512.75 & -68596051.33 & -163841.70 & 688761.89 & -688766.26 \\
-1528.07 & 1953.18 & 17779812744.34 & 68596059.75 & 160130.98 & -14237423606.37 & -312.51 & -1875.04 \\
-19.66 & 1512.75 & 68596059.75 & 936273.62 & 0.01 & -68580241.80 & 5973.05 & 6436.56 \\
118.01 & -68596051.33 & 160130.98 & 0.01 & 68580233.74 & 1762.09 & -688590.80 & 688601.35 \\
1520.83 & -163841.70 & -14237423606.37 & -68580241.80 & 1762.09 & 14239627660.71 & 17928.25 & -11003.66 \\
-2.04 & 688761.89 & -312.51 & 5973.05 & -688590.80 & 17928.25 & 21071.00 & 0.00 \\
1.30 & -688766.26 & -1875.04 & 6436.56 & 688601.35 & -11003.66 & 0.00 & 18877.00
\end{bmatrix}
$$

$$
R^T = \begin{bmatrix}
-19.66 & -0.01 & 68626336.58 & 936392.39 & 1512.76 & -68596059.18 & 5970.43 & 6439.29
\end{bmatrix}
$$

$$
A = \begin{bmatrix}
936511.26 & -39.33 & -0.17 & 137223898.45 \\
-39.33 & 0.00 & -472.76 & -6098.70 \\
-0.17 & -472.76 & 274461954.36 & 7866.57 \\
137223898.45 & -6098.70 & 7866.57 & 60485755382.95
\end{bmatrix}
$$

$$
B = \begin{bmatrix}
1873022.52 & -78.65 & -0.18 & 274476571.62
\end{bmatrix}
$$

$$
\Gamma = \begin{bmatrix}
936511.72
\end{bmatrix}
$$

		CASE 1	CASE 2	CASE 3	CASE 4	CASE 5	CASE 6	CASE 7	CASE 8	CASE 9	CASE 10
a1	=	223.83	222.09	223.54	222.08	225.16	224.29	219.71	217.25	220.75	222.27
a2	=	244080.43	243437.35	244569.07	242804.79	243886.93	244059.06	243124.83	243689.80	242957.87	243084.85
a3	=	6519729.61	6474942.92	6514641.21	6469218.71	6501997.31	6537475.37	6460137.65	6356067.32	6403613.72	6438261.09
b0	=	0.75	0.75	0.75	0.76	0.75	0.75	0.76	0.76	0.76	0.76
b1	=	238.37	236.60	238.12	236.56	239.70	238.83	234.21	231.80	235.24	236.77
b2	=	244230.16	243586.13	244718.74	242953.41	244036.29	244209.15	243273.29	243836.20	243105.18	243232.86
d0	=	1030.65	1025.55	1031.15	1023.83	1028.74	1032.14	1023.67	1015.79	1018.47	1021.70
d1	=	-994.32	-989.74	-995.03	-987.95	-992.64	-995.53	-988.01	-981.90	-983.65	-986.37
p1 [Hz]	=	77.76	77.67	77.84	77.56	77.72	77.75	77.63	77.74	77.60	77.61
p1 zeta	=	0.20	0.20	0.20	0.20	0.20	0.20	0.20	0.20	0.20	0.20
p2 [Hz]	=	77.76	77.67	77.84	77.56	77.72	77.75	77.63	77.74	77.60	77.61
p2 zeta	=	0.20	0.20	0.20	0.20	0.20	0.20	0.20	0.20	0.20	0.20
p3 [Hz]	=	4.35	4.33	4.33	4.34	4.34	4.36	4.32	4.24	4.29	4.31
p3 zeta	=	1.00	1.00	1.00	1.00	1.00	1.00	1.00	1.00	1.00	1.00
z1 [Hz]	=	89.47	89.31	89.58	89.15	89.41	89.47	89.24	89.34	89.17	89.21
z1 zeta	=	0.26	0.26	0.26	0.26	0.26	0.26	0.25	0.25	0.25	0.26
z2 [Hz]	=	89.47	89.31	89.58	89.15	89.41	89.47	89.24	89.34	89.17	89.21
z2 zeta	=	0.26	0.26	0.26	0.26	0.26	0.26	0.25	0.25	0.25	0.26
z3 [Hz]	=	4.35	4.34	4.34	4.34	4.35	4.37	4.33	4.25	4.29	4.32
z3 zeta	=	1.00	1.00	1.00	1.00	1.00	1.00	1.00	1.00	1.00	1.00

DMG Test Case

X Axis

$$P = \begin{bmatrix} 13.61 & -559.81 & 97838.56 & 1078.50 & -674.93 & -97921.56 & -24.32 & -21.60 \\ -559.81 & 7804138.00 & 26759.26 & -97900.30 & -7703285.94 & 18728888.89 & 69932.83 & -70140.50 \\ 97838.56 & 26759.26 & 4285841049.38 & 7701547.22 & -18757222.22 & -3773640046.30 & 2569.44 & -6458.33 \\ 1078.50 & -97900.30 & 7701547.22 & 85860.82 & 28.24 & -7841693.60 & -2367.51 & -1203.34 \\ -674.93 & -7703285.94 & -18757222.22 & 28.24 & 7842614.10 & 7500.00 & -68558.17 & 68763.42 \\ -97921.56 & 18728888.89 & -3773640046.30 & -7841693.60 & 7500.00 & 4620891203.70 & 131875.00 & -128472.22 \\ -24.32 & 69932.83 & 2569.44 & -2367.51 & -68558.17 & 131875.00 & 3070.00 & 0.00 \\ -21.60 & -70140.50 & -6458.33 & -1203.34 & 68763.42 & -128472.22 & 0.00 & 3734.00 \end{bmatrix}$$

$$R^T = \begin{bmatrix} 1078.13 & -12.87 & 7802964.06 & 85155.97 & -97862.16 & -7702664.44 & -1489.14 & -2084.26 \end{bmatrix}$$

$$A = \begin{bmatrix} 85680.48 & 2156.18 & -1449.60 & 15625692.09 \\ 2156.18 & 54.42 & -2253.42 & 391511.11 \\ -1449.60 & -2253.42 & 30923560.66 & 5566719.92 \\ 15625692.09 & 391511.11 & 5566719.92 & 13742276547.57 \end{bmatrix}$$

$$B = \begin{bmatrix} 171360.95 & 4312.44 & -1475.34 & 31231620.20 \end{bmatrix}$$

$$\Gamma = \begin{bmatrix} 85686.06 \end{bmatrix}$$

		CASE 1	CASE 2	CASE 3	CASE 4	CASE 5	CASE 6	CASE 7	CASE 8	CASE 9	CASE 10
a1	=	2950.11	2935.88	3000.83	2948.34	2954.44	2940.28	2955.44	2955.70	2826.85	2960.94
a2	=	527085.54	525284.51	535812.19	527256.56	526615.78	523626.18	528361.84	528457.66	503377.86	528545.90
a3	=	18790850.41	18871992.20	19152858.80	18874094.34	18664746.89	18537748.45	18916647.44	18951127.44	17823895.98	18839665.28
b0	=	0.84	0.83	0.83	0.83	0.84	0.83	0.83	0.83	0.83	0.83
b1	=	-2029.44	-2013.98	-2056.88	-2026.09	-2030.33	-2018.06	-2029.20	-2027.15	-1939.40	-2032.78
b2	=	290211.06	287388.91	294378.29	289333.20	291333.10	289945.91	289903.05	289565.18	278695.82	291058.44
d0	=	4432.02	4441.98	4512.93	4446.92	4408.03	4378.82	4456.42	4462.39	4210.40	4442.91
d1	=	826.64	839.38	850.08	834.63	818.48	813.72	837.90	842.11	781.92	831.59
p1 [Hz]	=	439.54	437.23	447.66	439.23	440.31	438.07	440.37	440.41	419.95	441.30
p1 zeta	=	1.00	1.00	1.00	1.00	1.00	1.00	1.00	1.00	1.00	1.00
p2 [Hz]	=	22.23	22.19	22.14	22.21	22.21	22.20	22.20	22.18	22.27	22.19
p2 zeta	=	1.00	1.00	1.00	1.00	1.00	1.00	1.00	1.00	1.00	1.00
p3 [Hz]	=	7.75	7.84	7.79	7.80	7.69	7.68	7.80	7.82	7.68	7.76
p3 zeta	=	1.00	1.00	1.00	1.00	1.00	1.00	1.00	1.00	1.00	1.00
z1 [Hz]	=	360.56	362.22	370.85	361.73	361.65	361.05	363.50	364.79	347.18	363.93
z1 zeta	=	-1.00	-1.00	-1.00	-1.00	-1.00	-1.00	-1.00	-1.00	-1.00	-1.00
z2 [Hz]	=	32.70	32.73	32.69	32.71	32.72	32.75	32.71	32.72	32.85	32.72
z2 zeta	=	-1.00	-1.00	-1.00	-1.00	-1.00	-1.00	-1.00	-1.00	-1.00	-1.00
z3 [Hz]	=	7.67	7.75	7.70	7.71	7.61	7.60	7.72	7.73	7.60	7.67
z3 zeta	=	1.00	1.00	1.00	1.00	1.00	1.00	1.00	1.00	1.00	1.00

DMG Test Case

Y Axis

A

P	=	13.62	-571.93	97978.46	1079.15	-666.56	-98073.92	-23.91	-20.83
		-571.93	7801379.62	260092.59	-98014.91	-7701580.69	18618258.10	69913.50	-69791.25
		97978.46	260092.59	4294762731.48	7699445.90	-18893072.92	-3776089891.98	-1041.67	-25208.33
		1079.15	-98014.91	7699445.90	85860.10	4.36	-7840347.22	-2365.63	-1195.25
		-666.56	-7701580.69	-18893072.92	4.36	7841475.56	72592.59	-68629.67	68676.83
		-98073.92	18618258.10	-3776089891.98	-7840347.22	72592.59	4608371913.58	135486.11	-119097.22
		-23.91	69913.50	-1041.67	-2365.63	-68629.67	135486.11	3092.00	0.00
		-20.83	-69791.25	-25208.33	-1195.25	68676.83	-119097.22	0.00	3607.00
R^T	=	1078.78	-8.90	7804371.01	85164.14	-98027.11	-7703165.13	-1486.08	-2074.31
A	=	85701.06	2157.49	-1444.03	15627391.94				
		2157.49	54.48	-2300.13	391991.89				
		-1444.03	-2300.13	30913032.10	6260242.17				
		15627391.94	391991.89	6260242.17	13785770661.54				
B	=	171402.12	4315.04	-1461.83	31236133.95				
Γ	=	85706.64							

		CASE 1	CASE 2	CASE 3	CASE 4	CASE 5	CASE 6	CASE 7	CASE 8	CASE 9	CASE 10
a1	=	4023.51	3964.03	4004.31	3926.62	4022.65	4000.84	3921.56	3859.27	3909.74	3936.78
a2	=	698963.09	688630.48	693679.16	681890.21	698577.95	693794.78	681298.95	669456.58	678941.92	683774.53
a3	=	25998712.54	25641533.20	25651291.00	25441918.25	25947315.82	25682465.44	25373127.34	24825331.70	25247096.69	25493432.57
b0	=	0.81	0.81	0.80	0.80	0.81	0.81	0.81	0.81	0.81	0.80
b1	=	-2534.65	-2494.82	-2517.44	-2464.65	-2535.10	-2519.58	-2468.10	-2428.55	-2461.12	-2473.74
b2	=	371117.16	365289.16	370219.98	361068.71	371380.27	369939.46	361341.95	356409.26	360574.59	362302.29
d0	=	1791.01	1764.90	1773.70	1747.71	1789.44	1775.24	1746.34	1714.01	1739.65	1752.57
d1	=	-2688.47	-2649.65	-2652.89	-2623.49	-2684.75	-2658.43	-2622.10	-2568.29	-2610.40	-2631.04
p1 [Hz]	=	611.70	602.22	608.72	596.26	611.57	608.14	595.44	585.55	593.57	597.88
p1 zeta	=	1.00	1.00	1.00	1.00	1.00	1.00	1.00	1.00	1.00	1.00
p2 [Hz]	=	20.17	20.17	20.16	20.14	20.18	20.18	20.18	20.21	20.19	20.15
p2 zeta	=	1.00	1.00	1.00	1.00	1.00	1.00	1.00	1.00	1.00	1.00
p3 [Hz]	=	8.50	8.51	8.43	8.54	8.48	8.44	8.51	8.46	8.49	8.53
p3 zeta	=	1.00	1.00	1.00	1.00	1.00	1.00	1.00	1.00	1.00	1.00
z1 [Hz]	=	471.75	466.15	473.81	466.22	471.06	470.07	460.95	453.99	459.32	465.56
z1 zeta	=	-1.00	-1.00	-1.00	-1.00	-1.00	-1.00	-1.00	-1.00	-1.00	-1.00
z2 [Hz]	=	33.33	33.37	33.37	33.41	33.33	33.36	33.39	33.43	33.40	33.40
z2 zeta	=	-1.00	-1.00	-1.00	-1.00	-1.00	-1.00	-1.00	-1.00	-1.00	-1.00
z3 [Hz]	=	8.21	8.22	8.15	8.25	8.19	8.16	8.22	8.18	8.21	8.24
z3 zeta	=	1.00	1.00	1.00	1.00	1.00	1.00	1.00	1.00	1.00	1.00